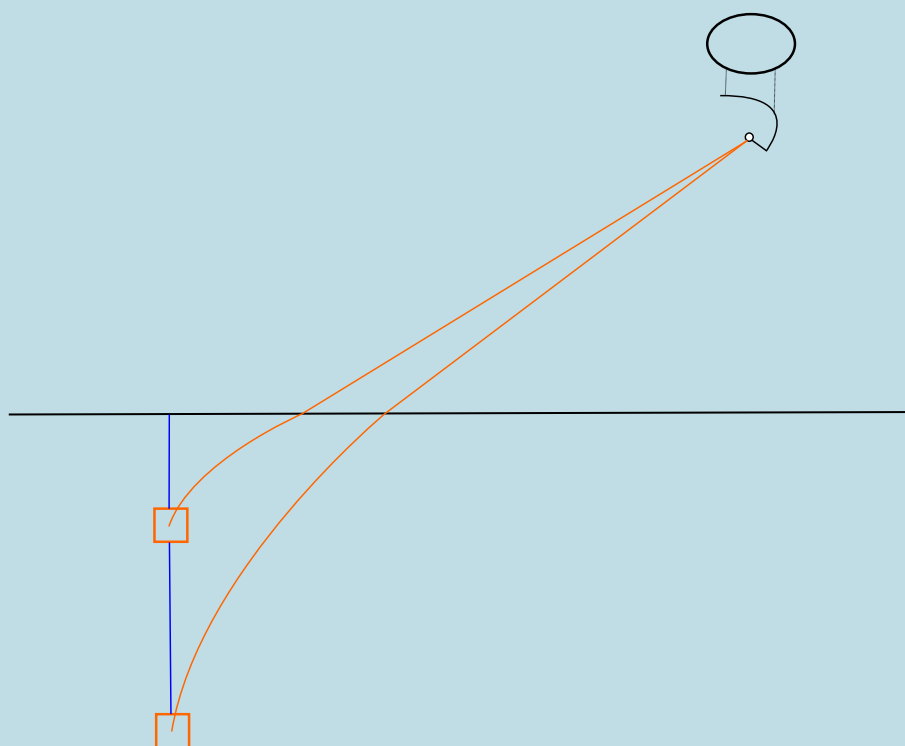


A new ray tracing algorithm for complex ice models and the analysis of ice properties using weather balloons

Arthur Adriaens



Department of Physics and Astronomy

Promotor: Prof. dr. Dirk Ryckbosch Dirk.Ryckbosch@ugent.be

Supervisor: Bob Oeyen Bob.Oeyen@ugent.be

Master's dissertation submitted in partial fulfilment of the requirements for the degree of master in Physics and Astronomy

DANKWOORD

“Educating the mind without educating the heart is no education at all”

– Aristotle

Ik zou Prof.Dr.em. Dirk Ryckbosch wensen te bedanken om daar te zijn doorheen heel mijn studie carrière. Eerst wanneer hij de voorstelling van de richting Fysica en Sterrenkunde deed in Ledeganck toen ik nog in de humaniora zat. Later wanneer ik buisde op mechanica maar hij me zei dat, aangezien mijn oefeningen goed waren, ik er duidelijk wel talent voor had en gewoon meer moest studeren met als afsluiter ”tot in de master”. En finaal hier wanneer ik een thesis doe met hem als promotor.

Ik zou Bob Oeyen willen bedanken om mij altijd te helpen wanneer ik vragen had. Ook heeft hij mij veel geholpen door kritisch te zijn op mijn werk en mij zo vooruit te helpen in beide mijn presentaties en mijn schrijfwerk.

Ik wens mijn ouders te bedanken om altijd daar te zijn voor mij. Ik apprecieer het nog altijd enorm om te kunnen jetskiën of tennissen met mijn vader (en binnenkort ook met mijn moeder). Ook zijn vele inzichten in deze thesis gekomen na even wandelen met mijn moeder en mijn hond Mickey. Zonder hen zou ik hier waarschijnlijk nooit geraakt zijn.

Als laatste wens ik mijn partner Polina te bedanken, zij heeft me meer dan wie dan ook gesteund en verdient heel mijn hart.

ABSTRACT

To infer information about the cosmos, the neutrino is an ideal candidate as it points back to the event itself. Due to the neutrino not having any charge, nearly no mass and interacting weakly we can be quite certain that if we observe a neutrino back here on earth it came from the direction we found it in.

There are, and have been, numerous neutrino detectors. But there was a need to build another one as *cosmogenic* neutrinos hadn't been observed yet. cosmogenic neutrinos are very high in energy but consequently are very low in flux, to observe cosmogenic neutrinos in human lifetimes you'll thus need a very big detector. The economical and logistical choice is to build a detector in the Greenland icecap on the principle of radio waves called *RNO-G*, for Radio Neutrino Observatory in Greenland.

As this detector is built in an icecap and the principle of detecting neutrinos is reliant on the physics of how the waves propagate through the ice, it is necessary to understand the optical properties of the Greenland ice cap well. An important optical property for neutrino reconstruction is the index of refraction-depth relation which, if modelled, is called an *ice model*.

The ice model currently being used is largely based on density-depth data but is a sub-ideal fit, in this thesis an algorithm was built to make use of a more complex ice model in chapter 4 and to test the difference between the used ice model and the actual ice properties, balloon plane wave reconstructions were performed which were used to map out the index-depth profile, as explained in chapter 5.

The following data was obtained this way:

Depth (m)	Station id	channels	Run:Event	$n_{\text{exponential}}$	n_{fit}
-48.155	21	6&7	1441:117	1.6400	$1.632 \pm 0.00128 \pm 0.00472$
-58.38	21	5&7	1441:117	1.6736	$1.66632 \pm 0.00226 \pm 0.00233$
-58.24	21	5&6&7	1441:117	1.67321	$1.66553 \pm 0.00167 \pm 0.00350$
-68.2	21	5&6	1441:117	1.6983	$1.69329 \pm 0.00199 \pm 0.00460$
-93.865	21	0&1&2&3	1441:117	1.73896	$1.71366 \pm 0.00287 \pm 0.05641$
-94.518	11	0&2&3	1034:12397	1.7397	$1.724 \pm 0.014 \pm 0.047$

SAMENVATTING

Om informatie over het heelal te leren is de neutrino een bijzonder goede bron aangezien ze, door haar zwakke interactiekracht, ongehinderd naar de aarde propageert. Als we dus een neutrino op aarde detecteren en de richting kunnen infereren zijn we vrijwel zeker waar ze vandaan komt.

Wegens deze handige eigenschappen van de neutrino zijn er al verscheidene neutrinodetectoren gebouwd. Maar er is een nood voor de bouw van nog een detector aangezien cosmogenische neutrinos nog niet geobserveerd zijn. Dit zijn neutrinos met zeer hoge energiën en dus ook laag in aantal, om deze neutrinos te kunnen observeren in doenbare tijdsperiodes is dus een grote detector nodig. Om deze reden werd de *Radio Neutrino Observatory in Greenland* of RNO-G gebouwd, een neutrino detector gebaseerd in het Groenlandse ijs.

Aangezien deze detector gebouwd is in het Groenlandse ijs en deze gebaseerd is op het principe van daarin gepropageerde radio golven is het cruciaal de optische eigenschappen van het ijs te kennen. Een zeer belangrijke optische eigenschap is the index van refractie-diepte relatie, dewelke gemodelleerd word en dan een *ijsmodel* wordt genoemd.

Het momentaan gebruikte ijsmodel is gebaseerd op een fit aan een lineaire omzetting van dichtheid-diepte metingen. Deze fit kan sub-optimaal zijn en om accuraat met moeilijkere ijsmodellen te kunnen omgaan werd in deze thesis, in hoofdstuk 4, een nieuw *ray tracing* algoritme gebouwd. Om te kijken of het wel degelijk nodig is een nieuwe te gebruiken werden metingen uitgevoerd aan de hand van gedetecteerde weerballon signalen, zoals uitgelegd in hoofdstuk 5. De bekomen data wordt hieronder weergegeven:

Depth (m)	Station id	channels	Run:Event	$n_{\text{exponential}}$	n_{fit}
-48.155	21	6&7	1441:117	1.6400	$1.632 \pm 0.00128 \pm 0.00472$
-58.38	21	5&7	1441:117	1.6736	$1.66632 \pm 0.00226 \pm 0.00233$
-58.24	21	5&6&7	1441:117	1.67321	$1.66553 \pm 0.00167 \pm 0.00350$
-68.2	21	5&6	1441:117	1.6983	$1.69329 \pm 0.00199 \pm 0.00460$
-93.865	21	0&1&2&3	1441:117	1.73896	$1.71366 \pm 0.00287 \pm 0.05641$
-94.518	11	0&2&3	1034:12397	1.7397	$1.724 \pm 0.014 \pm 0.047$

CONTENTS

Dankwoord	I
Summary	II
Samenvatting	III
Introduction	1
1 Neutrino as Astroparticle	3
1.1 Discovery	3
1.2 The weak interaction	4
1.3 Neutrino sources	4
1.3.1 Cosmological/Primordial neutrinos	5
1.3.2 Solar neutrinos	6
1.3.3 Supernovae	7
1.3.4 Background from old supernovae	8
1.3.5 Atmospheric neutrinos	8
1.3.6 neutrinos from AGNs	9
1.3.7 Cosmogenic neutrinos	10
2 Radio neutrino detection	11
2.1 Neutrino interactions in ice	11
2.2 Askaryan effect	12
2.3 RNO-G	14
2.3.1 Hardware	14
2.3.2 Reconstruction: Lookup tables	17
2.4 Multi-Messenger Astronomy	17
3 Ray tracing	19
3.1 Wave propagation	19
3.2 Ice model	20

3.3	Shortcomings of the exponential ice model	23
3.4	Iterative ray tracer	23
4	Hybrid Ray tracer	25
4.1	How the hybrid ray tracer works	25
4.2	Performance Optimization	27
4.2.1	Length of the normal vector	28
4.2.2	ztol	28
4.2.3	Sphere Size & Step Size	28
4.2.4	Conclusion of optimization	35
5	Weather Balloon	36
5.1	Plane Wave Reconstruction	36
5.1.1	simple plane wave reconstruction	38
5.1.2	plane wave reconstruction using snell's law	39
5.2	Is the goal feasible?	41
5.2.1	Simple Plane Wave	41
5.2.2	Influence of the height on the systematic error	42
5.3	Fitting the index: Phased array	44
5.4	Phased array and channels 5-7	49
5.5	Evaluation of the results	49
	Conclusion	51
A	List of abbreviations	52
B	Extra Figures	53
C	Balloon passbys under 5° in the summer of 2022	55
D	Balloon passbys under 10° in the summer of 2022	58

INTRODUCTION

“Begin at the beginning,” the King said, gravely, “and go on till you come to an end; then stop.”

– Lewis Carroll, *Alice in Wonderland*

Outside our earth various kinds of events take place which we wish to observe: Black hole outbursts, supernovae, cosmic jets, ... These events produce various kinds of messengers like Gravitational waves, gamma rays, protons,... But one of these information carriers is unique and the subject of our study: The neutrino.

The neutrino has the special property that it points back to the event itself. Due to the neutrino not having any charge, nearly no mass and interacting weakly it doesn't get bent nor absorbed and re-emitted on its way to us unlike say the proton. This means that if we observe a neutrino back here on earth it's very likely that the direction we observe it in, is the direction it came from, the neutrino is explained more in-depth in chapter 1.

The neutrinos in the ultra high energy (UHE) range are of high importance to us. There have been lots of neutrino detectors around but none of them have been able to observe *cosmogenic neutrinos* which would have energies above the 3 PeV energy range. We probably haven't detected them as the flux falls exponentially with increasing energy, implying that a really big detector volume is required to detect neutrinos in reasonable timespans.

Both economically and logistically it makes sense to build a detector of the required size in ice and let it operate in the radio regime, as was previously explored in experiments like ARA and ARIANNA. To this end the Radio Neutrino Observatory in Greenland or RNO-G is currently under construction and how it detects neutrinos is explained in chapter 2.

The ice properties have an impact on how radio waves propagate. As mentioned before, RNO-G is a detector built in the Greenland firn. As the radio waves get produced in the ice we need to figure out how they propagate towards our detector. An important part in figuring out how they propagate is understanding the optical properties of the ice with a big factor being the local index of refraction. This index of refraction seems to be linearly related to the density of the ice which varies continuously with depth. So we need a model describing the overall index-depth

relation called an *ice model*, how this is used to understand how the rays propagate is explained in chapter 3.

The ice model currently used seems to be a sub-optimal fit to the index-depth data (as converted from the density-depth data). To both work with more complex models and convince people to work with those models, some work needs to be done.

In this thesis, in chapter 4, a new algorithm was developed which makes it possible to work faster and more accurate with complex ice models whom might follow the real index-depth profile closer. And as to try and show the discrepancy of the real index-depth relation to the model now widely used, plane wave reconstruction of observed weather balloon signals was carried out in 5.

NEUTRINO AS ASTROPARTICLE

When looking at phenomena outside our earth the astronomer will turn to electromagnetic radiation, but he's missing out on a big part of the full picture. Not only do interesting events emit photons but also muons, nuclei, gravitational waves,... All kinds of particles which might also be of interest, that's where the astroparticle physicist comes in.

Of all these particles there is one particle which has properties we're quite interested in: the neutrino. Neutrinos don't have any charge, meaning that they are not deflected by magnetic fields. Also neutrinos interact very weakly, because of this they are often called "ghost" particles; on average 100 trillion neutrinos pass through your body per second, none of them having any effect. You'd even need a light year of lead to give you just a 50% chance of stopping a neutrino. These properties makes them ideal messenger particles as, when we detect a neutrino and it's arrival direction, we can be quite sure it came to our detector unhindered from a far away event in the exact same direction. Neutrinos can serve as unique clues about what's happening elsewhere in the universe including the cosmic collisions, galaxies, supernovae, Gamma-ray bursts (GRBs),... Where they are created.

In this chapter we'll give an overview of neutrinos and the various kinds of energies we expect to see them in when coming from outside our earth.

1.1 Discovery

In the fifties researchers were investigating β^- decay, the decay of a neutron. In the proton-electron model for the β^- -decay of a nucleus (A,Z) you would expect the final result to be (A,Z+1) + e^- , or

$$n \rightarrow p^+ + e^- \quad (1.1)$$

However, after measuring the outgoing proton and electron energies, the researchers concluded that energy was lost somewhere and angular momentum wasn't conserved [1]. The solution postulated by Wolfgang Pauli was to introduce a new, really hard to detect particle with no charge and a very small mass: the neutrino, and his solution stands to this day. The neutrino comes in three flavors: electron, muon and tau neutrinos, each corresponding to their respective

lepton denoted as

$$\nu_e \quad \nu_\mu \quad \nu_\tau \quad (1.2)$$

and each also having an anti-particle.

$$\bar{\nu}_e \quad \bar{\nu}_\mu \quad \bar{\nu}_\tau \quad (1.3)$$

Now with the introduction of the neutrino the full β^- decay becomes

$$n \rightarrow p^+ + e^- + \nu_e \quad (1.4)$$

The inverse can then also be used to detect neutrinos:

$$\bar{\nu}_e + p^+ \rightarrow n + e^+ \quad (1.5)$$

This method was used in the Cowan–Reines neutrino experiment in 1956 with the anti-neutrinos coming from a nuclear reactor [2], making it the first experimental detection of a neutrino.

1.2 The weak interaction

As with the strong and electromagnetic interaction which interact via gluons and photons respectively, the weak interaction which is the primary way neutrinos interact, is also mediated by the exchange of elementary spin-1 bosons. Namely the charged bosons W^+ and W^- and the neutral Z^0 boson. Contrary to the gluons and photons however, these bosons are massive [3]:

$$M_W = 80.40 \text{ GeV} \quad M_Z = 91.19 \text{ GeV} \quad (1.6)$$

Following general arguments, it can be derived that the range of any force is given by the Compton wavelength of the particles transmitting it [4], as the Compton wavelength is given by

$$\lambda = \frac{h}{mc} \quad (1.7)$$

The very large masses of the "force carriers" imply a very short-range interaction, in the order of 10^{-3}fm and can even be treated as a zero-range interaction at low energies.

The charged bosons couple to neutrinos via the *charged current* interaction:

$$\mathcal{L}_{int}^\nu = \sum_\ell -\frac{g}{\sqrt{2}} \bar{\nu}_\ell^L W \ell^L - \frac{g}{\sqrt{2}} \bar{\ell}^L W^\dagger \nu_\ell^L \quad (1.8)$$

With the L denoting left handed, note thus that only left-handed neutrinos interact. For the neutral boson we analogously have the *neutral-current* interaction:

$$\mathcal{L}_{int}^\nu = \sum_\ell -\frac{g}{2 \cos \theta_W} \bar{\nu}_\ell^L \not{Z} \nu_\ell^L \quad (1.9)$$

These bosons can also couple to quarks, making it possible to detect neutrinos via their interaction with nuclear matter which we'll get to in chapter 2.

1.3 Neutrino sources

As shown in figure 1.1 there are various kinds of neutrino sources. We'll discuss these one by one in order, leaving out the reactor anti-neutrinos and the terrestrial anti-neutrinos as we're only interested in neutrinos of astrophysical nature. The ones we'll thus discuss are the cosmological, solar, supernova, background from old supernovae, atmospheric, AGN and cosmogenic neutrinos.

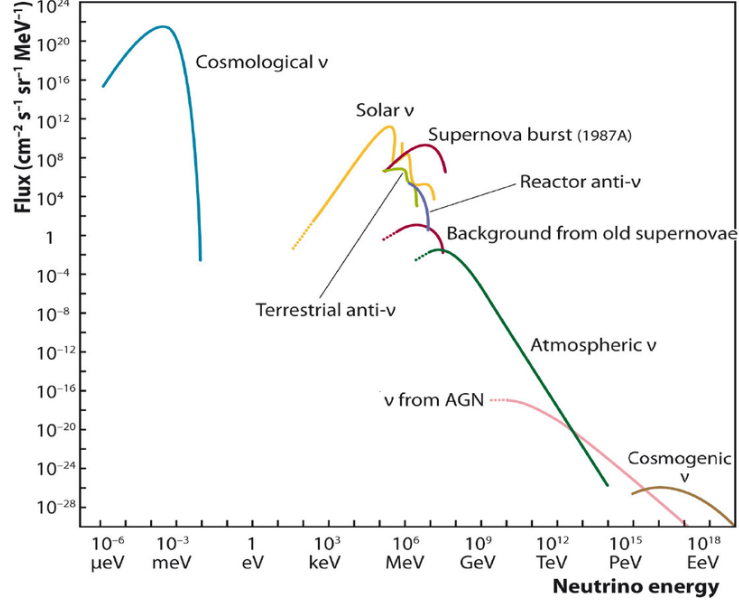


Figure 1.1: Less neutrinos will be observed for higher energies [Fig1]

1.3.1 Cosmological/Primordial neutrinos

The first source of neutrinos we'll talk about is the one in blue to the left of the figure termed the *Cosmological neutrinos*: the neutrino version of the CMB. To understand this source we'll have to go back all the way to just after the big bang: The very early universe was hot and dense. As a result, interactions among particles occurred much more frequently than they do today. As an example, a photon today can travel across the observable universe without deflection or capture, so it has a mean free path greater than 10^{26} m. When the universe was 1 second old, though, the mean free path of a photon was about the size of an atom. Thus in the time it took the universe to expand by a factor of 2, a given photon interacted many, many times. These multiple interactions kept the constituents in the universe in thermal equilibrium. But as the universe expanded there were times when reactions could not proceed rapidly enough to maintain equilibrium conditions, these particles then fall out of thermal equilibrium. This falling out of equilibrium is termed *decoupling*. And we're interested in when neutrinos decoupled. Neutrinos were kept in equilibrium through the interaction

$$\nu e \leftrightarrow \nu e \quad (1.10)$$

Up until the universe cooled down to about 1MeV when they decoupled. To estimate the temperature of the neutrinos who decoupled at the start of the universe, we can take a look at conservation of entropy [5] from which we'll find that the temperatures are related by:

$$T_\nu = \left(\frac{4}{11}\right)^{1/3} T_\gamma \quad (1.11)$$

Note that they decoupled before the photons making them lower in temperature. As T_γ is the CMB temperature which, nowadays, is measured to be around 2.7K or 2.3×10^{-4} MeV. This would imply $T_\nu = 1.66 \times 10^{-4}$ MeV which is roughly where the peak flux is located. These primordial neutrinos are thus very low in energy.



Figure 1.2: Two electron neutrinos get released over the full fusion cycle [Fig2]

1.3.2 Solar neutrinos

The sun fuses elements via the pp chain reaction to release energy and thus keeping itself from collapsing in on itself, in most of the various fusion steps, neutrinos get released as is shown in figure 1.2 where the neutrinos are electron neutrinos. Now with this and some information about the sun like the pressure and mass, the *standard solar model* was made. This model predicted a certain amount of electron neutrinos to be hitting the earth from the previously mentioned thermonuclear fusion, it was however 3 times higher than the observed amount of electron neutrinos back at our planet [6], this was called the *Solar neutrino problem*. The solar neutrino problem led to a some hysteria as this could've meant that the sun was dying and we'd see the aftermath only in a couple of years. This phenomenon was theoretically resolved by assuming [7] the different kinds of neutrinos to oscillating into each other on their way to earth, i.e 2/3 of the original electron neutrinos had oscillated into mu and tau neutrinos. But for them to oscillate into each other, they not only require mass but each flavor also should have a different mass as can be seen from an example 2D approximation to the transition probability [8]:

$$P(\nu_e \rightarrow \nu_\mu) = |\langle \nu_\mu | \psi(L, T) \rangle|^2 = c_\mu c_\mu^* = \sin^2(2\theta) \sin^2\left(\frac{\Delta\phi_{12}}{2}\right) \quad (1.12)$$

with

$$\Delta\phi_{12} \approx \frac{m_1^2 - m_2^2}{2p} L \quad (1.13)$$

In full generality (3D):

$$|\nu_\alpha\rangle = \sum_i U_{\alpha i} |\nu_i\rangle \quad (1.14)$$

With $U_{\alpha i}$ the Pontecorvo-Maki-Nakagawa-Sakata (PMNS) matrix [9]. This phenomenon has been experimentally verified e.g through the discrepancy from the observed and expected neutrino events coming from a nuclear reactor [10].

It was later found that the oscillation of the neutrinos was further enhanced through the Mikheyev–Smirnov–Wolfenstein effect, whereby neutrinos oscillate more in matter of varying density (like the sun) [11].

1.3.3 Supernovae

Supernovae produce a lot of neutrinos, to understand when in a supernovae they get released we'll have to go over the current theoretical understanding of how a supernova occurs.

A star starts its life as a ball of pure hydrogen. At the core, due to the gravitational pressure of the outside plasma, fusion of hydrogen into deuterium and helium happens. Thus converting mass into energy. The pressure of this energy counteracts the pressure of gravity and the star is stable.

When the hydrogen at the core runs out no more hydrogen can be fused. For stars with masses between $8M_{\odot}$ and $30M_{\odot}$ (M_{\odot} being the mass of the sun) the fusion of heavier elements starts, this can't keep going on however as at some point the star starts to form the most stable element: iron.

It costs energy to both make lighter elements than iron and heavier ones as can be seen on the energy curve shown on figure 1.3. As the iron core builds up the outside pressure from

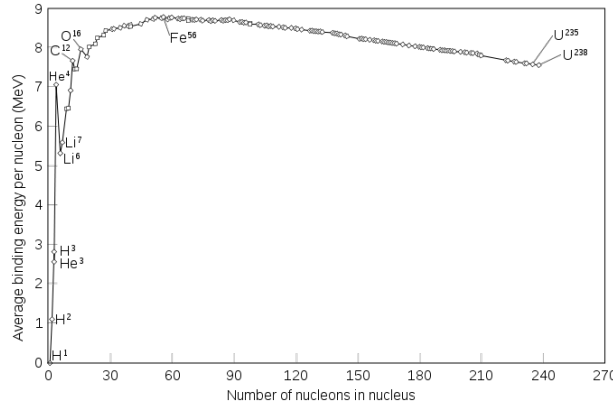


Figure 1.3: Iron is at the top and is thus the most stable atom [Fig3]

the core starts to decrease as no new energy is released. This goes on until the threshold of an iron core with a mass of $1.4M_{\odot}$ known as the Chandrasekhar limit [12] [13] is reached and the inwards pressure becomes too large compared to the outward pressure, making the electrons surrounding the iron core fuse with the protons (uud), creating neutrons (udd) and neutrinos, diagrammatically shown in figure 1.4.



Figure 1.4: fusion of protons with surrounding electrons into neutrons via charged current exchange

This last part happens in a split second as the collapse goes at 25% the speed of light, creating a very dense neutron star (3000km in diameter iron core to 30km in diameter neutron star) and

up to 10^{52} ultra-relativistic neutrinos, carrying up to 99%¹ of the released energy [14]. As the density has suddenly increased so much there's a huge distance of pure vacuum between the plasma outer layer and the (now) neutron star. This plasma starts free-falling inward, also at 25% the speed of light whilst the neutrinos carrying tremendous amounts of energy start going outward from the neutron stars core.

The neutrinos then collide with the plasma resulting in what we observe as a "supernova", wrongly thought of by Kepler as being a "new (nova) star" rather being a violent death of an old star.

This is quite unexpected as neutrinos rarely interact, it's only as the incoming plasma is so dense and due to the tremendous amount of neutrinos that collisions happen at all. Some, however, escape and will be visible on earth in our neutrino detectors ≈ 18 h before the light escapes the exploding star.

Neutrino observatories can thus be useful to know where to point our various telescopes before the supernova is actually visible in the night sky.

1.3.4 Background from old supernovae

Also termed the *diffuse supernova neutrino background* (DSNB), as the universe is quite old various supernovae have happened over it's lifetime, each generating a lot of neutrinos as was discussed in section 1.3.3. This is postulated to have generated a continuous neutrino background [15].

1.3.5 Atmospheric neutrinos

Before we can talk about atmospheric neutrinos it's necessary to discuss *cosmic rays*. Cosmic rays are ionized nuclei of which 90% are protons, 9% are alpha particles and the rest are heavier nuclei. Almost all of them originate from outside the solar system but from within our galaxy. The few particles that do come from our solar system can be temporally linked to violent events on the sun. In contrast to this the particles coming from outside our solar system show an anti-correlation with the sun as they can more easily reach the earth if solar activity is low. It has been observed that the major components of the cosmic ray elements roughly follow an inverse power law in energy, with differential flux [16]

$$\frac{dN}{dE} \propto E^{-(\gamma+1)} \quad (1.15)$$

Cosmic rays particles hit the Earth's atmosphere with a flux of about 1000 rays per square meter per second and interact with atomic nuclei in the Earth's atmosphere, creating showers of particles. Many of these showers consist of particles which are unstable and produce neutrinos when they decay. These neutrinos are what's called *Atmospheric neutrinos*. Most notably neutrinos can be produced together with muons in the two-body decays of charged pions and kaons wherever these hadronic interactions occur. The most important production channels and their branching ratios for neutrinos are:

$$\pi^\pm \rightarrow \mu^\pm + \nu_\mu(\bar{\nu}_\mu)(\sim 100\%) \quad (1.16)$$

$$K^\pm \rightarrow \mu^\pm + \nu_\mu(\bar{\nu}_\mu)(\sim 63.5\%) \quad (1.17)$$

Neutrinos are subsequently also produced when these muons decay:

$$\mu^\pm \rightarrow e^\pm + \nu_e(\bar{\nu}_e) + \bar{\nu}_\mu(\nu_\mu) \quad (1.18)$$

¹ $\approx 1\%$ is released as kinetic energy, only 0.001% as electromagnetic radiation

which is a process mainly happening at low energies in the atmosphere. As the Kaons are CP violating particles, a beam of neutral kaons produced by cosmic rays will decay in flight making the short-lived K_S (K-Short) disappear and leave a pure beam of long-lived K_L (K-Long) [17]. Another decay which is therefore important and the dominant source for electron neutrinos for energies $E_\nu \geq 1\text{GeV}$ is the K_L decay

$$K_L \rightarrow \pi^\pm e^\mp \nu_e (\bar{\nu}_e) \quad (1.19)$$

The atmospheric neutrino spectrum shown in figure 1.1 roughly follows a power spectrum as the cosmic ray flux follows a power spectrum. But the correspondence isn't one-to-one as, due to the difference in kinematics, the contribution from kaons to neutrinos is significantly more important than to muons, especially at high energies.

How well can we detect these atmospheric neutrinos coming from cosmic rays? The primary way to detect neutrinos is through neutrino-nucleon interactions. The cross section for producing a charged lepton [16] in the 1-3000 GeV region is

$$\sigma \approx 0.5 \times 10^{-38} \text{cm}^2 \times E_\nu (\text{GeV}) \quad (1.20)$$

The neutrino flux at 1 GeV is $\sim 1\text{cm}^{-2}\text{s}^{-1}$ from all directions, the interaction rate for atmospheric neutrinos is thus of the order

$$\sim 100 \frac{\nu\text{-interactions}}{\text{kTyr}} \quad (1.21)$$

With kT denoting kilotons, therefore detectors of a kiloton or more sensitive volume are required to study interactions of cosmic ray neutrinos [18].

1.3.6 neutrinos from AGNs

An AGN (active galactic nucleus) is deemed to be the reason why several abnormal galaxies exist with an extra bright (and mostly variable) light source in their core which even the biggest of telescopes can't spatially discern. The general consensus is that this phenomenon is caused by one particular kind of object: a supermassive black hole (a black hole with a mass of at least $105M_\odot$) surrounded with a close torus of dust and gas [19]. This torus of gas is called an *accretion disc* and is an enormous source of energy. The conversion of potential energy of the incoming gas to highly energetic radiation is a very complex physical process with which we have to account for various factors like gravitational instabilities, magnetic fields, hydrodynamical turbulence,... And thus produces a spectrum that's quite complex. It would appear that the luminosity of an AGN would increase indefinitely with incoming mass, but this process is limited: if too much matter accretes on the black hole the radiative pressure becomes too massive and the matter on the disc gets blown away. This phenomenon is termed a *black hole outburst*.

The emission of high energy neutrinos from AGNs rests solely on the premise that relativistic protons of sufficiently high energy and energy density in the AGN's accretion disc will be present [20] as they may interact to create e.g pions whom decay into neutrinos. A direct consequence of the occurrence of these relativistic protons is the production of γ -rays of similar energies to those of the neutrinos, thus high energy neutrino- and γ -ray astronomy are closely related. However, even though γ -ray photons can be produced even in the absence of relativistic protons (e.g via high energy electrons), neutrinos can not. Thus the detection of these high-energy neutrinos (which might have already been detected [21]) will provide unique information about the workings of AGNs. As these ultra high energy neutrinos get produced near the source (the AGN) they are what's called *astrophysical neutrinos*

1.3.7 Cosmogenic neutrinos

In contrast to the previous source of UHE neutrinos which was generated at the source, called *astrophysical neutrinos* we'll now talk about UHE neutrinos whom are generated through the interaction of ultra-high energy cosmic rays during propagation with the cosmic microwave or other photon backgrounds termed *cosmogenic neutrinos*.

If a proton has sufficiently high energy the cross section to interact with the CMB (Cosmic Microwave Background) becomes non-negligable and it may scatter off the photons to resonantly produce a Δ^+ baryon. This resonance has enough mass to dominantly decay to a pion and a nucleon [22]:

$$\Delta^+ \rightarrow \pi^0 + p \quad (2/3) \tag{1.22}$$

$$\Delta^+ \rightarrow \pi^+ + n \quad (1/3) \tag{1.23}$$

Of which the charged pion decays to neutrinos as previously mentioned in 1.3.5 whom are very high energy. This phenomenon is also predicted to cause the so-called Greisen–Zatsepin–Kuzmin [23] [24] limit. As, due to this interaction, there would be a limit to the energy a cosmic ray protons might have and still pass the intergalactic medium from another galaxie to our galaxy. This limit is theorized to be $5 \times 10^{19}\text{eV}$ (50 EeV).

RADIO NEUTRINO DETECTION

In this chapter I'll explain how astrophysical neutrinos get detected in the context of the Radio Neutrino Observatory in Greenland, or RNO-G.

Neutrinos are omnipresent in nature but as they interact very weakly we'll need a big detector to detect reasonable amounts in finite timespans. To this end we can make use of a detector volume nature has built for us: the Greenland icecap. Even though various detector media have been used, like water [25], heavy water [26] and even the moon [27], ice has been chosen as it has a few properties which makes it easy to work with, of which some are listed below:

- Ice is mostly see-through for electromagnetic radiation in the radio-frequency range
- The Greenland icecap is a really big continuous volume with little to no background from human activity
- As it's really cold within the ice, the detectors don't have to be made water-tight (contrary to in-water detectors)
- As ice is a solid the detectors are logistically easy to deploy

To detect a neutrino it has to generate some kind of signal, as will be explained, neutrinos can interact with hadronic matter to produce charged particles. For cubic-kilometer type in-ice detectors these charged particles can then be detected through the Cherenkov effect in the visible spectrum or through the Askaryan effect in the radio frequency range. For RNO-G the Askaryan effect will be leveraged.

2.1 Neutrino interactions in ice

As neutrinos propagate through ice they can interact weakly with the nuclei (see section 1.2). The main mechanisms of interaction is via charged- and neutral current exchange with the quarks [28] as is also depicted in figure 2.1.

The produced leptons in the W boson mediated interaction are either electrons, resulting in an electromagnetic shower, muons which typically live too long and thus escape before they deposit



Figure 2.1: Most prominent ways of neutrino-nucleus interaction

all their energy in the ice or taus which will decay via

$$\tau^- \rightarrow e^- + \bar{\nu}_e + \nu_\tau \quad (2.1)$$

or, less ideally

$$\tau^- \rightarrow \mu^- + \bar{\nu}_\mu + \nu_\tau \quad (2.2)$$

In both the charged and neutral current interaction, the resulting nucleus will result in an hadronic shower. For the neutral current interaction the fraction of the neutrino energy that gets transferred to the nucleon is described by the inelasticity y and is heavily shifted towards small values of y [29]. This causes a big, irreducible uncertainty when trying to estimate the original neutrino energy from these kinds of events. With the charged current interaction (mediated by the W^\pm bosons) this isn't a problem however as the full neutrino energy ends up in the resulting cascades.

2.2 Askaryan effect

A particle shower formed through the previously described interaction in ice can emit strong radio signals if two conditions are met:

- There is separation of positive and negative charges in the shower front
- The signals produced over the length of the shower profile overlap coherently.

The *Askaryan* [30] effect, which is responsible for the production of Askaryan radiation describes the effect at radio frequencies which abides by both of these conditions. In general it's a quite involved effect but we'll give a crude overview. After neutrinos interact in the ice they produce a cascade of secondary charged particles containing a net negative charge anisotropy [31]. This charge imbalance is a result of medium electrons either Compton scattering into the advancing shower or annihilating with shower positrons. This moving charge anisotropy is propagating faster than the speed of light in the dielectric medium, creating Cherenkov radiation.

Cherenkov radiation can be considered the electromagnetic equivalent of a sonic boom. A sonic boom happens when an object goes faster than the speed of sound in the medium; In the same way a particle emits Cherenkov radiation if it propagates faster than the speed of light in the medium. Choosing the particle trajectory to lie along the z axis an approximate equation can be found [32] for $\frac{d^2 \mathcal{J}}{d\omega d\Omega}$, which is the energy radiated per elementary unit solid angle and per elementary unit frequency interval:

$$\frac{d^2 \mathcal{J}(\omega)}{d\omega d\Omega} = \frac{q^2}{4\pi} \sqrt{\frac{\mu}{\epsilon}} \beta^2 \omega^2 \delta^2[\omega(1 - \beta \mathbf{e}_r \cdot \mathbf{e}_z)] |\mathbf{e}_r \times \mathbf{e}_z|^2 \quad (2.3)$$

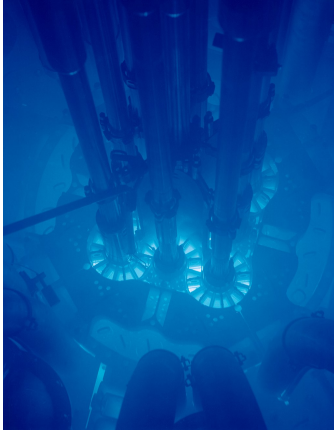


Figure 2.2: The particles coming from the reactor core produce cherenkov radiation as they pass through the water, most of the produced light is "in blue" [Fig4]

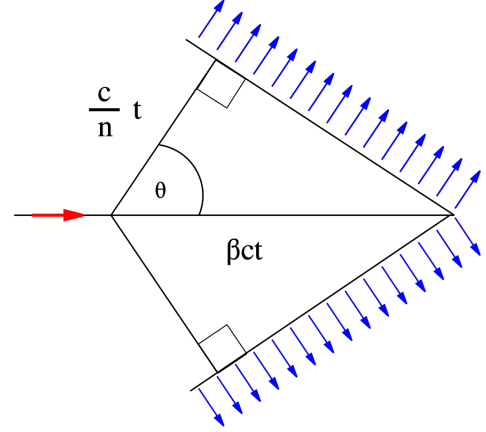


Figure 2.3: The cone shape is reminiscent of a sonic boom, the signal is the strongest on the cone [Fig5]

Now we can re-write this equation in spherical coordinates, which gives $1 - \beta \mathbf{e}_r \cdot \mathbf{e}_z = 1 - \beta \cos(\theta_c)$ in the delta function. We thus only expect radiation if

$$\cos(\theta_c) = \frac{1}{\beta} = \frac{c'}{u} = \frac{c}{n} \cdot \frac{1}{u} \quad (2.4)$$

With u the local speed of light in the medium and n the index of refraction, an optical property of a medium which we'll later on thoroughly discuss. If $u > \frac{c}{n}$, Cherenkov radiation will be emitted along a cone surface with half angle $\frac{\pi}{2} - \theta_c$ as illustrated in figure 2.3. Integrating equation 2.3 over the solid angle and formally dividing by the time interval we get:

$$\frac{d^2 \mathcal{J}}{d\omega dt} = \frac{q^2}{4\pi} \sqrt{\frac{\mu}{\epsilon}} \beta \omega \left(1 - \frac{1}{\beta^2} \right) \quad (2.5)$$

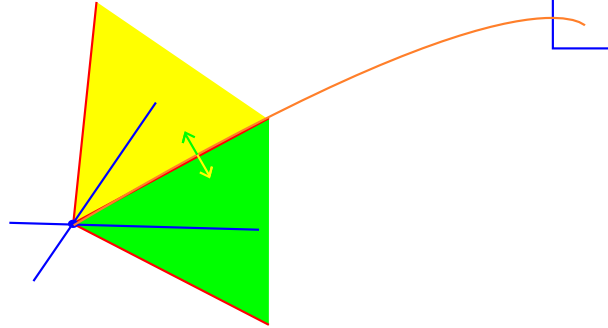
We see that the energy is proportional to ω , so we expect that most radiation will be emitted "in blue" with a cut-off frequency above which the equation $\cos \theta = 1/(n\beta)$ can no longer be satisfied. This "in blue" characteristic is responsible for the blue glow seen in nuclear reactors as seen in figure 2.2. For ice the index of refraction is roughly 1.78 in deep ice [33], so we expect an ultra-relativistic particle to produce the most radiation at around 56° opening as

$$\cos(\theta_c) \approx \frac{1}{n} \implies \cos^{-1} \left(\frac{1}{1.78} \right) \approx 56^\circ \quad (2.6)$$

Of course this is just an estimate, as the actual index of refraction is depth-dependent which we'll get to in section 3.2. Now this explains how the signals get generated but logically, from only knowing this we'd expect radio waves to almost be non-existent due to the "in blue" nature of Cherenkov radiation.

To understand why this isn't the case we'll need another piece of the puzzle: coherent overlap. Coherent overlap in the radio wave spectrum range can be intuitively explained as follows: generally the shower is of length $\mathcal{O}(10\text{cm})$ [34], over this length the radiation gets emitted, most frequencies decoherently interfering, but radio waves with wavelengths of $\approx 10\text{cm}$ coherently interfere, and it's these waves we then wish to detect. The radiation generated through this Askaryan effect is called *Askaryan radiation*.

The Askaryan radiation is polarized perpendicular to the Cherenkov cone, this can be useful to discern between different Cherenkov cones whom, timely, would generate the same response. This concept is illustrated below in 2D where two neutrinos from different directions would generate the same signal in a non-polarized detector.



If the detector has a way to differentiate between polarization however, there would be no doubt where the neutrino originated from as the one producing the yellow Cherenkov cone would have a downwards polarization and the one producing a green Cherenkov cone would have an upwards polarization, note that in 3D infinite different Cherenkov cones could generate the same timely signal (think of rotating the cone around a line on the cone) so both vertical and horizontal polarization information is needed.

2.3 RNO-G

Both cosmic ray and neutrino detectors face the same main problem at the highest energies: the steeply falling flux (as was previously seen in figure 1.1) requires large effective areas, which leads to the construction of neutrino detectors with volumes on the cubic kilometer scale like IceCube [35] which works on the principle of detecting neutrinos with visible light. But even IceCube has its limitations, it's still too small to observe many neutrino events above the 10 PeV scale [36] in acceptable timescales. That's why a new detector was needed which was even bigger and able to observe cosmogenic neutrinos. We could just make IceCube bigger but this would cost a lot of money as the individual detectors need to be spaced closely as the attenuation length is quite short for light in the visible spectrum propagating through ice.

The proposed solution was to work with radio wave detectors, leveraging the previously discussed Askaryan effect (see section 2.2). Radiowaves can propagate way further in ice than visible light making it possible to space the individual detectors further apart. The proposed location is Greenland, an island country in North America and part of the Kingdom of Denmark which has large ice sheets as shown in figure 2.4. The proposal for RNO-G, which was later funded and now in the construction phase, is for it to be an array of autonomous radio stations each of which having both surface channels and various deep channels resulting in a total of 24 channels per station. The whole project builds heavily on the knowledge obtained through previous radio based neutrino detectors like the NuMoon [27] project, ANITA [37], ARA [38], ARIANNA [39] and RICE [40].

2.3.1 Hardware

A station is illustrated in figure 2.5, the plan is to build 35 of these as is shown in figure 2.8. Looking closely at one such detector we see just below the surface 9 Log Periodic Dipole Antennas (LPDAs), these are used to detect air shower muon signals as muons will also generate Cherenkov radiation in the ice whose signals can then be filtered out. Aside from these surface



Figure 2.4: orthographic projection of Greenland with the red star representing the approximate RNO-G location [Fig6]

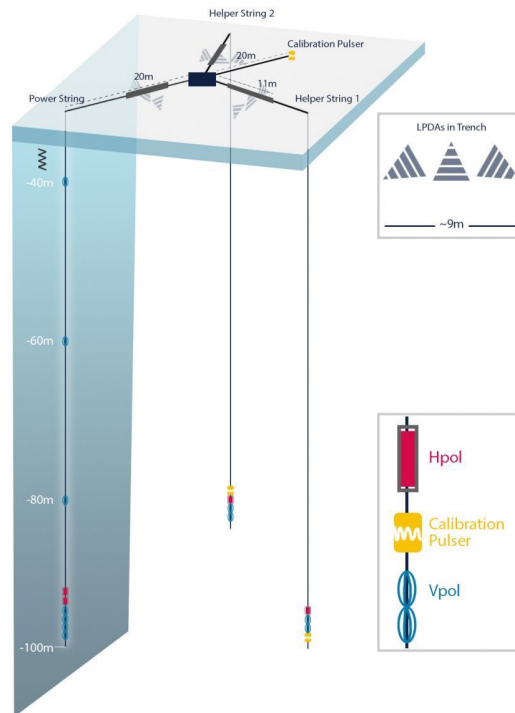


Figure 2.5: The combination of Vpol and Hpol antennae makes it possible to discern the direction of neutrinos whereas the surface LPDA antennae makes it possible to distinguish muons. [Fig7]

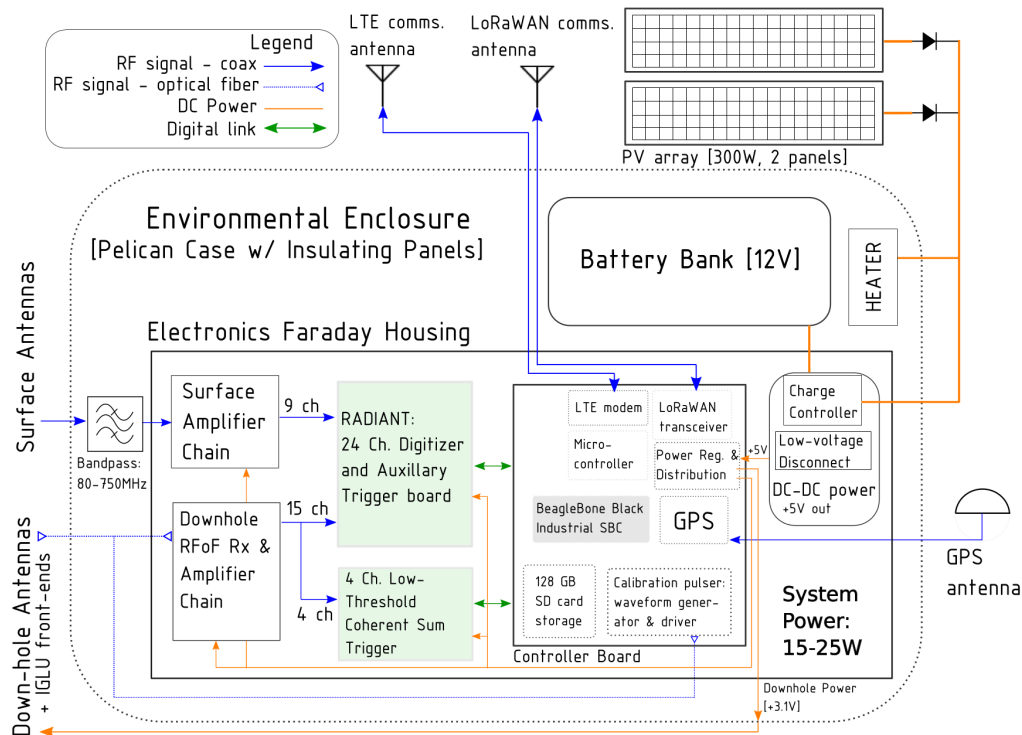


Figure 2.6: System diagram for a RNO-G station [Fig8]

detectors there are also deep components of the detector which can be split up in three parts: Two *helper strings* and the *power string*.

The helper strings are the 2 vertical cables shown on the right of figure 2.5 each housing 2 vertically polarized antennas (Vpols), one quadslot antenna for the horizontal polarization component (Hpol) and one radio pulser on each helper string which can be used to generate calibration signals. As was previously mentioned the polarization can be used to distinguish between possible Cherenkov cones generating the same resulting pulse, that's why both the helper and power string are equipped with both kinds of polarized antennae.

The power string (the leftmost vertical cable) is more densely instrumented than the helper strings: At the bottom it houses a set of four Vpol and two Hpol antennas with a spacing of 1m called the *phased array* [41]. Arguably the most important channels in a station as it's spaced closely together and can thus use the principle of phasing the channels to get higher precision. Further up the string, with a spacing of 20m, are three more Vpol antennas.

A full system diagram for a RNO-G station is shown in figure 2.6, I'll give a walk through of how data gets collected. The signal from each of the deep antennae are fed into a low-noise amplifier directly above it, from there the signal is sent to the data acquisition (DAQ) system at the surface via a Radio Frequency over Fiber (RFOF) cable. The signals coming from the surface antennae are first passed through a Bandpass filter of 80-750MHz¹ after which both the resulting signals and the deep component signals get sent up to the RAdio DIgitizer and Auxiliary Neutrino Trigger (RADIANT). There it's again amplified, digitized and, if a trigger threshold is reached, saved onto an SD card. This data is then transmitted via a Long Term Evolution (LTE) telecommunications network to a local server², from where it is sent via a

¹i.e a filter that only lets frequencies in this range pass

²There is additionally a Long Range Wide Area Network (LoRaWAN) antenna as backup in case of problems

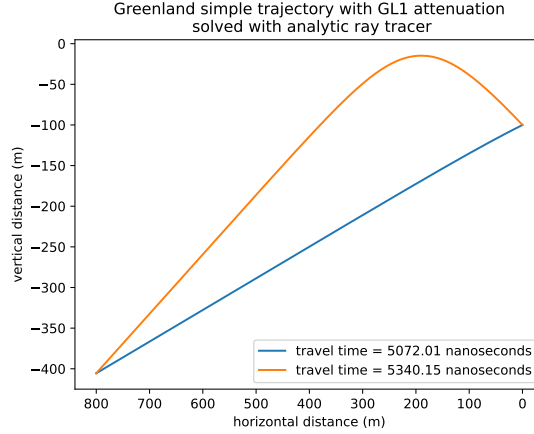


Figure 2.7: example simulation showing both direct and refracted path from a neutrino vertex (bottom left) to a detector (top right)

satellite link. As a power source, battery banks are used whom are charged via solar panels. But as there isn't enough light during the Greenland winters, there are plans to build wind turbines (with one of the problems being the possibly detectable RF noise the 'engine' would produce).

As was previously explained the radio signal from a neutrino often travels along both direct and refracted paths, designated DnR, to the deep array (as shown on figure 2.7). This double pulse characteristic would be a smoking-gun signature of an in-ice source. The two helper strings are needed for a full direction reconstruction. Three independent measurements are needed for azimuthal information, which is provided by the Vpol (Vertical polarization) antennas and placing the Hpol (Horizontal polarization) antennas at different depths on every string, both zenith and azimuth information will be provided for those signals. The helper strings' calibration pulsers, as well as one on the surface, will ensure regular monitoring of the performance of the station and provide information useful for precise calibration of the antenna geometry.

2.3.2 Reconstruction: Lookup tables

The main simulation code we'll be using consists of 2 parts: NuRadioMC [42] and NuRadioReco [43]. NuRadioMC uses Monte Carlo simulations to generate neutrino events in the ice and simulates how they propagate to the various channels, which will be covered more in-depth in the next chapter. NuRadioReco is reconstruction software, it simulates how the various detectors would respond to the detected radio waves. This simulation software is needed as the plan is to simulate a lot of neutrino events and record the detector responses in a giant database, then, when an actual neutrino event occurs, we'll only have to look in the database and match the actual detector response to the simulated detector responses, thus finding the origin.

2.4 Multi-Messenger Astronomy

The origin of the most energetic cosmic rays is still not conclusively identified. One approach to solving this problem is *multi-messenger astrophysics*, where several types of cosmic particles are used to identify the sources of these ultra-high energy cosmic rays (UHECRs). E.g we

with the LTE network

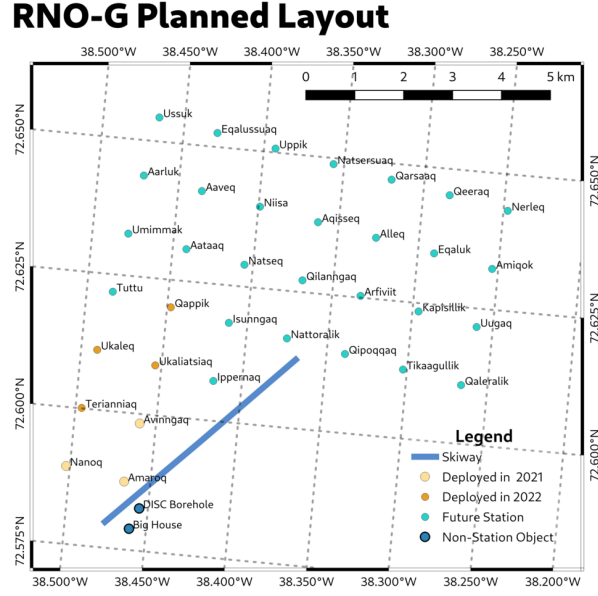


Figure 2.8: All the individual detectors are numbered but also named after various species living in Greenland (in the native tongue) [Fig9]

simultaneously measure gravitational waves with the Einstein telescope, neutrinos with RNO-G, photons with various telescopes and muons with a muon detector.

RAY TRACING

As previously hinted it is necessary to be able to simulate how radio waves propagate through the ice for various reasons like building up a database, calibrating channels,...

It will also become necessary in the last chapter for doing actual measurements, that's why in this chapter we'll give a brief introduction to the way radio wave paths are found within the NuRadioMC framework.

3.1 Wave propagation

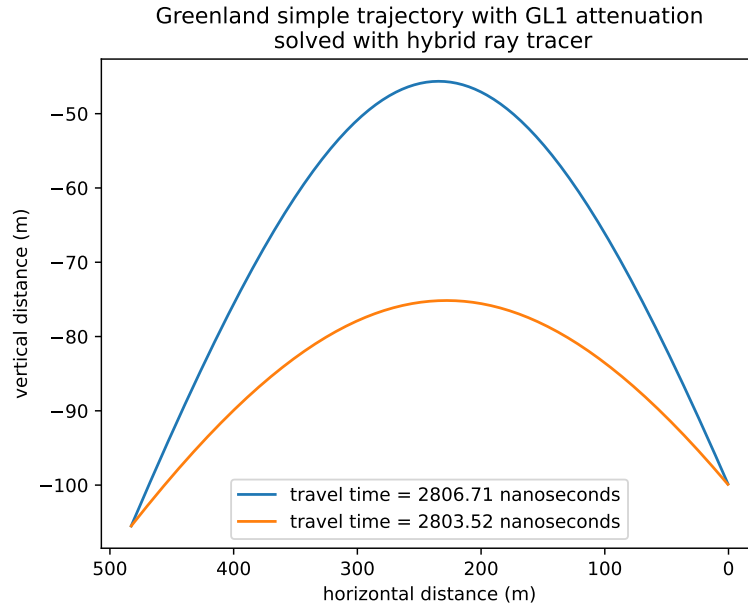


Figure 3.1: illustration of radio wave paths generated by a neutrino event

The way we simulate the strongest waves propagating to the detector from a radio source is through ray tracing, an illustration of such a simulation is shown in figure 3.1. Here the detector

is located at (0,-100) and a radio source at (480,-108), note that there are two possible paths leading to the detector.

The amount of solutions and how the waves are bent are consequences of the properties of the ice we work in. In a dielectric medium a ray propagates with it's signal wave-speed determined by the local index of refraction as $v = c/n$. The effect on speed isn't the only effect the index of refraction has which we'll need to concern ourselves with. However, if a ray propagates towards a boundary dividing 2 media with different indexes of refraction, the ray will refract and the refracted angle can be found from Snell's law:

$$n_i \sin \theta_i = n_o \sin \theta_o \quad (3.1)$$

Where n is the index of refraction, θ the angle with respect to the surface normal and "i" and "o" indicating incoming and outgoing respectively. The system we'll consider however, isn't homogeneous with some specified boundary. Ice in Greenland has a continuously varying density and index of refraction.

How do we know how the waves propagate in a medium? The software we'll be using to simulate how the radio waves behave is called *Radiopropa* [44]. As simulations of the wave propagation in full detail with the finite-differences-time-domain (FDTD) technique [45] are, even though they are more accurate, too time consuming. The authors of radiopropa opted to build their program on geometrical optics, i.e ray tracing. A path of a ray $\mathbf{r}(s)$ with path parameter s in a medium with index of refraction $n(\mathbf{r})$ is described by the eikonal equation [46]:

$$\frac{d}{ds} \left(n(\mathbf{r}) \frac{d\mathbf{r}}{ds} \right) = \nabla n \quad (3.2)$$

in radiopropa the local paraxial approximation (small angle approximation) is used, i.e if we assume that in any individual step of the algorithm the change of the refractive index along the path ds is small it's possible to re-write the equation as:

$$n(\mathbf{r}) \frac{d^2 \mathbf{r}}{ds^2} \approx \nabla n \quad (3.3)$$

Which is then iteratively solved using the Cash–Karp method. The way you would go about using this program is thus: find a start and end point (e.g a supposed neutrino interaction point and a detector respectively), "shoot" your ray in a certain direction for which the path will then be iteratively solved using radiopropa. And if you chose your direction right you have the path a ray might take from your start to the end point. The difficulty is this direction choosing which we'll get to later. If there are boundaries (such as defects or the surface) these are treated separately using Snell's law.

3.2 Ice model

Ice has a density gradient which we'll need to account for. Due to the way the ice bonds there will be more air trapped in between the molecules closer to the surface than at greater depths where the pressure due to the overhead ice prevents this. Due to this air being trapped the density of ice will be smaller closer to the surface than at greater depth.

Purely from classical gravity and density considerations it can be derived that the density scales exponentially. To see this let's consider a sheet of ice in the Greenland firn with a surface A and a height dz , the extra pressure this sheet of ice exerts on the ice just below it is:

$$d\sigma = \frac{dF}{A} = -\frac{g dM}{A} = -g \frac{A \rho(z) dz}{A} = -g \rho(z) dz \quad (3.4)$$

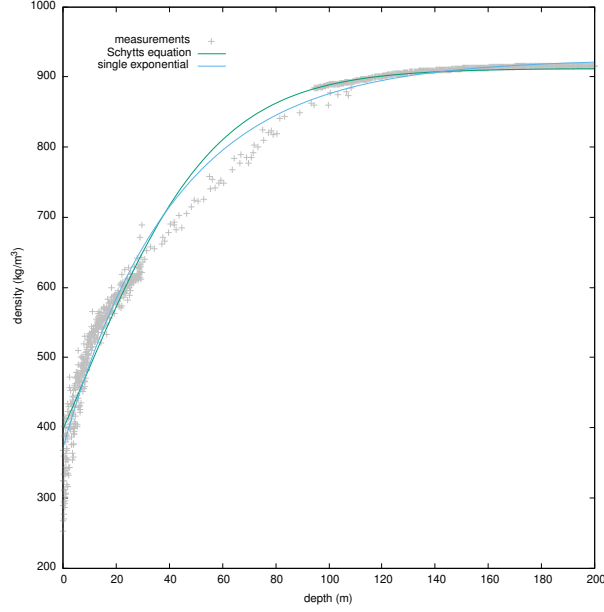


Figure 3.2: Illustration of the shortcomings of the analytical models

with $\rho(z)$ the depth-dependent density. Robin assumed the proportional change in air space to be proportional to the change in pressure [47]:

$$\frac{dV}{V} \propto d\sigma \quad (3.5)$$

As the volume scales inversely with the density let's assume the relation $V \propto (\rho_i - \rho)$ with ρ_i the density of pure ice, this yields:

$$\frac{d\rho}{\rho_i - \rho} \propto \rho dz \quad (3.6)$$

$$\frac{d\rho}{\rho(\rho_i - \rho)} \propto dz \quad (3.7)$$

Which can be solved to give

$$\rho = \frac{A\rho_i e^{z/z_0}}{1 + Ae^{z/z_0}} \quad (3.8)$$

Schytt also empirically fitted the following function:

$$\rho = \rho_0 e^{z/z_0} + B \quad (3.9)$$

Figure 3.2 shows how both of these functions fit the density curve¹. There is one big downside however. It seems that the ice actually doesn't follow these exponential curves perfectly.

Equation 3.3, and thus the path, depends on the index of refraction on a given location. The dependence of the dielectric constant on density for ice can approximately be given by [48]:

$$\epsilon(z) \approx (1 + 0.845\rho(z))^2 \quad (3.10)$$

Here ρ is called the *specific gravity* as to make the equation dimensionally correct, this is the same as the density in g/cm^3 but stripped off it's units. As the dielectric constant is the square of the index of refraction we can find an approximate index-density relation:

$$n(z) \approx 1 + 0.775 \frac{\rho(z)}{\rho_0} \approx 1 + 0.78 \frac{\rho(z)}{\rho_0} \quad (3.11)$$

¹The density with depth data can be found [here](#)

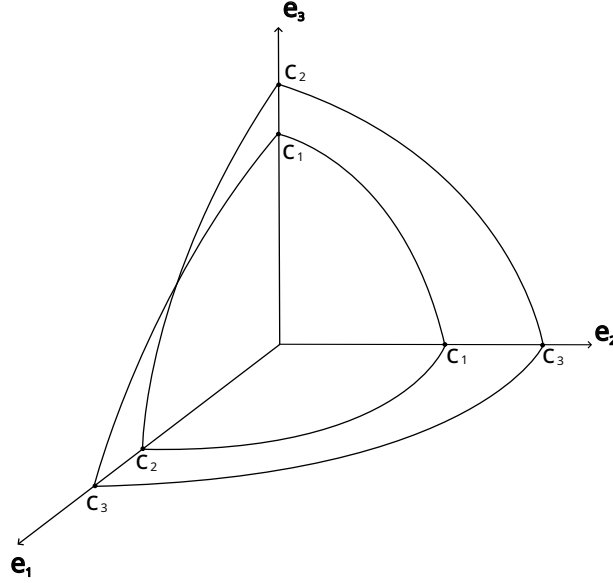


Figure 3.3: Wave surface of Fresnel with two sheets

Where we introduced ρ_0 , the density for solid ice (917 kg/m³). For the development of the simulation software equation 3.9 was taken and after assuming Schytt's equation (equation 3.11) to hold we find that the index of refraction abides by

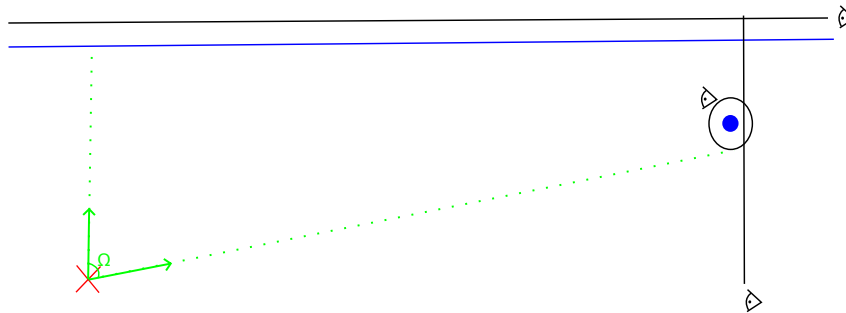
$$n(z) = n_{ice} - \Delta n e^{z/z_0} \quad (3.12)$$

with n_{ice} the refractive index of solid ice and $\Delta n = n_{ice} - n_s$ with n_s the index of refraction of snow. This exponential dependency of the index of refraction on depth is called the *single exponential model*.

This single exponential model has a huge advantage as it's analytically solvable, meaning that we can know which direction we'll have to shoot our ray in (as mentioned previously) after the location of the neutrino interaction and the detector are specified. The ray tracing algorithm developed using this exponential index is called the *analytic ray tracer*.

The discrepancy between the single exponential model and the actual data for the density implies that the analytic ray tracer will make the wrong predictions. This is why the development of a different ray tracer was needed which will be able to handle more complex ice models. One such ray tracer will be explained in section 3.4 but this ray tracer has its shortcomings. That's why the development of a new ray tracer was needed which is the partial work of this thesis and we'll get to that ray tracer in chapter 4.

Lastly there is an effect which might become important in the future: birefringence. Up until now we have implicitly assumed that ice is isotropic meaning that both its permittivity ε and its permeability μ are scalars but these could very well be tensorial in nature for radio waves in ice. In general, after calculating this tensorial nature through you'd find that in every direction two different indices of refraction can be found implying two different types of waves each propagating with a different speed as illustrated in figure 3.3. Which of the two speeds in a certain direction is then dependent on the polarization of the wave, which in our case thus depends on the Askaryan effect (see section 2.2). The optical property coming from the anisotropic nature of the material is what's called *birefringence*. Birefringence has been researched for implementation in the simulation software NuRadioMC used in the RNO-G group, e.g in [49].



3.3 Shortcomings of the exponential ice model

3.4 Iterative ray tracer

Now that the setup has been established we'll just iteratively shoot rays from the neutrino interaction point starting at an angle $\Delta\theta_1$ then at an angle $2\Delta\theta_1, 3\Delta\theta_1, \dots$. Until we have reached Ω . This process is illustrated on the left side of figure 3.5. After we have gone over all the different launch angles we'll have some solutions (marked in green) and some that don't end up on the detector (marked in red) we can now make the observer sphere's radius smaller ($r_2 < r_1$) and the step size of the angle smaller ($\Delta\theta_2 < \Delta\theta_1$). And again iteratively find the rays which end up on the sphere, only this time looking within the angles of the solutions of the previous step. We can keep on making the sphere and step size smaller in iterative steps until we've reached the precision we want. We then take, for each bunch of solutions within an angle interval, the most normal to the detector as the final solutions.

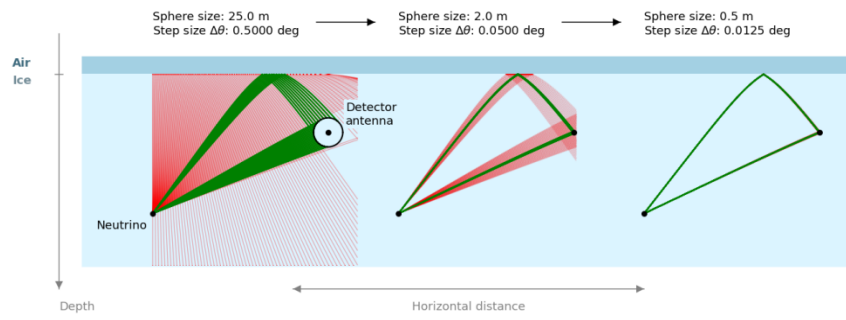


Figure 3.5: Illustration of the steps of the iterative ray tracer

HYBRID RAY TRACER

An algorithm was developed to work out the path the rays would trace out in more complex ice models called the *iterative ray tracer* [50], which was discussed in section 3.4. The way this algorithm works is however a sub-optimal solution in python as an optimization library will generally work faster and more accurate, work had been done on trying to implement such an algorithm deemed the "minimizer" but this attempt failed. As we saw this work the idea came to mind to combine the iterative ray tracer and the code using the optimization libraries. This way we built the algorithm which will be discussed in this chapter: The hybrid ray tracer, in the source code called the "hybrid minimizer" which can be found [here](#) under the radiopropa/hybrid_minimizer branch.

It succeeds in more rapidly finding the path from the event to the detector, is more accurate and also arrives closer to the detector as the final result is not limited by the final drawn sphere size but by a given tolerance making it useful for simulations in which high time and space precision is needed like plane wave reconstruction, which we'll do in the next chapter.

4.1 How the hybrid ray tracer works

The hybrid minimizer can be seen as an extension of the iterative ray tracer as it starts out the same way: Say our source of radiation is at position \mathbf{X}_1 and our detector is located at position \mathbf{X}_2 , we start by defining the vector $\mathbf{v} = \mathbf{X}_2 - \mathbf{X}_1$, then we clone it as a new vector \mathbf{u} and set it's z coordinate to 0, making it a normal vector of a plane parallel to the z direction in the lateral direction of the detector. We now want to constrain the search to where solutions are actually possible. Looking at figure 3.1 we see that no solutions below the direct path are possible as there would need to be upwards reflection, so we convert our vector \mathbf{v} representing the path from the source to the detector to spherical coordinates, giving us a polar angle (zenith angle) "theta-direct". With this we know that from the source the ray should propagate with an initial zenith angle lying within the angle interval 0° to $\text{theta-direct}^\circ := \Omega$ ($\theta \in]0, \Omega]$).

Next we need to define our "observers", if you shoot a ray with the radiopropa module from a certain point at a certain angle the ray path will get simulated until it interacts with this "observer". Ideally we would like to a priori know where to shoot our ray and have the detector be an infinitesimally small observer in our simulation, but as we'll be working with general ice

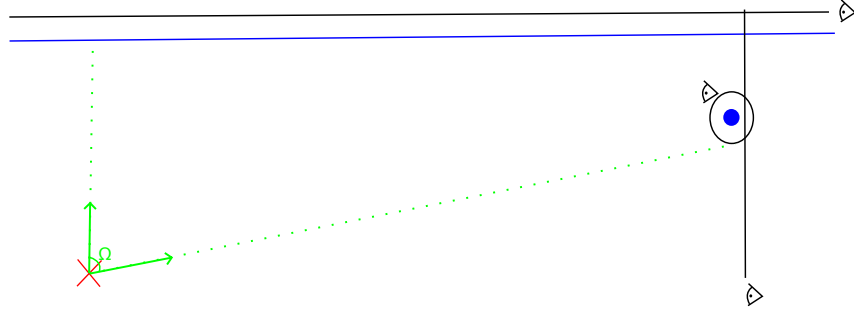


Figure 4.1: Illustration of the workings of the hybrid algorithm

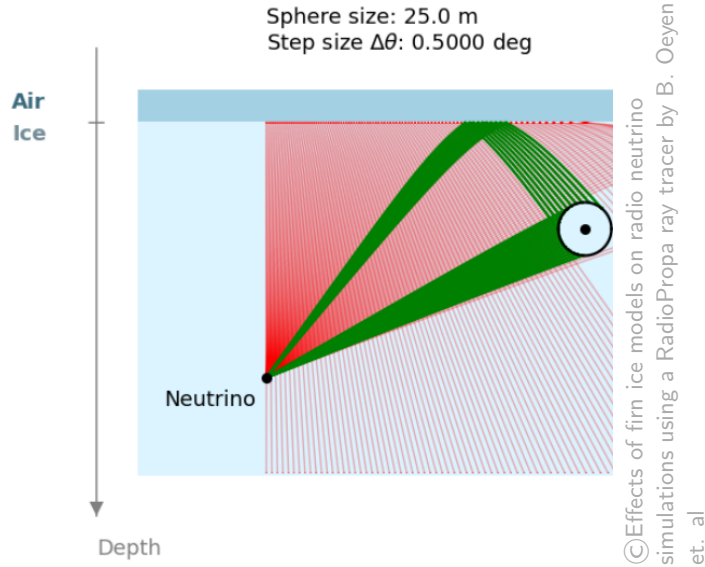


Figure 4.2: Iterative searches to find where the ray tracer ends up at the sphere, shown in green

models this can't be done.

The algorithm of finding the possible paths is then as follows: We define a spherical observer at the location of the detector, with a radius of fair size¹. We place an observer plane directly behind the detector with normal vector \mathbf{u} (as no rays can propagate back after passing the detector) and an observer above the surface (as no rays could make it back after escaping the ice) our full setup is then what's illustrated in figure 4.1

Here the red cross is the radio source, the blue horizontal line is the ice-air boundary surface, the blue dot to the right is the detector and the green Ω indicates the range over which solutions to the problem are possible.

We start off by just iteratively guessing: given a certain angle step size $\Delta\theta$ shoot rays at the angles $\{0, \Delta\theta, 2\Delta\theta, \dots, \Omega\}$ And see which ones get detected at the sphere around the detector, this process is illustrated in figure 4.2.

If 2 distinct launch regions are found, say in the regions $[\theta_1, \theta_2]$ and $[\theta_3, \theta_4]$ the rays end up on the sphere (drawn in green), then the so called *minimization* procedure will start. Using scipy's module `optimize.minimize` the optimal solution will be found by using the Nelder-Mead method [51]. First we get rid of the spherical observer and place the vertical observer at the detector, now to be able to use the minimize module we'll need a function to minimize, for

¹We'll get back to how this "fair size" gets chosen

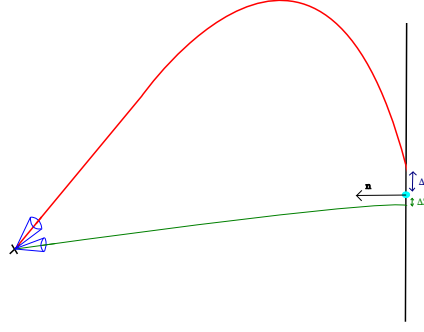


Figure 4.3: The scipy algorithm shoots rays in a direction within the blue cone angle intervals and minimizes the Δz that gets returned

this reason we first define the function *delta_z* as, given a certain launch angle, propagating the ray onto the vertical observer and returning the distance from the point where it lands on the plane to the detector, as illustrated on figure 4.3 (i.e it returns the value Δz). The function we'll minimize is then *delta_z_squared* which just squares the value which *delta_z* returns as we want to do away with negative values (so we can minimize to $\Delta z = 0$). We use the previously found angle boundaries as the boundaries for this minimization algorithm, meaning that if the 2 zenith angle intervals $[\theta_1, \theta_2]$ and $[\theta_3, \theta_4]$ were found in the first step of the algorithm it will first minimize Δz^2 within the first angle interval and find it's solution and then within the second angle interval. With this our algorithm is done, it does have a fail-safe as well in case that the first step, finding the launch regions, doesn't find the 2 launch regions. Namely it reverts back to being the iterative ray tracer.

4.2 Performance Optimization

We wish to optimize this algorithm to make it as fast as possible. To consistently test the algorithm after every particular change in a parameter we'll be randomly generating vertex interaction positions, keeping the detector at the fixed (0,-100) value. To this end the numpy random module was used to generate random coordinates, the considered square (as there is only a z component to the ice model, the 3D problem has cylindrical symmetry and thus essentially only a 2D problem) is $x:0.1\text{km}, 4\text{km}$ and $z:-0.1\text{km}, -3\text{km}$ ². Every simulated point shown in the following subsections consists of at least 500 random initial positions. As the speed of the algorithm is computer dependent the algorithm's speed is always plotted relative to the iterative ray tracer's speed, simulated with the same coordinates and under equal computer load.

Now we don't want to just achieve higher speed in our algorithm, we also want to at least have the same accuracy as the iterative ray tracer, if not even better. To this end we need to check with an "exact solution". There is only one candidate that fits this role: *the analytic ray tracer*. The plan is thus to use the exponential ice model as a testing ground for the hybrid ray tracer and solving each vertex-detector ray tracing problem with both the iterative, analytic and hybrid ray tracer. After having solved for the **propagation time** (meaning the time it takes the ray to propagate from the source to the detector) and the **arrival zenith angle** (the zenith angle the ray makes at the detector) for each of the algorithms we can infer the accuracy of a particular algorithm by how much it differs from the solution found through the analytic ray tracer.

²This start at 100m depth was to get around issues concerning events that won't even trigger in a full simulation

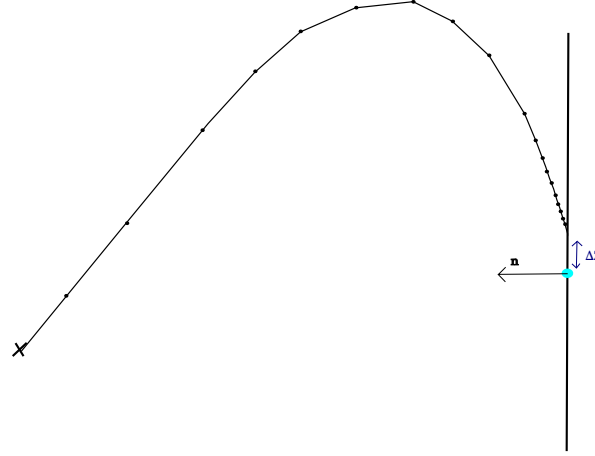


Figure 4.4: the steps taken are illustrated with the dots, the spacing reduces close to the detector. changing the normal vector changes the spacing

4.2.1 Length of the normal vector

Whilst figuring out what was wrong with the initial *minimizer* we stumbled on the fact that radiopropa has a little weird quirk. As visually explained in figure 4.4, the size of the normal vector seems to influence how big radiopropa's ray tracer's step size is taken close to the detector. This thus influences the accuracy and total computational time taken. The results of varying the length of this normal vector, comparing the accuracy (in timing and arrival zenith) with the analytic ray tracer and the computational time with the iterative ray tracer, are shown in figures 4.5 and 4.6. Looking at these figures we can make, what would normally be rather obvious but is interesting nonetheless, a first optimization conclusion: take the normal vector length to be 1 unit in radiopropa. We can conclude this as the calculation speed seems to be minimal there (after zooming in on the graph) and the accuracy dropping rapidly after 1 meter.

4.2.2 ztol

We'll now change the *tolerance*, with this we mean when the minimization algorithm returns a Δz smaller than a certain threshold "ztol" the ray will be accepted as the solution. The results from analogous comparisons as previously discussed are shown in figures 4.7 and 4.8. There seems to be a minimum around 0.05m, looking at the accuracy for this tolerance it seems sufficient to be used. We can thus infer the second optimization conclusion: take ztol to be 0.05 m.

4.2.3 Sphere Size & Step Size

The initial rays are sent out in steps of a certain angle and with a sphere around the detector of a certain size. Varying the parameters of this first step of the algorithm (e.g the step size and sphere size) might thus have an effect on both the accuracy and the computational time. As this initial search for launch angle regions is also the slowest step in the hybrid ray tracer (takes $\approx 57\%$ of the total computation time) it's also the most important step to optimize. The optimization procedure is as follows: change the sphere size and loop over various step sizes, recording the speed. Note that, as we have to vary 2 parameters, we can't really look at accuracy

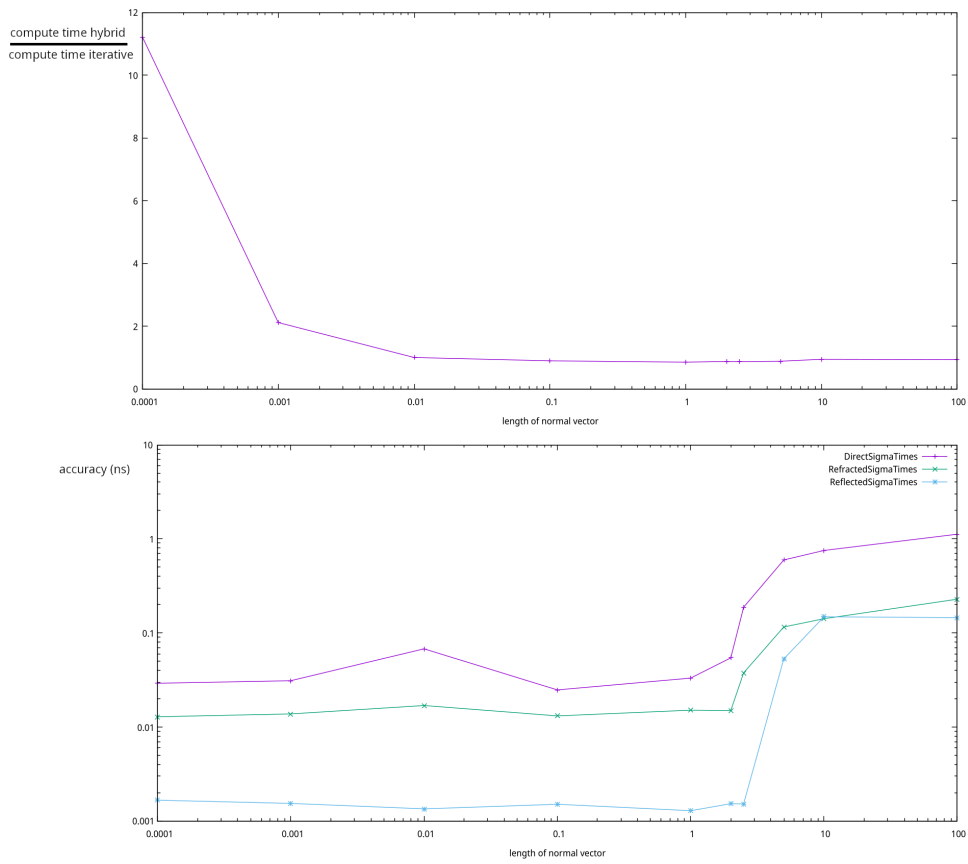


Figure 4.5: The speed lowers with larger normal vector length but the accuracy on timing gets worse after a length of 1

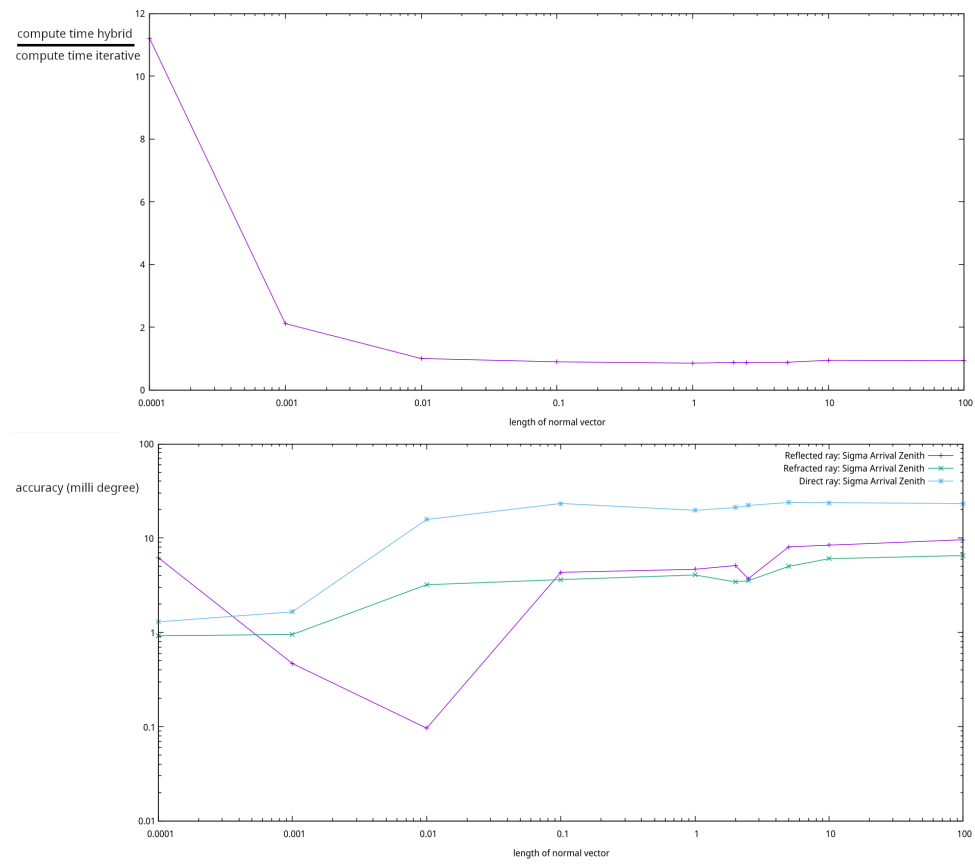


Figure 4.6: The speed lowers with larger normal vector length but accuracy stays roughly the same after 0.1

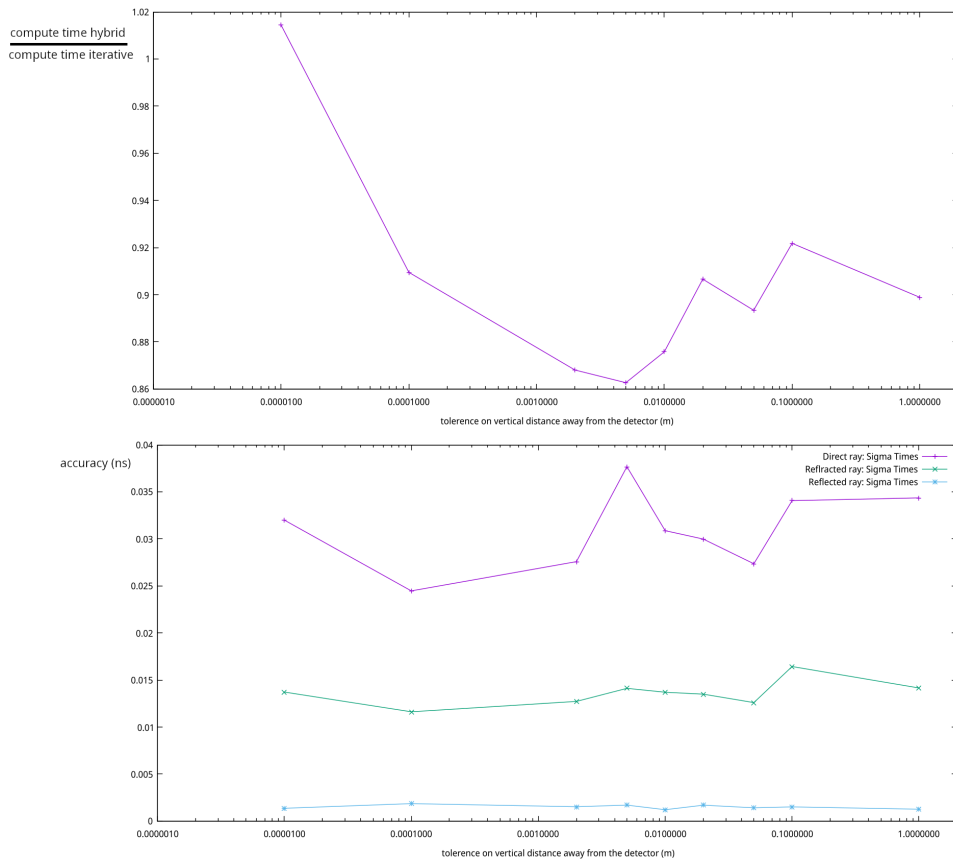


Figure 4.7: the solution seems to reach a minimal time at a tolerance of 5cm whilst the accuracy on timing stays roughly the same

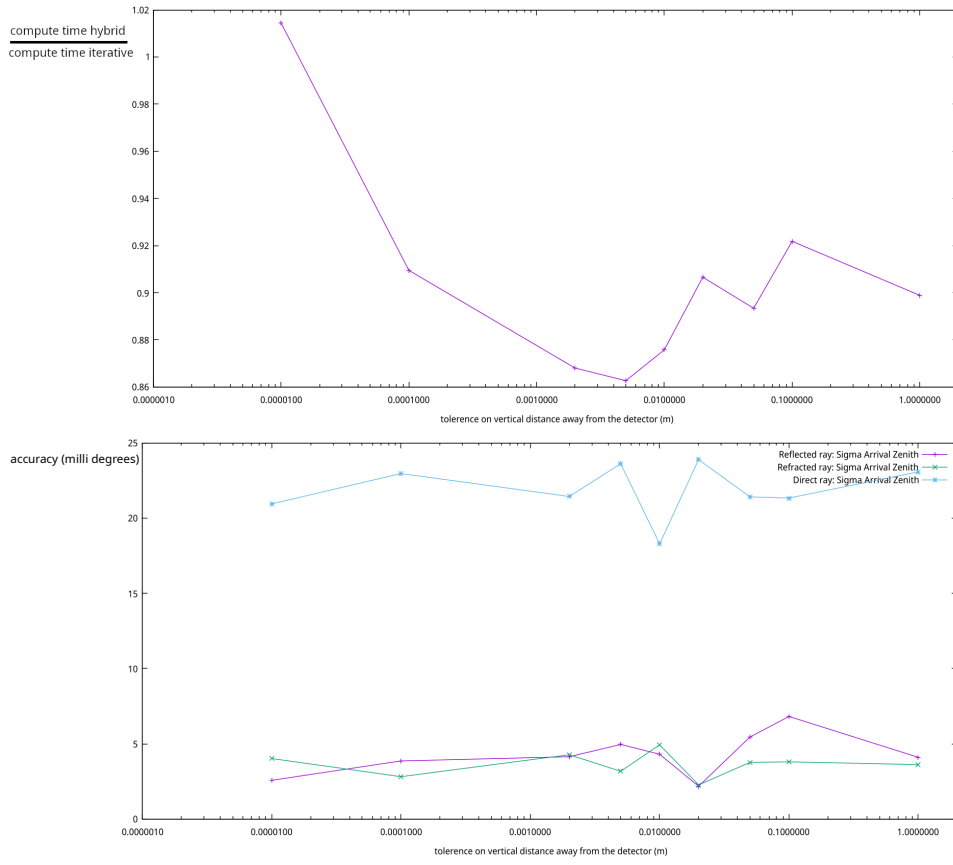


Figure 4.8: the solution seems to reach a minimal time at a tolerance of 5cm whilst the accuracy on the angle stays roughly the same

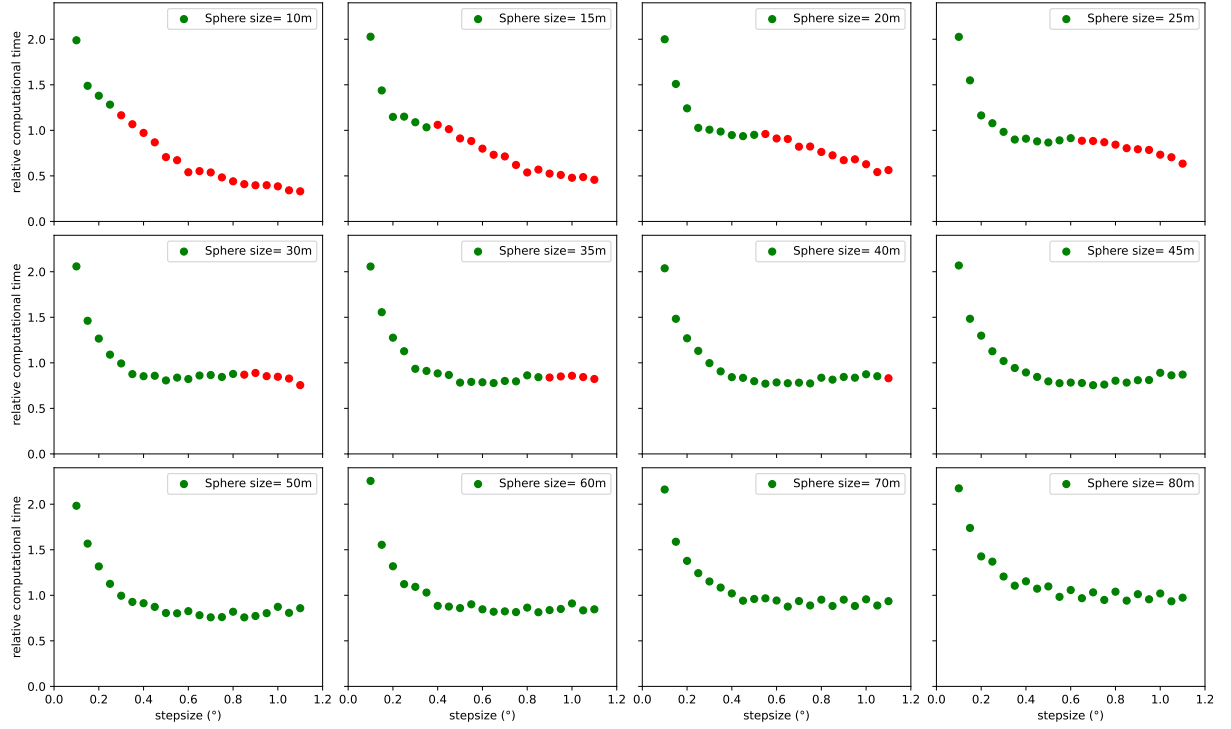


Figure 4.9: The data in green is acceptable, at high sphere size the geometric effects start to play a role and staggering is observed

here. This isn't needed however as we'll see that after finding the optimal solution the accuracy is still sufficient, apart from one part where it is needed: **if insufficient solutions are found**, as we wish this algorithm to be better the iterative ray tracer, it'll need to at least find as many solutions as the iterative ray tracer does. If, for a particular random interaction vertex location, less solutions are found by the hybrid ray tracer than for the iterative ray tracer, this parameter choice will be thrown away (and colored differently). The results are shown in figure 4.9, the points colored red are unusable as previously discussed.

The lower on the graph the points lie, the better. If we combine all the green points into a single plot we get what is shown on figure 4.10, zooming in onto the lowest point, we see that an optimal sphere size seems to be at 45m accompanied by a step size of 0.7° , this is in contrast to the iterative ray tracer where a sphere size of 25m and stepsize of 0.5° is used. Note that changing these values for the iterative ray tracer doesn't change its speed nor accuracy.

The programs used in making these plots can be found [here](#) under the folder "testhybrid".

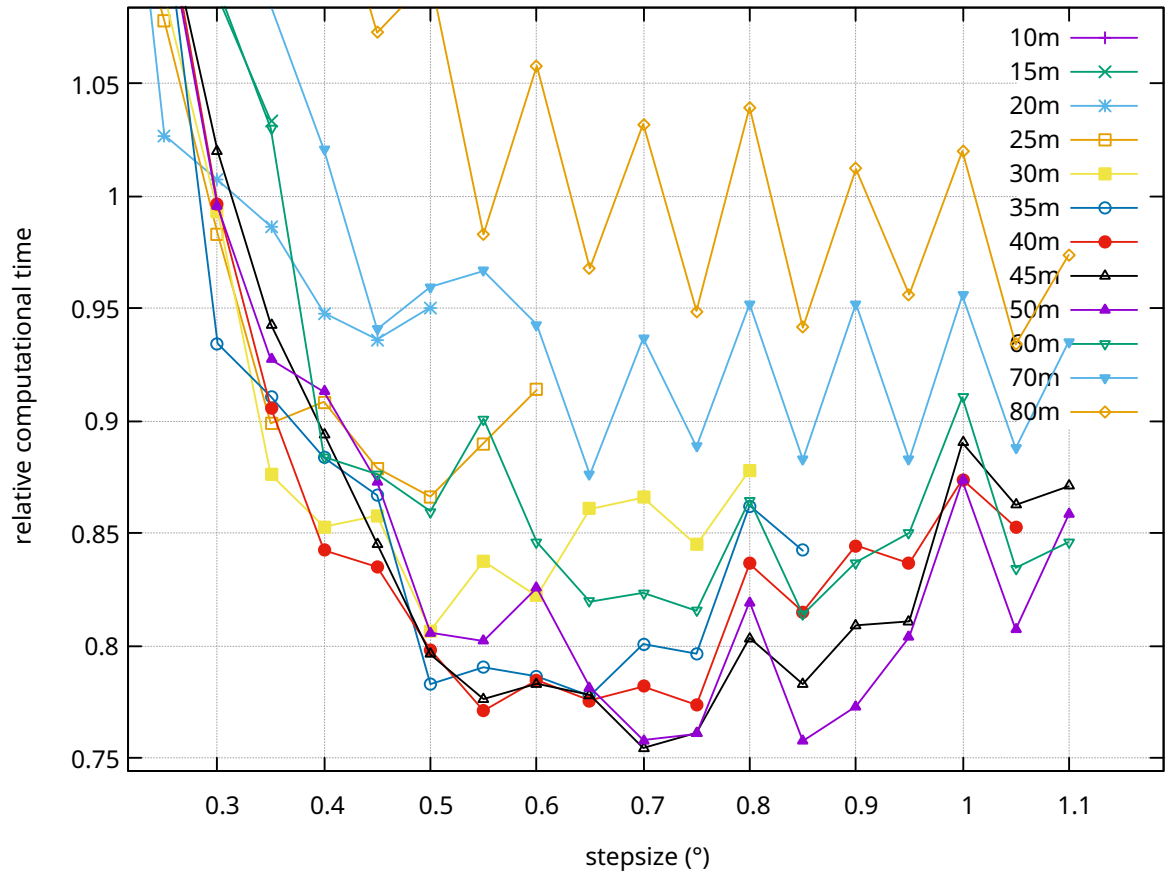


Figure 4.10: Green values in variation in sphere and angle step size, the lower the better. Max speed (lowest point on the figure) at 0.7° as step size and 45m sphere size

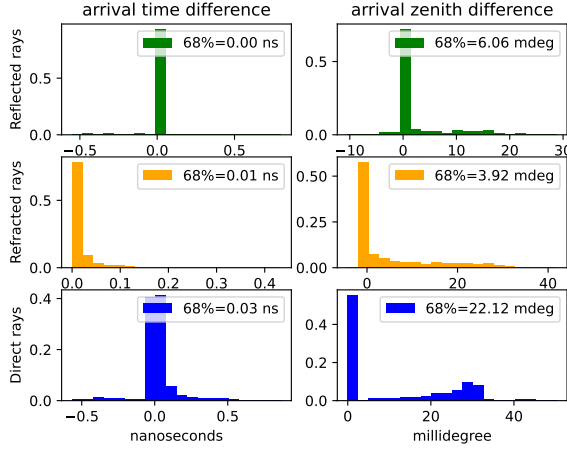


Figure 4.11: Hybrid

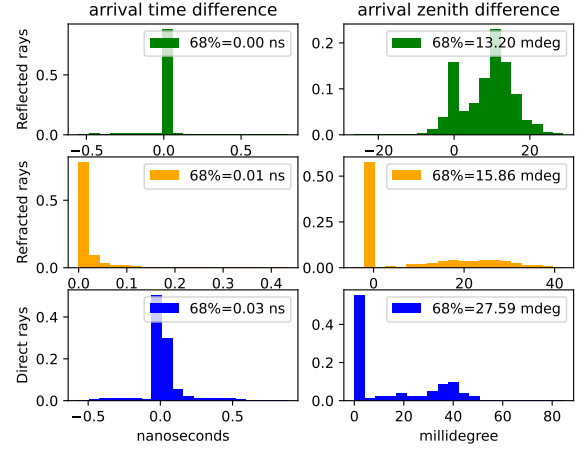


Figure 4.12: Iterative

4.2.4 Conclusion of optimization

How does the hybrid ray tracer perform relative to the iterative ray tracer if we use the previously optimized variables? After doing a simulation of 1000 random source locations (double the previous amount) with the iterative, analytic and hybrid ray tracer and comparing both the iterative to the analytic and the hybrid to the analytic we get what's shown in figures 4.11 and 4.12. Where we can clearly see that the hybrid ray tracer is more accurate, now during this simulation we also recorded the computational speed, the fractional speeds relative to the analytic ray tracer are presented below:

- iterative: 5.93×10^{-5} computations/analytic computation
- hybrid: 7.97×10^{-5} computations/analytic computation

The hybrid ray tracer is thus 33.7% faster than the iterative ray tracer. The speed difference with the analytic ray tracer might seem quite overwhelming but this can get mitigated in the future if part of the hybrid ray tracer gets re-written in a compiled language (like c++) just like the analytic ray tracer.

WEATHER BALLOON

In this chapter we'll infer optical information about the ice the detectors reside in using radio signals coming from a weather balloon flying over the stations. Every day in the summer, 2 times a day, a weather balloon gets launched from base camp at Summit in Greenland. This weather balloon has an antenna strapped to it constantly emitting a sinusoidal signal of 0.403GHz.

We can use this signal to find the index of refraction locally at the phased array. We'll go about this by first finding the difference in timing between channels by fitting the balloon's sinusoidal signal to the data, and then doing a plane wave reconstruction, minimizing the angle the reconstruction makes with the balloon, with that finding the local index of refraction. This procedure will be explained more in depth over the following sections.

Prior to the measurements we'll need to be able to predict how accurate our findings will be, for this we'll need to run a simulation with the hybrid ray tracer. There is one change that needs to happen first to our algorithm for us to be able to simulate this: The air observer has to be removed as to make a ray tracing possible from within the air into the ice and onto the detector. The modified version of the hybrid ray tracer can be found [here](#) under the branch radiopropa/BaLLoon.

5.1 Plane Wave Reconstruction

We want to do a plane wave reconstruction of the balloon's position as this will make us able to infer the index of refraction between chosen channels. Example paths the weather balloon produce that end up in the deep channels is shown in figure 5.1, here the balloon emits a signal which propagates straight in the air and then refracts in the ice. Locally in the ice we can assume the wave to come in as a plane wave.

The arriving plane wave is shown as parallel lines in blue on figure 5.2. The plane wave reconstruction method can be understood by taking a closer look at this figure, the radio waves coming from the weather balloon make a certain angle θ with the detectors. The top detector (top box) detects the wave at a certain time t_1 , the bottom detector detects it at a time t_2 . After deciphering the data RNO-G recorded we'd thus see that these two detectors got a signal $\Delta t = t_1 - t_2$ seconds apart from each other. Now ideally this observed time is equal to the time

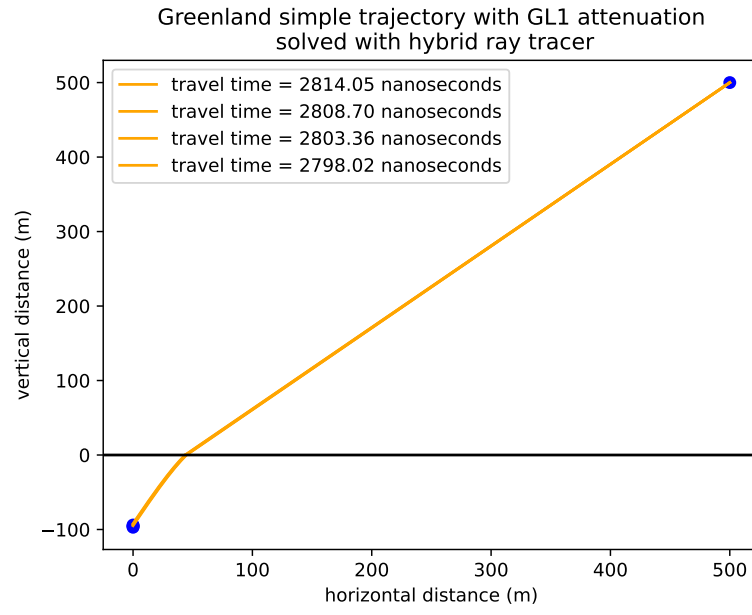


Figure 5.1: Example trajectory of rays coming from a weather balloon (blue dot top right) and going through the ice to the various detectors (blue dots bottom left)

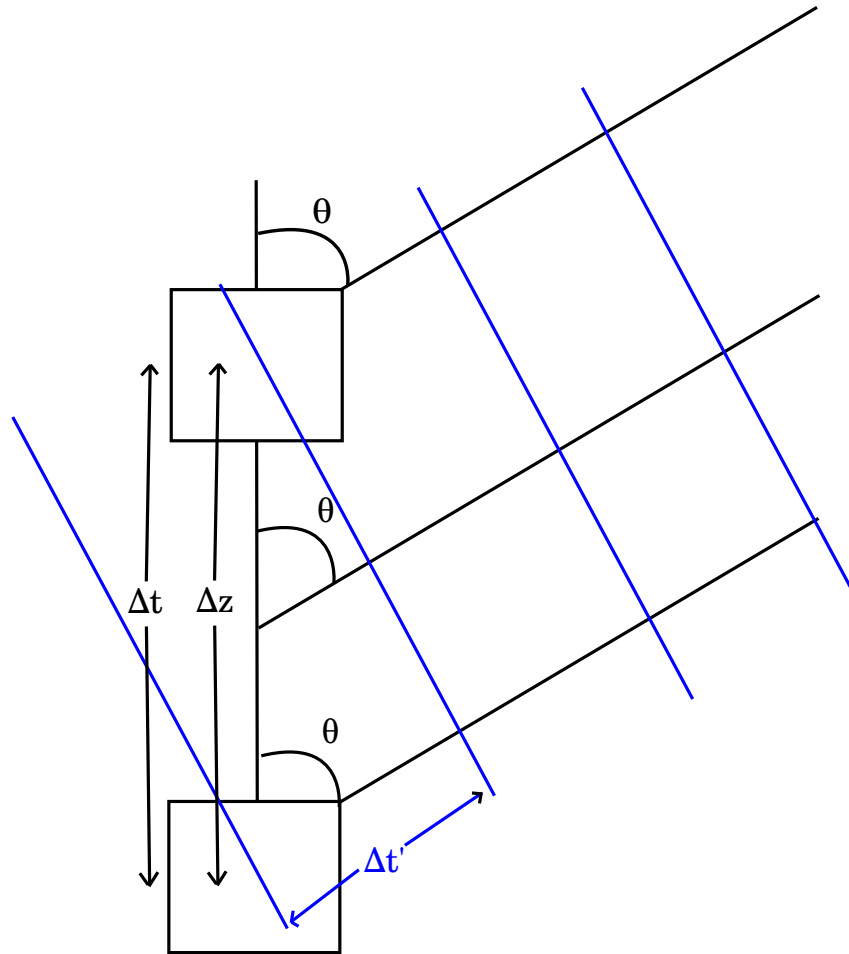


Figure 5.2: Illustration of Plane waves

it would take a plane wave to propagate that distance ($\Delta t'$) which we can calculate from the geometry of the problem and dimensional analysis:

$$\Delta t' = \frac{m}{(m/s)} = (s/m) * m = v^{-1} * m = v^{-1} \cos \theta \Delta z \quad (5.1)$$

With $v = c/n$ the local speed of light, n the index of refraction at the depth in between the considered channels and Δz the distance between the channels. Thus if we know the angle θ , the time $\Delta t'$ and the distance between the channels Δz we could infer the index of refraction at a certain depth as can be seen by reforming equation 5.1:

$$n = \frac{\Delta t' c}{\Delta z \cos \theta} \quad (5.2)$$

We can actually roughly guess the angle, as for a balloon flying close to the detector this incoming angle will be roughly the same as the observed angle. At the actual index of refraction we expect the following function to show a minimum (go to zero) at that angle:

$$\eta(\theta, n) := (\Delta t - \Delta t') = \left(\Delta t - n \frac{\cos \theta \Delta z}{c} \right) \quad (5.3)$$

If we want to determine the index of refraction, we need to minimize equation 5.3 with $\theta = \theta_b$:

$$\eta(n) = \left(\Delta t - n \frac{\cos \theta_b \Delta z}{c} \right) \quad (5.4)$$

If we want to use more than 2 detectors at once however (which we'll do for the phased array), we'll need to specify various functions to minimize. E.g if we have four detectors labeled 0 to 3 we'll have to construct functions between detectors 0&1, 0&2, 0&3, 1&2, 1&3 and 2&3. The further apart the detectors lie the larger the function values and thus the more they will weigh in the sum. This importance to further spaced channels is what we want as these will yield a more accurate result.

5.1.1 simple plane wave reconstruction

To take into account all the different channels we take the sum of the various eta functions (as defined in equation 5.4) and thus minimize the following function with respect the the index:

$$f(n) := \sum_{i=\text{channel pairs}} \eta_i(n) = \sum_{i=\text{channel pairs}} \left(\Delta t_i - \frac{n \cos \theta_b \Delta z_i}{c} \right) \equiv \sum_{i < j} \left(\Delta t_{ij} - \frac{n \cos \theta_b \Delta z_{ij}}{c} \right) \quad (5.5)$$

where Δt_{ij} denotes the observed time difference between channels i and j , similarly Δz_{ij} denotes the distance between channels i and j . If this function f gets minimized, the n leading up to this minimization will be the answer we are seeking: the index of refraction inbetween the detectors. We now want to find the error on the index we fitted this way. To find the error on our result we need an expression for the index, let's solve for n :

$$f(n) = \sum_{i < j} \left(\Delta t_{ij} - \frac{n \cos \theta_b \Delta z_{ij}}{c} \right) \quad (5.6)$$

$$\sum_{i < j} \frac{n \cos \theta_b \Delta z_{ij}}{c} = \sum_{i < j} \Delta t_{ij} - f(n) \quad (5.7)$$

$$n = \frac{c}{\cos \theta_b} \left(\frac{\sum_{i < j} \Delta t_{ij}}{\sum_{i < j} \Delta z_{ij}} - \frac{f(n)}{\sum_{i < j} \Delta z_{ij}} \right) \quad (5.8)$$

Let's assume an error on the difference in propagation time between channel i and j (Δ_{ij}) of δt_{ij} , which we'll find out later. For the positional accuracy we'll assume to know the detector location to within 1cm^1 , this will imply an accuracy on Δz_{ij} of 2cm .

Let's now compute the error on our predicted index:

$$\delta n = \frac{c}{\cos \theta_b} \delta \left(\frac{\sum_{i<j} \Delta t_{ij}}{\sum_{i<j} \Delta z_{ij}} - \frac{f(n)}{\sum_{i<j} \Delta z_{ij}} \right) \quad (5.9)$$

$$\delta n = \frac{c}{\cos \theta_b} \delta \left(\frac{\sum_{i<j} \Delta t_{ij}}{\sum_{i<j} \Delta z_{ij}} \right) + f(n) \frac{c}{\cos \theta_b} \delta \left(\frac{1}{\sum_{i<j} \Delta z_{ij}} \right) \quad (5.10)$$

$$(5.11)$$

Note here the function δ denotes the absolute error, let's define the function RE to be the relative error and look at the terms individually:

$$\delta \left(\frac{\sum_{i<j} \Delta t_{ij}}{\sum_{i<j} \Delta z_{ij}} \right) = \left(\frac{\sum_{i<j} \Delta t_{ij}}{\sum_{i<j} \Delta z_{ij}} \right) \times \left(RE \left(\sum_{i<j} \Delta t_{ij} \right) + RE \left(\sum_{i<j} \Delta z_{ij} \right) \right) \quad (5.12)$$

$$\delta \left(\frac{\sum_{i<j} \Delta t_{ij}}{\sum_{i<j} \Delta z_{ij}} \right) = \left(\frac{\sum_{i<j} \Delta t_{ij}}{\sum_{i<j} \Delta z_{ij}} \right) \times \left(\frac{\sum_{i<j} \delta t_{ij}}{\sum_{i<j} \Delta t_{ij}} + \frac{\sum_{i<j} \delta z_{ij}}{\sum_{i<j} \Delta z_{ij}} \right) \quad (5.13)$$

$$\delta \left(\frac{\sum_{i<j} \Delta t_{ij}}{\sum_{i<j} \Delta z_{ij}} \right) \approx \left(\frac{\sum_{i<j} \Delta t_{ij}}{\sum_{i<j} \Delta z_{ij}} \right) \times \left(\frac{\sum_{i<j} \delta t_{ij}}{\sum_{i<j} \Delta t_{ij}} + \frac{\sum_{i<j} 0.02m}{\sum_{i<j} \Delta z_{ij}} \right) \triangleq E_1 \quad (5.14)$$

$$(5.15)$$

And now the second term:

$$\delta \left(\frac{1}{\sum_{i<j} \Delta z_{ij}} \right) = \left(\frac{1}{\sum_{i<j} \Delta z_{ij}} \right) \times RE \left(\sum_{i<j} \Delta z_{ij} \right) \quad (5.16)$$

$$\delta \left(\frac{1}{\sum_{i<j} \Delta z_{ij}} \right) = \left(\frac{1}{\sum_{i<j} \Delta z_{ij}} \right) \times \frac{\delta \left(\sum_{i<j} \Delta z_{ij} \right)}{\sum_{i<j} \Delta z_{ij}} \quad (5.17)$$

$$\delta \left(\frac{1}{\sum_{i<j} \Delta z_{ij}} \right) = \frac{\sum_{i<j} \delta z_{ij}}{\left(\sum_{i<j} \Delta z_{ij} \right)^2} \quad (5.18)$$

$$\delta \left(\frac{1}{\sum_{i<j} \Delta z_{ij}} \right) \approx \frac{\sum_{i<j} 0.02m}{\left(\sum_{i<j} \Delta z_{ij} \right)^2} \triangleq E_2 \quad (5.19)$$

$$(5.20)$$

So, finally:

$$\delta n \approx \frac{c}{\cos \theta_b} (E_1 + f(n)E_2) \quad (5.21)$$

5.1.2 plane wave reconstruction using snell's law

This was one way of fitting the index of refraction, another procedure that we could do is by implementing breaking of the plane wave at the surface.

¹this is a reasonable estimate as this is the accuracy of the reported channel positions

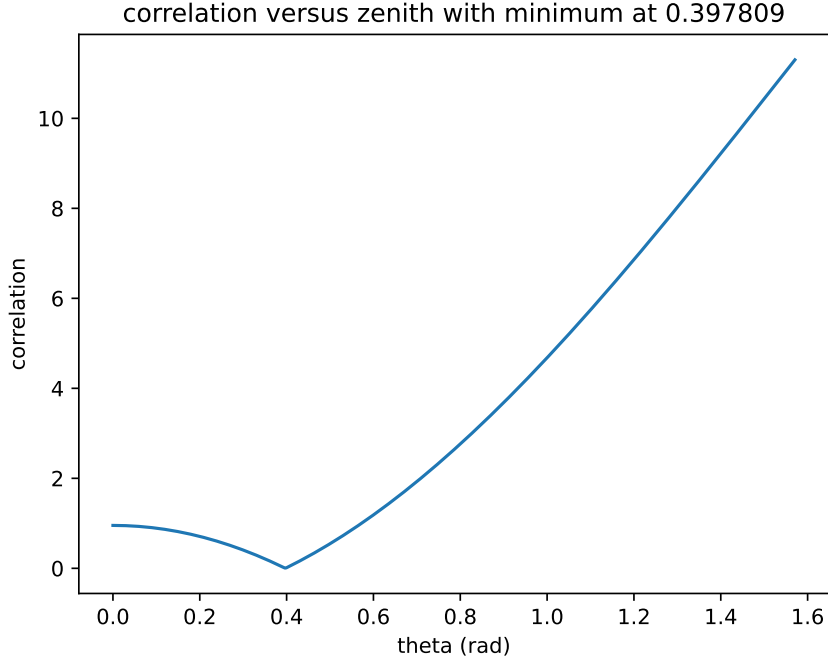


Figure 5.3: Example sum of the normed correlation functions

We thus assume the reconstructed plane wave to behave like an actual wave and, encountering the ice-air boundary, refracting according to snell's law. This is useful for when the angle with the balloon is quite big as is illustrated in figure 5.4, here you can clearly see that, even though the plane wave locally matches the incoming signal, it ends up really far away from the balloon. The reconstructed plane wave follows the wave path closely until the air-ice boundary where the wave path got refracted, we thus try doing the same thing by making the plane wave refract as well.

To find the index of refraction this way we can't minimize by taking the incoming plane wave to have the same angle as the balloon, we'll need to look at the distance between the plane wave reconstructed ray (after also refracting at the surface) and the balloon, both at the height of the balloon. The full procedure then goes as follows: We first choose a certain index of refraction n , then we reconstruct the plane wave launch angle by minimizing the function

$$f(\theta) := \sum_{i=\text{channel pairs}} \left(\Delta t_i - \frac{n \cos \theta \Delta z_i}{c} \right) \equiv \sum_{i < j} \left(\Delta t_{ij} - \frac{n \cos \theta \Delta z_{ij}}{c} \right) \quad (5.22)$$

Such a function is illustrated in figure 5.3. For this figure the modified hybrid ray tracing algorithm was used to simulate what the difference in timing would be. As can be seen on the figure this function is minimal at a certain launch angle θ_1 , we can use this angle and the height of the middle of the concerned detectors to derive the path in the ice until it encounters the air-ice boundary. To know the path after this boundary we'll need the outgoing zenith angle at the surface θ_2 which can be calculated from Snell's law:

$$n_1 \sin \theta_1 = n_2 \sin \theta_2 \implies \theta_2 = \sin^{-1} \left(\frac{n_1}{n_2} \sin \theta_1 \right) \quad (5.23)$$

After doing this we have a linear function describing the path in air after it passed the ice-air boundary layer. If we evaluate this function at the height of the balloon we then get the distance

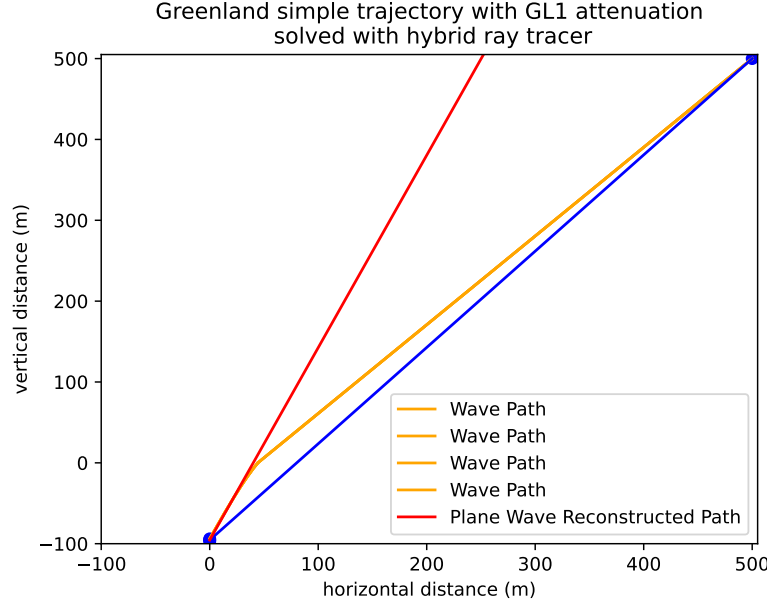


Figure 5.4: The balloon is too far away for a simple plane wave reconstruction, but using snells law at the surface might mitigate the problem.

the reconstructed ray is away from the balloon. To find the index of refraction n we record this distance and redo the procedure starting at the minimization of equation 5.22 for a different index of refraction. After iterating through indices this way we then have a list of corresponding distances to the balloon. The index corresponding to the minimum in these distances is then the final result.

5.2 Is the goal feasible?

5.2.1 Simple Plane Wave

In the example reconstruction illustrated in figure 5.4 the difference in angle between direct to balloon and plane wave reconstruction is quite big ($\approx 65\%$) but as the balloon gets closer to the detector this reduces significantly. As previously layed out, our goal is to find the local index of refraction n by using the plane wave reconstruction with the recorded timing and the positional data from the weather balloon.

Now let's ask ourselves the question, within which angles should the weather balloon fly for the data to be useful? The further the weather balloon is away (in the x direction) the bigger the zenith angle with the detector, the less accurate the plane wave reconstruction. So which angles are acceptable? Note that not only angle but also height will eventually play a role in the accuracy, the angle however gives a good starting point.

To determine the accuracy we vary the position of the weather balloon in the x direction (keeping the height constant at 500m), simulate the ray path to channels 0 to 3 and then fit n both via the simple plane wave reconstruction method layed out in section 5.1.1 and the one using snell's law layed out in section 5.1.2. We then compare the n 's we have fitted to the one we know from the model at that position. We quantify the discrepancy between the fitted and known index of

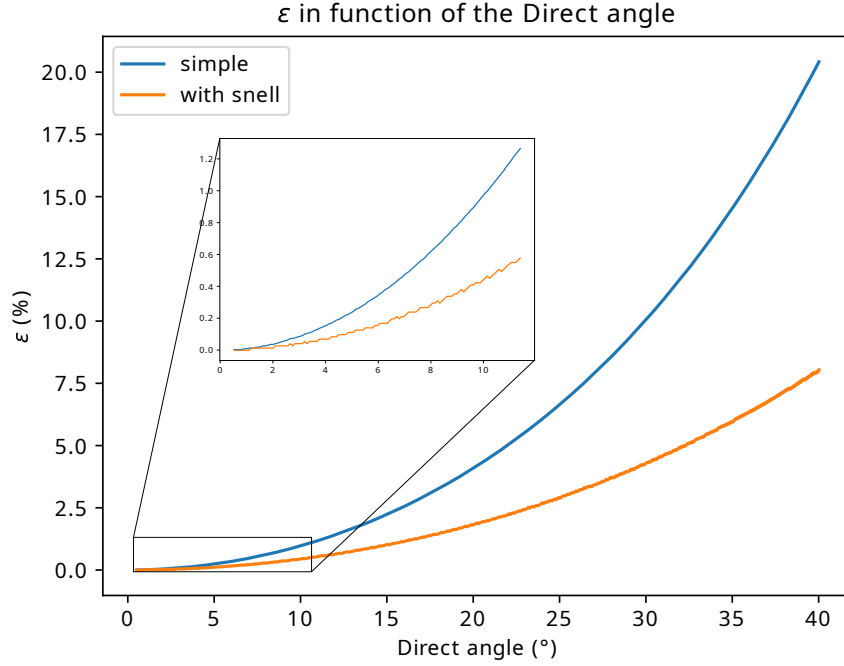


Figure 5.5: The accuracy of the plane wave reconstruction with the use of snell’s law at the surface is more accurate but the simple plane wave method’s accuracy is sufficient to make reliable predictions for angles less than 10°. For small angles the simple reconstruction is preferred as no ice parameters need to be assumed.

refraction via the *systematic error*:

$$\varepsilon (\%) = \frac{n_{\text{fit}} - n_{\text{exact}}}{n_{\text{exact}}} \quad (5.24)$$

Carrying this out² we get figure 5.5. Both the snell and simple plane wave method get exponentially less accurate as the balloon moves further away. If we wish the systematic error to be within 1% for the simple plane wave, the angle the balloon makes with the middle of channels 0 to 3 needs to be less than 10°.

Now can we actually find balloon passbys whom make an angle less than 10 degrees? To figure this out we looped over all the balloon positions recorded over the summer of 2022, more particularly 15/06/2022 - 30/09/2022³, and recorded the time intervals when they flew close enough. To illustrate such a trajectory, an example path of a balloon passing close enough to a detector is shown in figure 5.6. The data shown in appendices D and C respectively show < 10° and < 5° encounters.

5.2.2 Influence of the height on the systematic error

In the previous sections we’ve assumed the height of the weather balloon to be 500m, does changing this height influence the behavior of the systematic error ε in some way? The answer is, at first surprisingly, yes. As can be seen in figure 5.7 the systematic error can vary with height for the same angles. This has, as a consequence, that if we manage to get a hold on some

²The code for this can be found in `projects-mt/BaLLooN/simulations` as `plane_wave.py`

³The positional data of the weather balloons was obtained from the <ftp1.esrl.noaa.gov> website using the `rno-g-sonde` script of the official RNO-G github page.

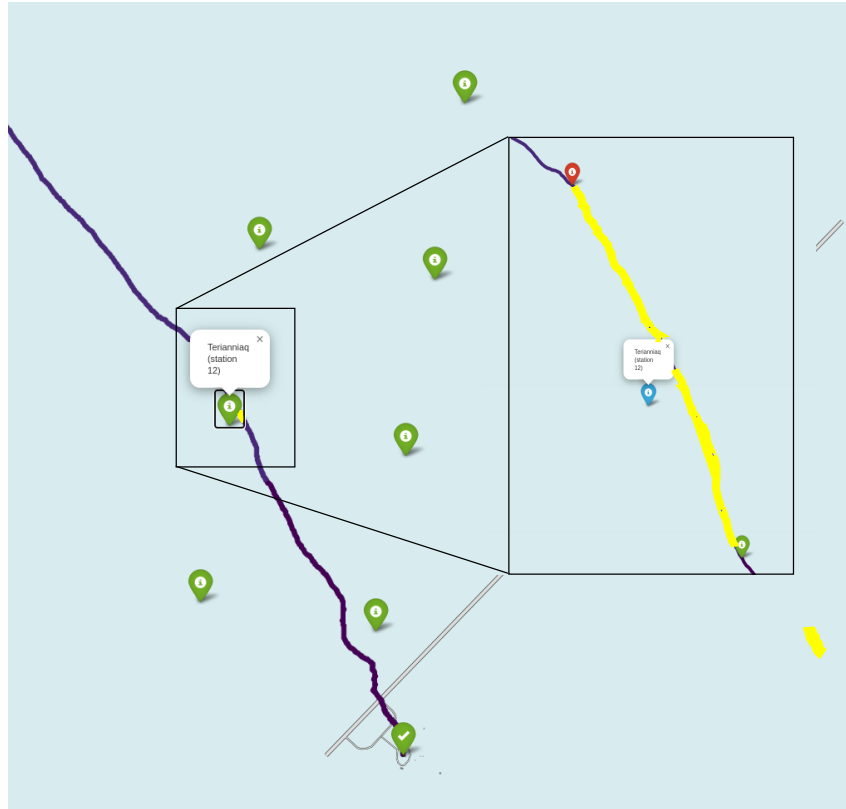


Figure 5.6: Path traced out by a weather balloon in purple released at 20/08/2022, in yellow you can see when it gets within 10° of detector 12.

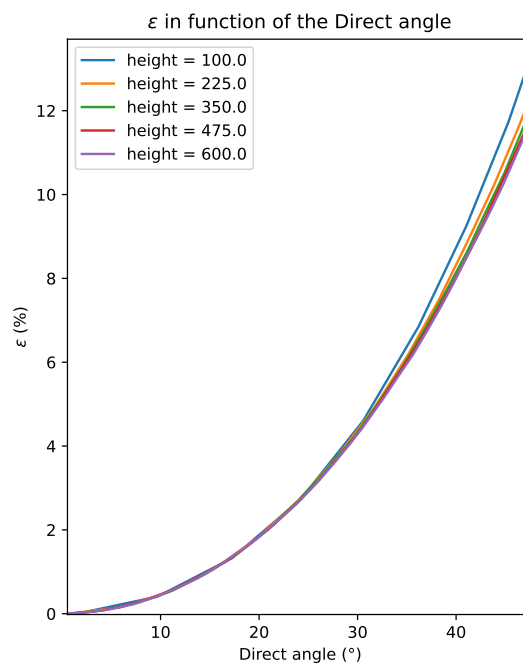


Figure 5.7: How varying the height influences ϵ over the same angles

usable data we'll still have to re-compute ϵ for every measurement we do.

5.3 Fitting the index: Phased array

Now that we know our goal to be feasible, let's analyze some data. As we'll start by just analyzing one event, let's take a reasonably good one for our analysis.

If we search in the DESY database ⁴ within the calculated time frames as listed in appendix C where the 403MHz signal coming from the balloon is detected in the deep channels, the events of the 24th of July stands out; at 23:21:53 the balloon gets quite close to detector 11 and shows a clear 403MHz signal at the phased array in channels 0,2 and 3, as shown for the channels 2 and 3 in figure 5.8.

Now to calculate the differences in timing for this received signal, the code we built for this is called FitN.py and stored at the repository [projects-mt](https://github.com/BaLloonN/RealData) under BaLloonN/RealData, let's go over the full code step by step:

Spatial data

The first part we'll need to concern ourselves with is determining the relative positions of everything. The balloon data file and the time when the event took place are given, from these two both the latitudinal and longitudinal position and the elevation of the balloon at the given time are determined, which we convert to ENU (x,y,z) coordinates as to be able to use them.

The locations of the various stations have also been determined and can be found on the official RNO-G github under "analysis-tools".

Now that we have both the position of our balloon and station, let's simplify the calculations by setting the detector as the origin i.e our new balloon position will be

$$\mathbf{r}_{bs} = \mathbf{r}_b - \mathbf{r}_s \quad (5.25)$$

With the subscript b denoting "balloon" and s "station". As we might want to plot this later, due to the cylindrical symmetry of the ice, we can rotate the coordinates to get rid of our y-axis. We can do this by defining the radius:

$$r := \sqrt{x_{bs}^2 + y_{bs}^2} \quad (5.26)$$

And redefining our relative position as

$$\mathbf{r} = \begin{bmatrix} r \\ 0 \\ z_{bs} \end{bmatrix} \quad (5.27)$$

We don't have the position of our individual channels yet, only of the station itself. The relative position of these can however also be obtained and as we chose our station to be the center of the coordinate system, these relative positions are absolute positions of the channels in our frame of reference. Using these it thus doesn't matter where the position of the station was defined.

⁴<https://rnog-monitor.zeuthen.desy.de/>

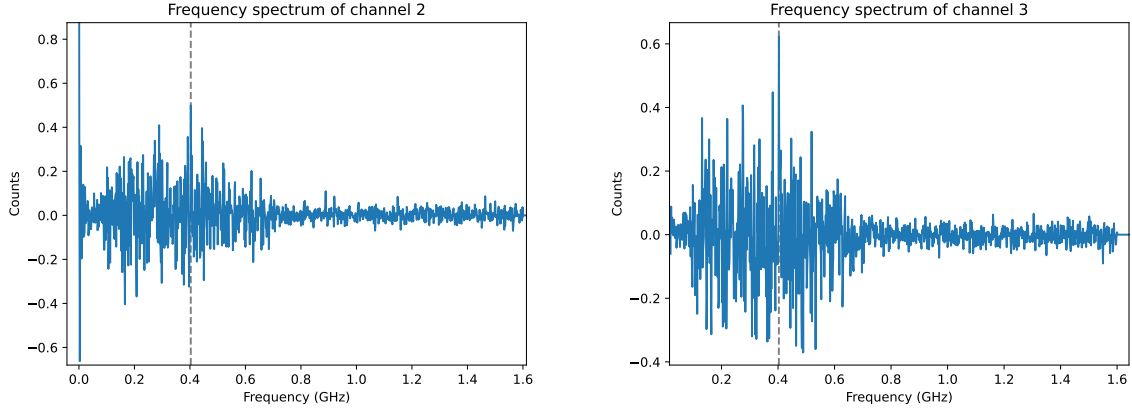


Figure 5.8: recorded frequencies on detector 11 at 2022/07/24 23:21:53, clear spikes at 0.403GHz are visible

Signal analysis and initial guesses

Now that we have our the position of the balloon and of the channels, let's analyze the data for the channels. The data for a particular channel from a recorded event (here event 12397 of run 1034) is stored in a channel object, from this object we can get the recorded voltages and times during this event. These recorded voltages can be Fourier transformed to get the recorded frequency spectrum. We know that the signal sent out by the weather balloon is a sine wave with a frequency of 403MHz; as the data is measured in nanoseconds the frequency is:

$$f = 403\text{MHz} = 403 \times 10^{-3} \frac{1}{\text{ns}} \quad (5.28)$$

The recorded spectrum of channels 2 and 3 is given in figure 5.8, for which we previously mentioned the spike at 0.403GHz. Now note that on this figure it's shown that there are signals with frequencies both below 0.15GHz and above 0.6GHz, these can be left out as the Vpol is defined to be most responsive only in the range 0.15GHz to 0.6GHz [52]. To filter out these frequencies we'll pass the signal trough a virtual butterworth bandpass filter.

Now that we have filtered our data we'd also like to increase the accuracy in timing, to this end we'll resample the signal. Resampling is the process of changing the sampling rate of a discrete signal to obtain a new discrete representation of the underlying continuous signal we'll upsample towards 10GHz increasing our timely accuracy from 0.3125ns to 0.1ns, this is possible as the full Nyquist-sampled waveforms are stored [41]. As the timely accuracy is now 0.1ns, the error on a time difference between channels is then 0.2ns. So $\delta t_{ij} = 0.2\text{ns}$ as explained in section 5.1.1.

After this cleaning of our data (by filtering and upsampling) we have a voltage response with an example shown for channel 0 in figure 5.9, we wish to find a sine wave coming from the weather balloon in this signal. To find a sine wave herein, and thus find out the timing of our signal, we'll make use of a method called *cross correlation*, whereby we move a template over our data, returning a high value if the data and template line up and a low value if they don't.

We thus need a template to correlate with the data. The template we'll be choosing is of course the sine function but it's important to notice that the channel has a certain sampling rate, namely now after up sampling, 10GHz.

Our template sine which we'll correlate to the data will also need to have this sampling rate, meaning that it needs to be step wise defined with spaces of 0.1ns. Next we'll also need to give

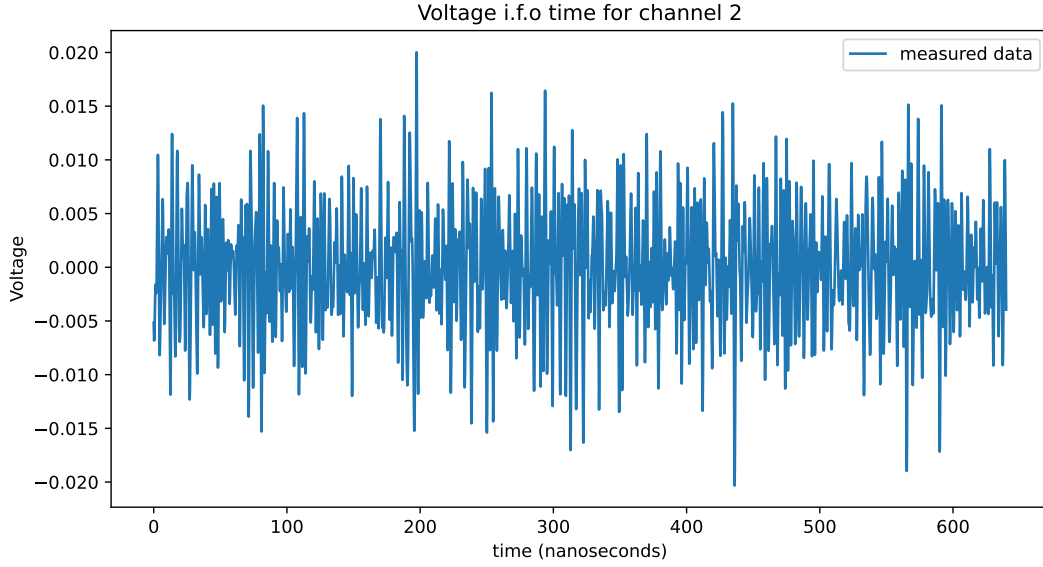


Figure 5.9: Recorded voltage i.f.o time in vpol antenna 2 after up sampling and passing through the butterworth filter, hereing we'll need to find a sinusoidal signal

the sine a certain amplitude, as we don't have a system for finding this let's assume an amplitude $A = 0.007$ (this shouldn't impact the result). Our template thus looks like this:

$$\mathcal{S} = A \cdot \sin(\omega t) \quad (5.29)$$

with

$$\omega = 2\pi f \quad (5.30)$$

With f the frequency of the balloon signal, 0.403GHz and t an array going from 0 to $3/f$ as to be able to fit 3 periods with intervals of 0.1ns, the cross-correlation is done by moving the signal with steps of $\Delta t = 0.1\text{ns}$, as is illustrated in figure 5.10. Mathematically this amounts to evaluating [53]:

$$(f \star g)(\tau) \triangleq \int_{-\infty}^{\infty} f(t)g(t + \tau)dt \quad (5.31)$$

With $f(t)$ the recorded signal and $g(t)$ the sine wave template.

In reality the data is a bit less perfect and after doing this correlation procedure on the real data we get what's (partially) shown in figure 5.11. Herein the peaks represent the maximal correlation, if we now do the same for channel 3 we have two correlation functions, if we cross-correlate these with each other we'll get the difference in timing between the channels. This is easy to comprehend after taking a look at the illustration shown in figure 5.12. How this cross-correlation of cross-correlated functions then looks like is shown in figure 5.13, the negative offset is caused by us accounting for cable delay. Note that multiple peak correlations are present. To find out which peak is the actual one, and with that finding out what the difference in arrival time is which we need to find our index of refraction, we'll need to analyse the physics of the problem.

Our signal is sinusoidal with a frequency of 0.403GHz, locally our index of refraction should be around 1.7, meaning that our wavelenght should be:

$$\lambda = \frac{v}{f} = \frac{c}{nf} \approx 0.44m \quad (5.32)$$

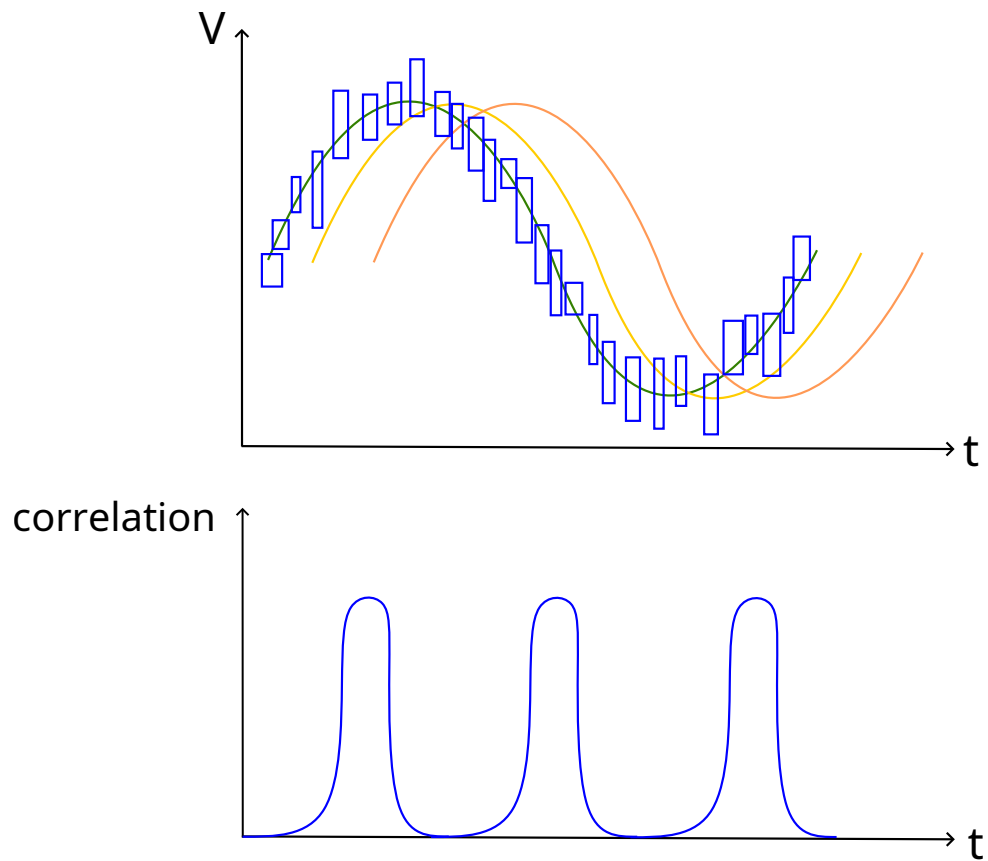


Figure 5.10: How correlating a sine with data leads to periodic peaks in the correlation function

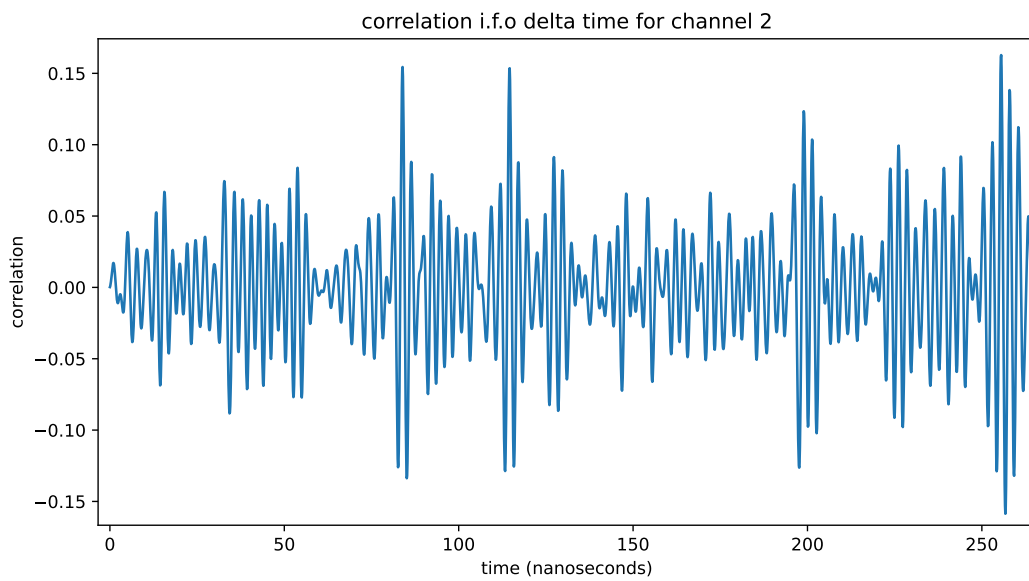


Figure 5.11: The correlation is less clear than in the illustration but still shows the periodicity of the sinusoidal signal

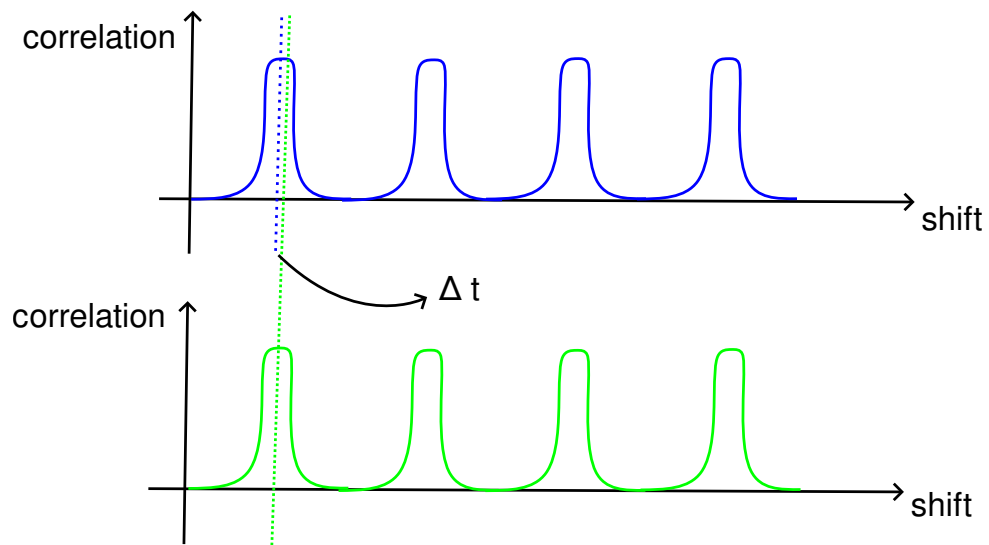


Figure 5.12: Crosscorrelating two crosscorrelated functions gives peaks at the differences in timing

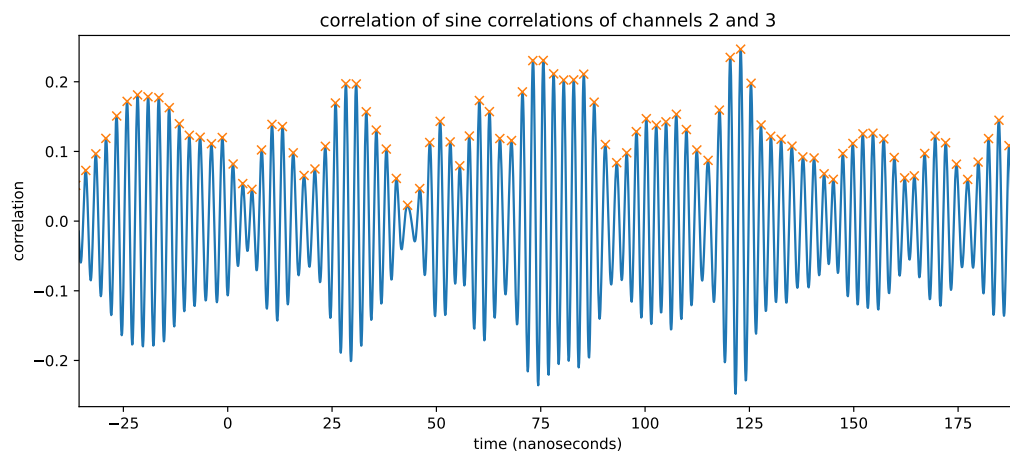


Figure 5.13: Crosscorrelating two crosscorrelated functions gives peaks at the differences in timing

This wavelength is longer than the distance between the individual channels, meaning that if the top of the sinusoidal wave gets detected in channel 2, then the sinusoidal wave gets detected in channel 3 $3 \frac{1m}{0.44m} \approx 2.3$ wavelengths later. So we expect at least two peaks to have gone by until the same sinusoidal wave as in channel 2 gets detected in channel 3. We thus have to search for the third peak (starting from $t=0$) in this case, similarly for detectors 0 and 3 which are spaced 3 meters apart we'll need to look at peak number $\lceil \frac{3m}{0.44m} \rceil = 7$. And for completeness sake, for channels spaced 2 meters apart we'll need to look at peak $\lceil \frac{2m}{0.44m} \rceil = 5$. In reality however, it is easier to just simulate the time differences and look in that neighbourhood.

Fitting n and finding it's error

Now that we have the differences in timing between the individual channels and their error, the angle the balloon makes with the detector and the distance between the individual channels all that's left to do is minimize function f as defined in equation 5.5 and calculate the error. Doing the full procedure we get as a result:

Depth (m)	Station id	channels	Run:Event	$n_{\text{exponential}}$	n_{fit}
-94.518	11	0&2&3	1034:12397	1.7397	$1.724 \pm 0.014 \pm 0.047$

With the first error indicating the systematic error and the second error the error found through error analysis. After changing the various errors it seems that the positional error is the biggest factor on accuracy.

5.4 Phased array and channels 5-7

The event we'll now analyse is recorded in detector 21 at the 26th of July 11:18:41 and falls within the $< 5^\circ$ mark, the balloon signal gets detected by both the phased array and channels 5 to 7.

Channels 5 to 7 lie at a very interesting depth as, looking at the density versus depth data shown in figure 3.2, here (40-80m depth) the difference between the density measurements and the single exponential model shows the largest deviations.

As channels 5 to 7 are spaced quite far apart we can do the plane wave fitting for two channels at a time, still keeping the error quite small. The results are given below:

Depth (m)	Station id	channels	Run:Event	$n_{\text{exponential}}$	n_{fit}
-48.155	21	6&7	1441:117	1.6400	$1.632 \pm 0.00128 \pm 0.00472$
-58.38	21	5&7	1441:117	1.6736	$1.66632 \pm 0.00226 \pm 0.00233$
-58.24	21	5&6&7	1441:117	1.67321	$1.66553 \pm 0.00167 \pm 0.00350$
-68.2	21	5&6	1441:117	1.6983	$1.69329 \pm 0.00199 \pm 0.00460$
-93.865	21	0&1&2&3	1441:117	1.73896	$1.71366 \pm 0.00287 \pm 0.05641$

5.5 Evaluation of the results

All the fits that were found are visually shown in figure 5.14, with a bigger version shown in appendix B together with the index found by converting the density data through the linear index-density relation ($n(z) \approx 1 + 0.845\rho(z)$) and the exponential model. Note that all of the indices that have been found have a value below the exponential model's, more closely to the converted density data. Even though the error is quite big these results could raise some

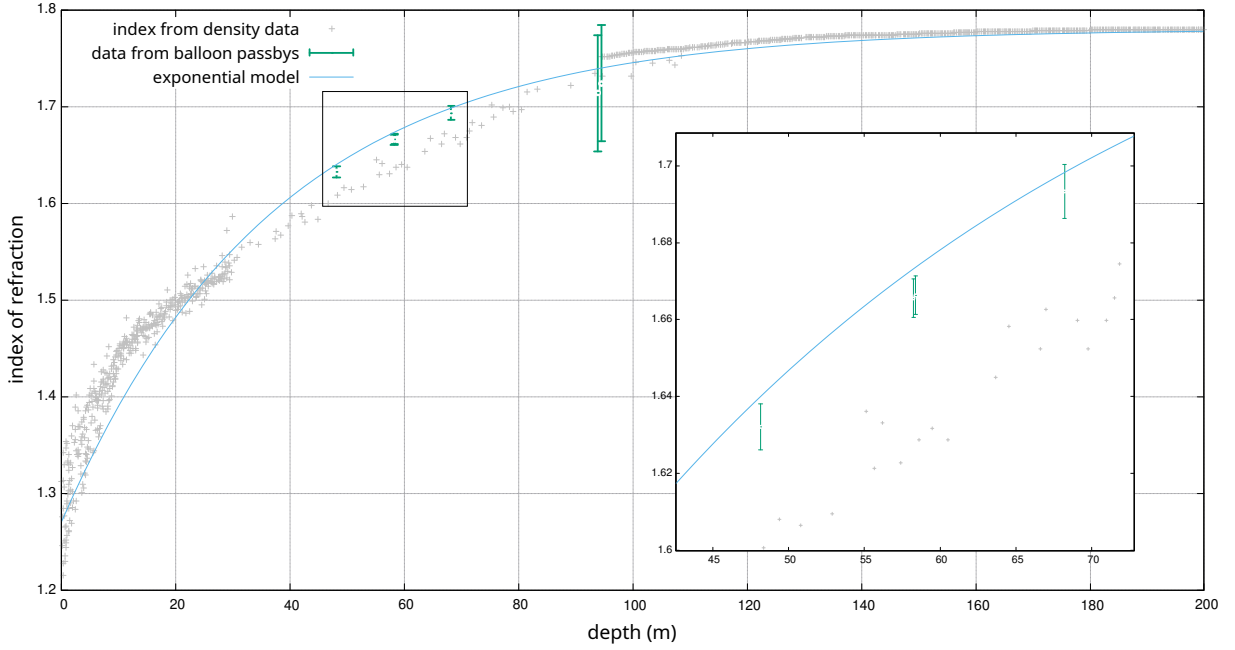


Figure 5.14: Even though the error bars are quite big, all values found within this chapter lie under the single exponential, which is especially clear at the phased array depths where the measurements are below both the exponential model and the data from the converted densities

suspicion on the validity of the exponential model and might indicate that it's needed to measure the whole index-depth profile.

Now note that the measurements on depths 40-80m don't fully agree with the density data, this could be caused by one of the following reasons:

- The density measurements aren't accurate enough
- The index isn't fully linear at every depth
- The fit isn't accurate enough and thus the error bars are underestimated

The density measurements do actually show quite a lot of spread for nearly the same values so there might be a problem there. There are also not that many recorded measurements in the 40-100m region and no reported uncertainties which makes the data less trustworthy.

As for the linearity relation, it has been extensively studied in the literature [54] and there seem to be multiple linear relationships reported, another one is e.g

$$n(z) \approx 1 + 0.77\rho(z) \quad (5.33)$$

How our data correlates with this relation is shown in figure B.1, but this doesn't seem to heavily impact the distance from the density converted data and our measurements.

CONCLUSION

The hybrid ray tracer developed over the course of this thesis and reported in chapter 4 was a success, not only is it more accurate than it's predecessors, as shown in figures 4.11 and 4.12, but it's also faster by about 34%. The accuracy of the ray tracer also makes it perfectly suitable for very fine precision simulations as used within the Balloon radio wave systematic error prediction.

The use of weather balloons to estimate the index of refraction as was reported in 5 was also done successfully yielding the following data:

Depth (m)	Station id	channels	Run:Event	$n_{\text{exponential}}$	n_{fit}
-48.155	21	6&7	1441:117	1.6400	$1.632 \pm 0.00128 \pm 0.00472$
-58.38	21	5&7	1441:117	1.6736	$1.66632 \pm 0.00226 \pm 0.00233$
-58.24	21	5&6&7	1441:117	1.67321	$1.66553 \pm 0.00167 \pm 0.00350$
-68.2	21	5&6	1441:117	1.6983	$1.69329 \pm 0.00199 \pm 0.00460$
-93.865	21	0&1&2&3	1441:117	1.73896	$1.71366 \pm 0.00287 \pm 0.05641$
-94.518	11	0&2&3	1034:12397	1.7397	$1.724 \pm 0.014 \pm 0.047$

It can be argued that this data shows a shortcoming of the exponential model. Because of this we reason that there's a need to investigate the index-depth relation further.

As there are a multitude of events (as can be found in appendices C and D but only finite time to analyze each and every one, this code is also made public [here](#) as to make it easy to improve on this work.

As this method seems to be a viable way of measuring the index of refraction, we'd want to use this method to determine a index-depth profile As has been done in the South Polar firm [55]. To do this we'd want some immobile close source and a phased array which we'll move down every couple of measurements. thus obtaining an index-depth profile using direct measurements. This might be carried out e.g during deployment of a new station's power string.

APPENDIX

A

LIST OF ABBREVIATIONS

- **AM:** Amplitude Modulated
- **AGN:** Active Galactic Nucleus
- **CMB:** Cosmic Microwave Background
- **DAQ:** Data Acquisition system
- **DnR:** Direct aNd Refracted
- **DSNB:** Diffuse Supernova Neutrino Background
- **FFT** Fast Fourier Transform
- **GRBs:** Gamma-Ray Bursts
- **RADIANT:** RAdio DIgitizer and Auxiliary Neutrino Trigger
- **RNO-G:** Radio Neutrino Observatory in Greenland
- **RF:** Radio Frequency
- **UHE:** Ultra High Energy
- **UHECRs:** Ultra High Energy Cosmic Rays

APPENDIX

B

EXTRA FIGURES

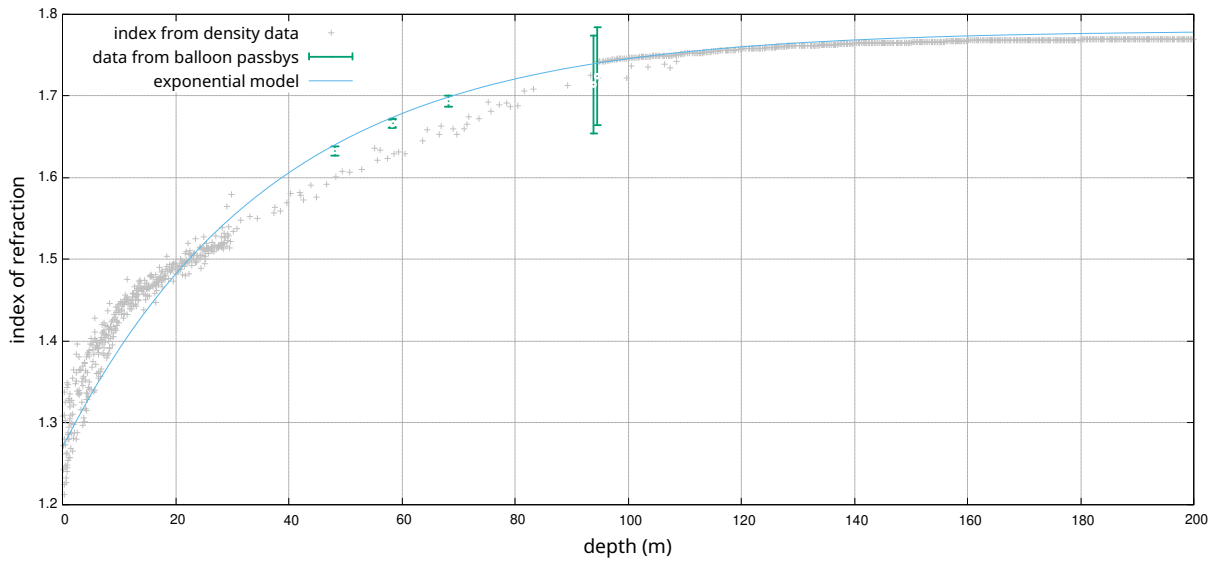


Figure B.1: Changing the linear index-density relation from $n(z) = 1 + 0.78\rho(z)$ to $n(z) = 1 + 0.77\rho(z)$ (shown here) seems to make our phased array measurements lie closer to the density data

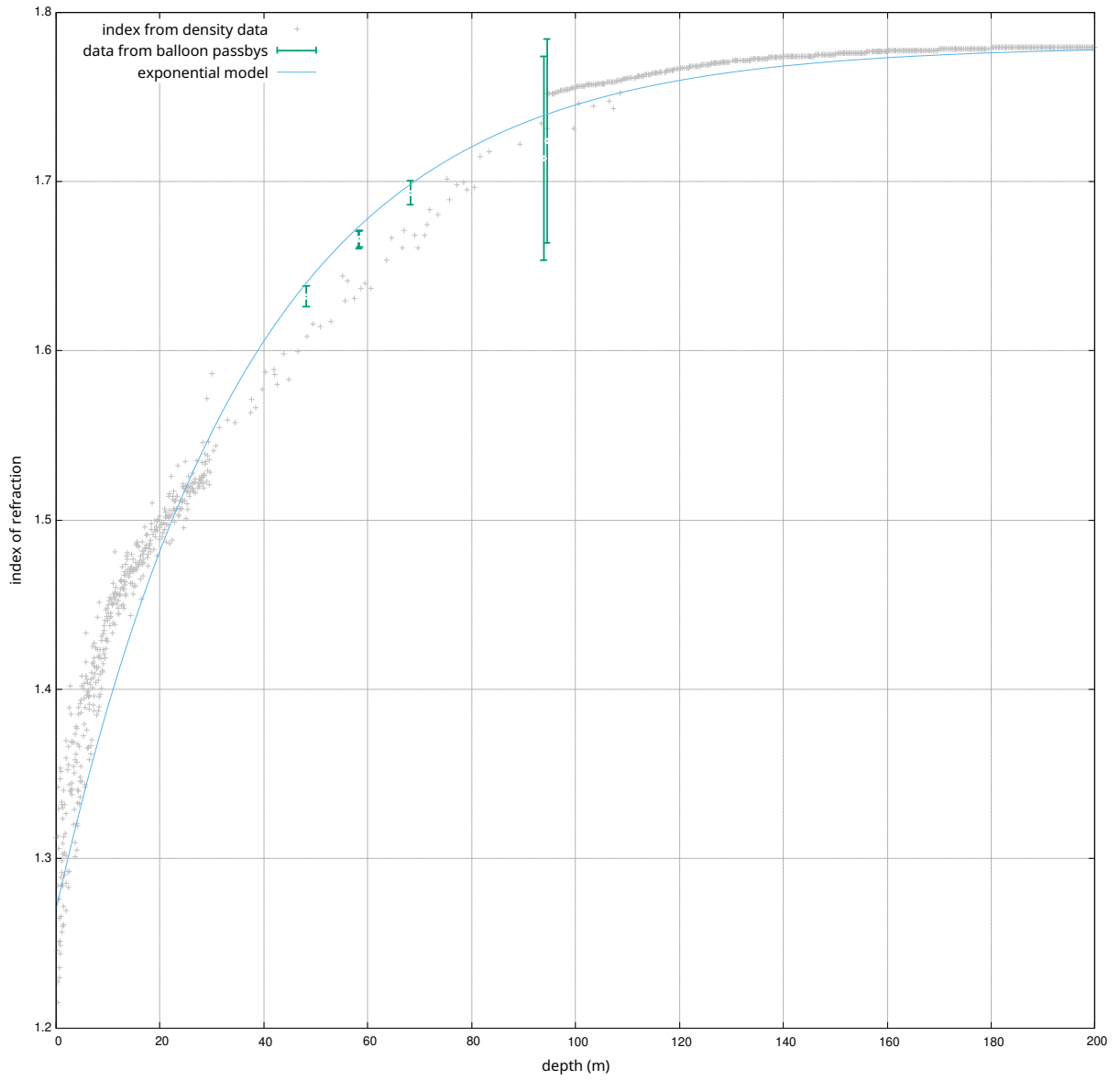


Figure B.2: In this bigger plot it's easier to see just where our measured values lie

APPENDIX

C

BALLOON PASSBYS UNDER 5° IN THE SUMMER OF 2022

Balloon filename (gpx)	station	expected timeframe
SMT_20220907_112500.gpx	23.00	2022-09-07 11:28:47+00:00 till 2022-09-07 11:28:49+00:00
SMT_20220728_112143.gpx	12.00	2022-07-28 11:36:42+00:00 till 2022-07-28 11:37:44+00:00
SMT_20220728_112143.gpx	11.00	2022-07-28 11:34:00+00:00 till 2022-07-28 11:35:37+00:00
SMT_20220728_112143.gpx	13.00	2022-07-28 11:38:18+00:00 till 2022-07-28 11:39:13+00:00
SMT_20220723_231622.gpx	21.00	2022-07-23 23:25:19+00:00 till 2022-07-23 23:27:24+00:00
SMT_20220723_231622.gpx	22.00	2022-07-23 23:31:22+00:00 till 2022-07-23 23:33:50+00:00
SMT_20220930_231507.gpx	13.00	2022-09-30 23:19:22+00:00 till 2022-09-30 23:19:23+00:00

APPENDIX C. BALLOON PASSBYS UNDER 5°
IN THE SUMMER OF 2022

Balloon filename (gpx)	station	expected timeframe
SMT_20220904_111459.gpx	21.00	2022-09-04 11:17:00+00:00 till 2022-09-04 11:17:49+00:00
SMT_20220904_111459.gpx	22.00	2022-09-04 11:21:12+00:00 till 2022-09-04 11:21:29+00:00
SMT_20220726_111605.gpx	21.00	2022-07-26 11:18:31+00:00 till 2022-07-26 11:18:47+00:00
SMT_20220726_111605.gpx	23.00	2022-07-26 11:27:32+00:00 till 2022-07-26 11:28:24+00:00
SMT_20220726_111605.gpx	24.00	2022-07-26 11:34:42+00:00 till 2022-07-26 11:40:36+00:00
SMT_20220826_113003.gpx	21.00	2022-08-26 11:32:14+00:00 till 2022-08-26 11:32:30+00:00
SMT_20220826_113003.gpx	13.00	2022-08-26 11:38:18+00:00 till 2022-08-26 11:39:04+00:00
SMT_20220714_231645.gpx	11.00	2022-07-14 23:30:57+00:00 till 2022-07-14 23:31:40+00:00
SMT_20220701_111515.gpx	11.00	2022-07-01 11:22:57+00:00 till 2022-07-01 11:25:30+00:00
SMT_20220725_112511.gpx	12.00	2022-07-25 11:29:41+00:00 till 2022-07-25 11:30:12+00:00
SMT_20220703_111803.gpx	24.00	2022-07-03 11:47:29+00:00 till 2022-07-03 11:50:43+00:00
SMT_20220820_111609.gpx	12.00	2022-08-20 11:24:37+00:00 till 2022-08-20 11:25:33+00:00
SMT_20220623_231633.gpx	13.00	2022-06-23 23:29:52+00:00 till 2022-06-23 23:30:59+00:00
SMT_20220623_231633.gpx	22.00	2022-06-23 23:23:50+00:00 till 2022-06-23 23:25:39+00:00
SMT_20220703_231627.gpx	21.00	2022-07-04 00:21:36+00:00 till 2022-07-04 00:42:14+00:00
SMT_20220703_231627.gpx	12.00	2022-07-04 00:32:03+00:00 till 2022-07-04 00:45:17+00:00
SMT_20220703_231627.gpx	11.00	2022-07-04 00:32:02+00:00 till 2022-07-04 00:47:35+00:00
SMT_20220703_231627.gpx	22.00	2022-07-04 00:21:47+00:00 till 2022-07-04 00:40:30+00:00
SMT_20220703_231627.gpx	23.00	2022-07-04 00:26:31+00:00 till 2022-07-04 00:34:55+00:00
SMT_20220624_231528.gpx	24.00	2022-06-25 00:29:26+00:00 till 2022-06-25 00:35:21+00:00
SMT_20220916_231807.gpx	22.00	2022-09-16 23:21:25+00:00 till 2022-09-16 23:21:49+00:00
SMT_20220908_111450.gpx	12.00	2022-09-08 11:20:23+00:00 till 2022-09-08 11:21:08+00:00
SMT_20220908_111450.gpx	13.00	2022-09-08 11:23:08+00:00 till 2022-09-08 11:23:54+00:00
SMT_20220817_111600.gpx	21.00	2022-08-17 11:31:37+00:00 till 2022-08-17 11:33:56+00:00
SMT_20220729_112533.gpx	11.00	2022-07-29 12:26:35+00:00 till 2022-07-29 12:31:35+00:00
SMT_20220907_231621.gpx	24.00	2022-09-07 23:24:23+00:00 till 2022-09-07 23:24:51+00:00
SMT_20220630_231835.gpx	21.00	2022-07-01 00:18:16+00:00 till 2022-07-01 00:32:45+00:00
SMT_20220630_231835.gpx	12.00	2022-07-01 00:25:19+00:00 till 2022-07-01 00:38:40+00:00
SMT_20220630_231835.gpx	11.00	2022-07-01 00:24:24+00:00 till 2022-07-01 00:37:58+00:00
SMT_20220630_231835.gpx	13.00	2022-07-01 00:30:30+00:00 till 2022-07-01 00:37:06+00:00
SMT_20220630_231835.gpx	22.00	2022-07-01 00:22:24+00:00 till 2022-07-01 00:34:12+00:00
SMT_20220826_231852.gpx	23.00	2022-08-26 23:27:09+00:00 till 2022-08-26 23:27:51+00:00
SMT_20220826_231852.gpx	24.00	2022-08-26 23:29:02+00:00 till 2022-08-26 23:29:48+00:00
SMT_20220624_111844.gpx	13.00	2022-06-24 11:33:51+00:00 till 2022-06-24 11:34:42+00:00
SMT_20220624_111844.gpx	22.00	2022-06-24 11:31:46+00:00 till 2022-06-24 11:32:35+00:00
SMT_20220707_112434.gpx	21.00	2022-07-07 12:31:12+00:00 till 2022-07-07 12:48:00+00:00
SMT_20220707_112434.gpx	12.00	2022-07-07 12:37:07+00:00 till 2022-07-07 12:49:22+00:00
SMT_20220707_112434.gpx	11.00	2022-07-07 12:36:00+00:00 till 2022-07-07 12:49:22+00:00
SMT_20220707_112434.gpx	13.00	2022-07-07 12:41:38+00:00 till 2022-07-07 12:49:22+00:00
SMT_20220707_112434.gpx	22.00	2022-07-07 12:34:46+00:00 till 2022-07-07 12:49:22+00:00
SMT_20220707_112434.gpx	23.00	2022-07-07 12:41:33+00:00 till 2022-07-07 12:48:09+00:00
SMT_20220829_111459.gpx	23.00	2022-08-29 11:18:46+00:00 till 2022-08-29 11:18:58+00:00
SMT_20220829_111459.gpx	24.00	2022-08-29 11:19:52+00:00 till 2022-08-29 11:20:10+00:00
SMT_20220727_232120.gpx	21.00	2022-07-27 23:24:53+00:00 till 2022-07-27 23:25:26+00:00
SMT_20220719_231514.gpx	11.00	2022-07-19 23:23:48+00:00 till 2022-07-19 23:26:06+00:00
SMT_20220807_231525.gpx	11.00	2022-08-07 23:18:35+00:00 till 2022-08-07 23:19:02+00:00
SMT_20220725_231505.gpx	13.00	2022-07-26 00:41:45+00:00 till 2022-07-26 00:53:49+00:00
SMT_20220725_231505.gpx	22.00	2022-07-25 23:22:13+00:00 till 2022-07-25 23:23:48+00:00
SMT_20220725_231505.gpx	23.00	2022-07-25 23:26:39+00:00 till 2022-07-26 00:48:25+00:00

APPENDIX C. BALLOON PASSBYS UNDER 5°
IN THE SUMMER OF 2022

Balloon filename (gpx)	station	expected timeframe
SMT_20220725_231505.gpx	23.00	2022-07-25 23:26:39+00:00 till 2022-07-26 00:48:25+00:00
SMT_20220725_231505.gpx	24.00	2022-07-26 00:35:23+00:00 till 2022-07-26 00:49:53+00:00
SMT_20220928_111604.gpx	11.00	2022-09-28 11:34:13+00:00 till 2022-09-28 11:35:36+00:00
SMT_20220808_231507.gpx	11.00	2022-08-08 23:18:40+00:00 till 2022-08-08 23:19:08+00:00
SMT_20220816_232314.gpx	22.00	2022-08-16 23:34:34+00:00 till 2022-08-16 23:35:09+00:00
SMT_20220704_231605.gpx	21.00	2022-07-04 23:23:47+00:00 till 2022-07-04 23:27:33+00:00
SMT_20220630_112143.gpx	21.00	2022-06-30 12:26:56+00:00 till 2022-06-30 12:38:03+00:00
SMT_20220630_112143.gpx	12.00	2022-06-30 12:31:57+00:00 till 2022-06-30 12:44:25+00:00
SMT_20220630_112143.gpx	11.00	2022-06-30 12:31:26+00:00 till 2022-06-30 12:42:23+00:00
SMT_20220630_112143.gpx	13.00	2022-06-30 12:34:40+00:00 till 2022-06-30 12:44:06+00:00
SMT_20220630_112143.gpx	22.00	2022-06-30 12:28:56+00:00 till 2022-06-30 12:39:23+00:00
SMT_20220630_112143.gpx	23.00	2022-06-30 12:33:15+00:00 till 2022-06-30 12:37:09+00:00
SMT_20220704_112103.gpx	21.00	2022-07-04 11:49:20+00:00 till 2022-07-04 11:55:43+00:00
SMT_20220704_112103.gpx	11.00	2022-07-04 11:45:32+00:00 till 2022-07-04 11:51:31+00:00
SMT_20220704_112103.gpx	13.00	2022-07-04 12:10:16+00:00 till 2022-07-04 12:11:52+00:00
SMT_20220704_112103.gpx	22.00	2022-07-04 11:52:45+00:00 till 2022-07-04 12:02:35+00:00
SMT_20220704_112103.gpx	23.00	2022-07-04 11:58:37+00:00 till 2022-07-04 12:16:54+00:00
SMT_20220704_112103.gpx	24.00	2022-07-04 12:06:21+00:00 till 2022-07-04 12:25:28+00:00
SMT_20220720_111442.gpx	23.00	2022-07-20 11:46:26+00:00 till 2022-07-20 11:50:05+00:00
SMT_20220720_111442.gpx	24.00	2022-07-20 11:50:53+00:00 till 2022-07-20 12:03:52+00:00
SMT_20220829_231438.gpx	22.00	2022-08-29 23:16:33+00:00 till 2022-08-29 23:16:38+00:00
SMT_20220829_231438.gpx	23.00	2022-08-29 23:17:45+00:00 till 2022-08-29 23:17:58+00:00
SMT_20220921_231851.gpx	12.00	2022-09-22 10:46:18+00:00 till 2022-09-22 10:46:19+00:00
SMT_20220821_111511.gpx	21.00	2022-08-21 12:39:53+00:00 till 2022-08-21 12:56:06+00:00
SMT_20220821_111511.gpx	12.00	2022-08-21 12:51:06+00:00 till 2022-08-21 12:56:06+00:00
SMT_20220821_111511.gpx	11.00	2022-08-21 12:51:32+00:00 till 2022-08-21 12:56:06+00:00
SMT_20220821_111511.gpx	13.00	2022-08-21 12:52:27+00:00 till 2022-08-21 12:56:06+00:00
SMT_20220821_111511.gpx	22.00	2022-08-21 12:40:26+00:00 till 2022-08-21 12:56:06+00:00
SMT_20220821_111511.gpx	23.00	2022-08-21 12:43:03+00:00 till 2022-08-21 12:56:06+00:00
SMT_20220724_231539.gpx	11.00	2022-07-24 23:20:04+00:00 till 2022-07-24 23:21:11+00:00
SMT_20220827_111534.gpx	24.00	2022-08-27 11:23:00+00:00 till 2022-08-27 11:23:07+00:00
SMT_20220625_111630.gpx	21.00	2022-06-25 12:27:31+00:00 till 2022-06-25 12:35:22+00:00
SMT_20220625_111630.gpx	12.00	2022-06-25 12:30:09+00:00 till 2022-06-25 12:39:40+00:00
SMT_20220625_111630.gpx	11.00	2022-06-25 12:32:45+00:00 till 2022-06-25 12:37:21+00:00
SMT_20220625_111630.gpx	13.00	2022-06-25 12:30:42+00:00 till 2022-06-25 12:40:11+00:00
SMT_20220625_111630.gpx	22.00	2022-06-25 12:27:03+00:00 till 2022-06-25 12:37:11+00:00
SMT_20220625_111630.gpx	23.00	2022-06-25 12:28:31+00:00 till 2022-06-25 12:37:18+00:00

APPENDIX

D

BALLOON PASSBYS UNDER 10° IN THE SUMMER OF 2022

Balloon filename (gpx)	station	expected timeframe
SMT_20220719_231514.gpx	21	2022-07-19 23:19:46+00:00 till 2022-07-19 23:20:41+00:00
SMT_20220719_231514.gpx	11	2022-07-19 23:22:44+00:00 till 2022-07-19 23:27:19+00:00
SMT_20220831_111419.gpx	11	2022-08-31 11:16:20+00:00 till 2022-08-31 11:16:26+00:00
SMT_20220625_111630.gpx	21	2022-06-25 12:22:22+00:00 till 2022-06-25 12:40:57+00:00
SMT_20220625_111630.gpx	12	2022-06-25 12:25:55+00:00 till 2022-06-25 12:45:40+00:00
SMT_20220625_111630.gpx	11	2022-06-25 12:25:58+00:00 till 2022-06-25 12:45:09+00:00
SMT_20220625_111630.gpx	13	2022-06-25 12:26:44+00:00 till 2022-06-25 12:45:40+00:00
SMT_20220625_111630.gpx	22	2022-06-25 12:22:25+00:00 till 2022-06-25 12:42:40+00:00
SMT_20220625_111630.gpx	23	2022-06-25 12:24:10+00:00 till 2022-06-25 12:43:09+00:00
SMT_20220625_111630.gpx	24	2022-06-25 12:26:32+00:00 till 2022-06-25 12:42:24+00:00
SMT_20220826_113003.gpx	21	2022-08-26 11:32:04+00:00 till 2022-08-26 11:32:42+00:00
SMT_20220826_113003.gpx	13	2022-08-26 11:37:48+00:00 till 2022-08-26 11:39:40+00:00
SMT_20220626_112912.gpx	11	2022-06-26 11:35:52+00:00 till 2022-06-26 11:37:32+00:00
SMT_20220808_231507.gpx	11	2022-08-08 23:18:27+00:00 till 2022-08-08 23:19:24+00:00

APPENDIX D. BALLOON PASSBYS UNDER 10°
IN THE SUMMER OF 2022

Balloon filename (gpx)	station	expected timeframe
SMT_20220724_231539.gpx	11	2022-07-24 23:19:27+00:00 till 2022-07-24 23:21:58+00:00
SMT_20220724_231539.gpx	13	2022-07-25 00:19:35+00:00 till 2022-07-25 00:32:09+00:00
SMT_20220829_231438.gpx	22	2022-08-29 23:16:29+00:00 till 2022-08-29 23:16:42+00:00
SMT_20220829_231438.gpx	23	2022-08-29 23:17:39+00:00 till 2022-08-29 23:18:04+00:00
SMT_20220829_231438.gpx	24	2022-08-29 23:18:59+00:00 till 2022-08-29 23:19:22+00:00
SMT_20220916_231807.gpx	21	2022-09-16 23:19:09+00:00 till 2022-09-16 23:19:17+00:00
SMT_20220916_231807.gpx	22	2022-09-16 23:21:13+00:00 till 2022-09-16 23:22:03+00:00
SMT_20220816_232314.gpx	22	2022-08-16 23:33:11+00:00 till 2022-08-16 23:37:34+00:00
SMT_20220907_112500.gpx	23	2022-09-07 11:28:37+00:00 till 2022-09-07 11:28:59+00:00
SMT_20220907_112500.gpx	24	2022-09-07 11:29:35+00:00 till 2022-09-07 11:29:53+00:00
SMT_20220628_231514.gpx	12	2022-06-28 23:19:37+00:00 till 2022-06-28 23:20:55+00:00
SMT_20220630_112143.gpx	21	2022-06-30 12:21:02+00:00 till 2022-06-30 12:46:53+00:00
SMT_20220630_112143.gpx	12	2022-06-30 12:26:35+00:00 till 2022-06-30 12:48:30+00:00
SMT_20220630_112143.gpx	11	2022-06-30 12:25:33+00:00 till 2022-06-30 12:48:30+00:00
SMT_20220630_112143.gpx	13	2022-06-30 12:28:56+00:00 till 2022-06-30 12:48:30+00:00
SMT_20220630_112143.gpx	22	2022-06-30 12:23:21+00:00 till 2022-06-30 12:47:42+00:00
SMT_20220630_112143.gpx	23	2022-06-30 12:26:20+00:00 till 2022-06-30 12:47:25+00:00
SMT_20220630_112143.gpx	24	2022-06-30 12:30:34+00:00 till 2022-06-30 12:46:14+00:00
SMT_20220725_231505.gpx	21	2022-07-25 23:17:47+00:00 till 2022-07-26 00:53:39+00:00
SMT_20220725_231505.gpx	12	2022-07-26 00:38:19+00:00 till 2022-07-26 00:55:04+00:00
SMT_20220725_231505.gpx	11	2022-07-26 00:45:41+00:00 till 2022-07-26 00:55:04+00:00
SMT_20220725_231505.gpx	13	2022-07-26 00:34:56+00:00 till 2022-07-26 00:55:04+00:00
SMT_20220725_231505.gpx	22	2022-07-25 23:21:41+00:00 till 2022-07-26 00:55:04+00:00
SMT_20220725_231505.gpx	23	2022-07-25 23:25:16+00:00 till 2022-07-26 00:55:04+00:00
SMT_20220725_231505.gpx	24	2022-07-26 00:25:43+00:00 till 2022-07-26 00:55:04+00:00
SMT_20220703_111803.gpx	22	2022-07-03 11:40:24+00:00 till 2022-07-03 11:42:55+00:00
SMT_20220703_111803.gpx	23	2022-07-03 11:42:26+00:00 till 2022-07-03 11:49:33+00:00
SMT_20220703_111803.gpx	24	2022-07-03 11:45:29+00:00 till 2022-07-03 11:52:37+00:00
SMT_20220820_111609.gpx	21	2022-08-20 11:19:36+00:00 till 2022-08-20 11:21:16+00:00
SMT_20220820_111609.gpx	12	2022-08-20 11:24:02+00:00 till 2022-08-20 11:26:23+00:00
SMT_20220624_231528.gpx	12	2022-06-25 00:33:09+00:00 till 2022-06-25 00:40:51+00:00
SMT_20220624_231528.gpx	13	2022-06-25 00:28:45+00:00 till 2022-06-25 00:40:56+00:00
SMT_20220624_231528.gpx	22	2022-06-25 00:31:15+00:00 till 2022-06-25 00:34:40+00:00
SMT_20220624_231528.gpx	23	2022-06-25 00:24:52+00:00 till 2022-06-25 00:40:56+00:00
SMT_20220624_231528.gpx	24	2022-06-25 00:23:18+00:00 till 2022-06-25 00:40:56+00:00
SMT_20220701_111515.gpx	11	2022-07-01 11:21:58+00:00 till 2022-07-01 11:26:31+00:00
SMT_20220930_111518.gpx	12	2022-09-30 11:19:46+00:00 till 2022-09-30 11:20:04+00:00
SMT_20220821_111511.gpx	21	2022-08-21 12:30:15+00:00 till 2022-08-21 12:56:06+00:00
SMT_20220821_111511.gpx	12	2022-08-21 12:37:45+00:00 till 2022-08-21 12:56:06+00:00
SMT_20220821_111511.gpx	11	2022-08-21 12:37:28+00:00 till 2022-08-21 12:56:06+00:00
SMT_20220821_111511.gpx	13	2022-08-21 12:39:39+00:00 till 2022-08-21 12:56:06+00:00
SMT_20220821_111511.gpx	22	2022-08-21 12:31:58+00:00 till 2022-08-21 12:56:06+00:00
SMT_20220821_111511.gpx	23	2022-08-21 12:33:47+00:00 till 2022-08-21 12:56:06+00:00
SMT_20220821_111511.gpx	24	2022-08-21 12:39:51+00:00 till 2022-08-21 12:56:06+00:00
SMT_20220813_112235.gpx	21	2022-08-13 11:12:14+00:00 till 2022-08-13 11:12:14+00:00
SMT_20220714_231645.gpx	12	2022-07-14 23:33:22+00:00 till 2022-07-14 23:38:49+00:00
SMT_20220714_231645.gpx	11	2022-07-14 23:27:54+00:00 till 2022-07-14 23:35:34+00:00
SMT_20220714_231645.gpx	13	2022-07-14 23:37:48+00:00 till 2022-07-14 23:46:03+00:00
SMT_20220723_231622.gpx	21	2022-07-23 23:21:03+00:00 till 2022-07-23 23:30:26+00:00

APPENDIX D. BALLOON PASSBYS UNDER 10°
IN THE SUMMER OF 2022

Balloon filename (gpx)	station	expected timeframe
SMT_20220723_231622.gpx	21	2022-07-23 23:21:03+00:00 till 2022-07-23 23:30:26+00:00
SMT_20220723_231622.gpx	22	2022-07-23 23:30:12+00:00 till 2022-07-23 23:35:27+00:00
SMT_20220723_231622.gpx	23	2022-07-23 23:33:26+00:00 till 2022-07-23 23:37:57+00:00
SMT_20220723_231622.gpx	24	2022-07-23 23:36:33+00:00 till 2022-07-23 23:39:18+00:00
SMT_20220701_231934.gpx	22	2022-07-01 23:08:19+00:00 till 2022-07-01 23:08:19+00:00
SMT_20220701_231934.gpx	23	2022-07-01 23:08:19+00:00 till 2022-07-01 23:08:19+00:00
SMT_20220830_231921.gpx	12	2022-08-30 23:22:15+00:00 till 2022-08-30 23:22:31+00:00
SMT_20220706_231615.gpx	22	2022-07-07 00:34:24+00:00 till 2022-07-07 00:35:15+00:00
SMT_20220706_231615.gpx	23	2022-07-07 00:33:30+00:00 till 2022-07-07 00:35:15+00:00
SMT_20220706_231615.gpx	24	2022-07-07 00:33:50+00:00 till 2022-07-07 00:35:15+00:00
SMT_20220728_112143.gpx	12	2022-07-28 11:36:04+00:00 till 2022-07-28 11:38:16+00:00
SMT_20220728_112143.gpx	11	2022-07-28 11:32:06+00:00 till 2022-07-28 11:36:28+00:00
SMT_20220728_112143.gpx	13	2022-07-28 11:37:48+00:00 till 2022-07-28 11:39:49+00:00
SMT_20220716_111633.gpx	21	2022-07-16 12:05:05+00:00 till 2022-07-16 12:20:22+00:00
SMT_20220716_111633.gpx	12	2022-07-16 12:10:53+00:00 till 2022-07-16 12:24:07+00:00
SMT_20220716_111633.gpx	11	2022-07-16 12:08:23+00:00 till 2022-07-16 12:25:43+00:00
SMT_20220716_111633.gpx	22	2022-07-16 12:09:06+00:00 till 2022-07-16 12:18:35+00:00
SMT_20220715_231621.gpx	21	2022-07-16 00:08:58+00:00 till 2022-07-16 00:12:03+00:00
SMT_20220726_111605.gpx	21	2022-07-26 11:18:19+00:00 till 2022-07-26 11:19:03+00:00
SMT_20220726_111605.gpx	12	2022-07-26 12:20:14+00:00 till 2022-07-26 12:21:53+00:00
SMT_20220726_111605.gpx	13	2022-07-26 12:06:52+00:00 till 2022-07-26 12:30:56+00:00
SMT_20220726_111605.gpx	22	2022-07-26 11:21:46+00:00 till 2022-07-26 11:24:39+00:00
SMT_20220726_111605.gpx	23	2022-07-26 11:26:09+00:00 till 2022-07-26 12:22:24+00:00
SMT_20220726_111605.gpx	24	2022-07-26 11:31:17+00:00 till 2022-07-26 12:25:10+00:00
SMT_20220726_231510.gpx	11	2022-07-26 23:31:39+00:00 till 2022-07-26 23:43:04+00:00
SMT_20220724_111936.gpx	11	2022-07-24 11:24:45+00:00 till 2022-07-24 11:27:03+00:00
SMT_20220724_111936.gpx	13	2022-07-24 12:23:16+00:00 till 2022-07-24 12:33:48+00:00
SMT_20220724_111936.gpx	24	2022-07-24 12:12:44+00:00 till 2022-07-24 12:29:27+00:00
SMT_20220820_231751.gpx	13	2022-08-20 23:41:03+00:00 till 2022-08-20 23:45:01+00:00
SMT_20220820_231751.gpx	22	2022-08-20 23:39:20+00:00 till 2022-08-20 23:41:29+00:00
SMT_20220820_231751.gpx	23	2022-08-20 23:39:47+00:00 till 2022-08-20 23:42:41+00:00
SMT_20220703_231627.gpx	21	2022-07-03 23:58:58+00:00 till 2022-07-04 00:51:57+00:00
SMT_20220703_231627.gpx	12	2022-07-04 00:19:47+00:00 till 2022-07-04 00:52:09+00:00
SMT_20220703_231627.gpx	11	2022-07-04 00:19:37+00:00 till 2022-07-04 00:52:09+00:00
SMT_20220703_231627.gpx	13	2022-07-04 00:22:04+00:00 till 2022-07-04 00:52:07+00:00
SMT_20220703_231627.gpx	22	2022-07-04 00:14:09+00:00 till 2022-07-04 00:50:28+00:00
SMT_20220703_231627.gpx	23	2022-07-04 00:17:51+00:00 till 2022-07-04 00:48:29+00:00
SMT_20220703_231627.gpx	24	2022-07-04 00:23:40+00:00 till 2022-07-04 00:42:26+00:00
SMT_20220816_111548.gpx	11	2022-08-16 11:19:06+00:00 till 2022-08-16 11:20:08+00:00
SMT_20220704_231605.gpx	21	2022-07-04 23:21:14+00:00 till 2022-07-04 23:29:47+00:00
SMT_20220704_231605.gpx	22	2022-07-05 00:45:35+00:00 till 2022-07-05 00:46:21+00:00
SMT_20220704_231605.gpx	23	2022-07-05 00:44:35+00:00 till 2022-07-05 00:46:21+00:00
SMT_20220704_231605.gpx	24	2022-07-05 00:44:08+00:00 till 2022-07-05 00:46:21+00:00
SMT_20220921_231851.gpx	12	2022-09-22 10:46:18+00:00 till 2022-09-22 10:46:20+00:00
SMT_20220921_231851.gpx	13	2022-09-22 10:46:21+00:00 till 2022-09-22 10:46:22+00:00
SMT_20220630_231835.gpx	21	2022-07-01 00:11:25+00:00 till 2022-07-01 00:39:49+00:00
SMT_20220630_231835.gpx	12	2022-07-01 00:19:34+00:00 till 2022-07-01 00:45:51+00:00
SMT_20220630_231835.gpx	11	2022-07-01 00:17:35+00:00 till 2022-07-01 00:45:17+00:00

APPENDIX D. BALLOON PASSBYS UNDER 10°
IN THE SUMMER OF 2022

Balloon filename (gpx)	station	expected timeframe
SMT_20220630_231835.gpx	13	2022-07-01 00:23:23+00:00 till 2022-07-01 00:45:28+00:00
SMT_20220630_231835.gpx	22	2022-07-01 00:17:04+00:00 till 2022-07-01 00:40:11+00:00
SMT_20220630_231835.gpx	23	2022-07-01 00:21:11+00:00 till 2022-07-01 00:39:32+00:00
SMT_20220630_231835.gpx	24	2022-07-01 00:26:47+00:00 till 2022-07-01 00:37:45+00:00
SMT_20220807_231525.gpx	11	2022-08-07 23:18:24+00:00 till 2022-08-07 23:19:22+00:00
SMT_20220727_232120.gpx	21	2022-07-27 23:24:29+00:00 till 2022-07-27 23:25:46+00:00
SMT_20220727_232120.gpx	22	2022-07-27 23:27:22+00:00 till 2022-07-27 23:27:30+00:00
SMT_20220727_232120.gpx	23	2022-07-27 23:31:39+00:00 till 2022-07-27 23:32:39+00:00
SMT_20220727_232120.gpx	24	2022-07-27 23:33:29+00:00 till 2022-07-27 23:36:31+00:00
SMT_20220707_112434.gpx	21	2022-07-07 12:23:11+00:00 till 2022-07-07 12:49:22+00:00
SMT_20220707_112434.gpx	12	2022-07-07 12:31:06+00:00 till 2022-07-07 12:49:22+00:00
SMT_20220707_112434.gpx	11	2022-07-07 12:28:16+00:00 till 2022-07-07 12:49:22+00:00
SMT_20220707_112434.gpx	13	2022-07-07 12:34:19+00:00 till 2022-07-07 12:49:22+00:00
SMT_20220707_112434.gpx	22	2022-07-07 12:26:02+00:00 till 2022-07-07 12:49:22+00:00
SMT_20220707_112434.gpx	23	2022-07-07 12:32:01+00:00 till 2022-07-07 12:49:22+00:00
SMT_20220707_112434.gpx	24	2022-07-07 12:37:10+00:00 till 2022-07-07 12:49:22+00:00
SMT_20220617_231459.gpx	22	2022-06-17 23:17:36+00:00 till 2022-06-17 23:17:58+00:00
SMT_20220826_231852.gpx	23	2022-08-26 23:26:43+00:00 till 2022-08-26 23:28:19+00:00
SMT_20220826_231852.gpx	24	2022-08-26 23:28:41+00:00 till 2022-08-26 23:30:12+00:00
SMT_20220828_111632.gpx	22	2022-08-28 11:21:14+00:00 till 2022-08-28 11:23:09+00:00
SMT_20220828_111632.gpx	23	2022-08-28 11:24:07+00:00 till 2022-08-28 11:25:44+00:00
SMT_20220828_111632.gpx	24	2022-08-28 11:26:44+00:00 till 2022-08-28 11:28:09+00:00
SMT_20220623_231633.gpx	13	2022-06-23 23:29:11+00:00 till 2022-06-23 23:31:38+00:00
SMT_20220623_231633.gpx	22	2022-06-23 23:23:06+00:00 till 2022-06-23 23:26:51+00:00
SMT_20220807_111547.gpx	12	2022-08-07 11:22:02+00:00 till 2022-08-07 11:22:59+00:00
SMT_20220807_111547.gpx	13	2022-08-07 11:26:06+00:00 till 2022-08-07 11:27:55+00:00
SMT_20220624_111844.gpx	12	2022-06-24 11:33:01+00:00 till 2022-06-24 11:33:33+00:00
SMT_20220624_111844.gpx	13	2022-06-24 11:33:25+00:00 till 2022-06-24 11:35:11+00:00
SMT_20220624_111844.gpx	22	2022-06-24 11:31:13+00:00 till 2022-06-24 11:33:06+00:00
SMT_20220929_111540.gpx	12	2022-09-29 11:19:52+00:00 till 2022-09-29 11:20:48+00:00
SMT_20220720_111442.gpx	21	2022-07-20 11:28:20+00:00 till 2022-07-20 11:34:28+00:00
SMT_20220720_111442.gpx	22	2022-07-20 11:32:55+00:00 till 2022-07-20 11:49:29+00:00
SMT_20220720_111442.gpx	23	2022-07-20 11:37:02+00:00 till 2022-07-20 12:04:15+00:00
SMT_20220720_111442.gpx	24	2022-07-20 11:44:43+00:00 till 2022-07-20 12:12:56+00:00
SMT_20220829_111459.gpx	21	2022-08-29 11:15:53+00:00 till 2022-08-29 11:15:59+00:00
SMT_20220829_111459.gpx	23	2022-08-29 11:18:35+00:00 till 2022-08-29 11:19:05+00:00
SMT_20220829_111459.gpx	24	2022-08-29 11:19:44+00:00 till 2022-08-29 11:20:20+00:00
SMT_20220705_113009.gpx	21	2022-07-05 12:48:04+00:00 till 2022-07-05 12:53:24+00:00
SMT_20220705_113009.gpx	11	2022-07-05 12:50:13+00:00 till 2022-07-05 12:53:24+00:00
SMT_20220817_111600.gpx	21	2022-08-17 11:20:21+00:00 till 2022-08-17 11:35:09+00:00
SMT_20220817_111600.gpx	11	2022-08-17 11:27:50+00:00 till 2022-08-17 11:30:32+00:00
SMT_20220904_111459.gpx	21	2022-09-04 11:16:45+00:00 till 2022-09-04 11:18:39+00:00
SMT_20220904_111459.gpx	22	2022-09-04 11:20:46+00:00 till 2022-09-04 11:21:55+00:00
SMT_20220904_111459.gpx	23	2022-09-04 11:22:57+00:00 till 2022-09-04 11:24:53+00:00
SMT_20220904_111459.gpx	24	2022-09-04 11:24:58+00:00 till 2022-09-04 11:25:49+00:00
SMT_20220928_111604.gpx	12	2022-09-28 11:37:02+00:00 till 2022-09-28 11:38:16+00:00
SMT_20220928_111604.gpx	11	2022-09-28 11:33:16+00:00 till 2022-09-28 11:36:59+00:00
SMT_20220930_231507.gpx	13	2022-09-30 23:19:10+00:00 till 2022-09-30 23:19:35+00:00

Balloon filename (gpx)	station	expected timeframe
SMT_20220904_231730.gpx	24	2022-09-04 23:22:54+00:00 till 2022-09-04 23:23:14+00:00
SMT_20220921_111527.gpx	12	2022-09-21 11:27:31+00:00 till 2022-09-21 11:29:09+00:00
SMT_20220921_111527.gpx	11	2022-09-21 11:25:37+00:00 till 2022-09-21 11:27:09+00:00
SMT_20220921_111527.gpx	13	2022-09-21 11:29:18+00:00 till 2022-09-21 11:30:46+00:00
SMT_20220725_112511.gpx	12	2022-07-25 11:29:27+00:00 till 2022-07-25 11:30:29+00:00
SMT_20220907_231621.gpx	23	2022-09-07 23:22:59+00:00 till 2022-09-07 23:23:40+00:00
SMT_20220907_231621.gpx	24	2022-09-07 23:24:09+00:00 till 2022-09-07 23:25:07+00:00
SMT_20220827_111534.gpx	24	2022-08-27 11:22:30+00:00 till 2022-08-27 11:23:43+00:00
SMT_20220615_231713.gpx	12	2022-06-15 23:21:29+00:00 till 2022-06-15 23:22:47+00:00
SMT_20220908_111450.gpx	12	2022-09-08 11:20:02+00:00 till 2022-09-08 11:21:40+00:00
SMT_20220908_111450.gpx	13	2022-09-08 11:22:39+00:00 till 2022-09-08 11:24:21+00:00
SMT_20220616_231523.gpx	11	2022-06-16 23:17:55+00:00 till 2022-06-16 23:18:16+00:00
SMT_20220729_112533.gpx	21	2022-07-29 12:19:23+00:00 till 2022-07-29 12:33:04+00:00
SMT_20220729_112533.gpx	12	2022-07-29 12:26:18+00:00 till 2022-07-29 12:36:15+00:00
SMT_20220729_112533.gpx	11	2022-07-29 12:21:20+00:00 till 2022-07-29 12:37:29+00:00
SMT_20220704_112103.gpx	21	2022-07-04 11:46:05+00:00 till 2022-07-04 12:00:57+00:00
SMT_20220704_112103.gpx	12	2022-07-04 11:48:49+00:00 till 2022-07-04 12:35:14+00:00
SMT_20220704_112103.gpx	11	2022-07-04 11:41:27+00:00 till 2022-07-04 11:58:58+00:00
SMT_20220704_112103.gpx	13	2022-07-04 11:56:33+00:00 till 2022-07-04 12:40:36+00:00
SMT_20220704_112103.gpx	22	2022-07-04 11:49:29+00:00 till 2022-07-04 12:25:01+00:00
SMT_20220704_112103.gpx	23	2022-07-04 11:54:52+00:00 till 2022-07-04 12:33:48+00:00
SMT_20220704_112103.gpx	24	2022-07-04 11:59:40+00:00 till 2022-07-04 12:34:54+00:00
SMT_20220825_112057.gpx	12	2022-08-25 11:25:22+00:00 till 2022-08-25 11:25:43+00:00
SMT_20220712_111713.gpx	11	2022-07-12 12:29:00+00:00 till 2022-07-12 12:30:52+00:00
SMT_20220628_111612.gpx	11	2022-06-28 11:19:17+00:00 till 2022-06-28 11:19:27+00:00
SMT_20220702_231622.gpx	21	2022-07-03 00:14:37+00:00 till 2022-07-03 00:47:11+00:00
SMT_20220702_231622.gpx	12	2022-07-03 00:22:20+00:00 till 2022-07-03 00:52:30+00:00
SMT_20220702_231622.gpx	11	2022-07-03 00:29:05+00:00 till 2022-07-03 00:52:25+00:00
SMT_20220702_231622.gpx	13	2022-07-03 00:21:33+00:00 till 2022-07-03 00:52:30+00:00
SMT_20220702_231622.gpx	22	2022-07-03 00:11:26+00:00 till 2022-07-03 00:50:35+00:00
SMT_20220702_231622.gpx	23	2022-07-03 00:14:24+00:00 till 2022-07-03 00:51:28+00:00
SMT_20220702_231622.gpx	24	2022-07-03 00:16:28+00:00 till 2022-07-03 00:51:10+00:00
SMT_20220706_112237.gpx	21	2022-07-06 12:48:26+00:00 till 2022-07-06 12:48:49+00:00
SMT_20220803_232212.gpx	21	2022-08-03 23:23:53+00:00 till 2022-08-03 23:23:54+00:00
SMT_20220803_232212.gpx	22	2022-08-03 23:26:19+00:00 till 2022-08-03 23:27:55+00:00
SMT_20220803_232212.gpx	23	2022-08-03 23:29:46+00:00 till 2022-08-03 23:34:09+00:00
SMT_20220803_232212.gpx	24	2022-08-03 23:34:19+00:00 till 2022-08-03 23:38:20+00:00

REFERENCES OF FIGURES

- [Fig1] A. Jash, “Studies on the physics of resistive plate chambers in relation to the ino experiment,” Ph.D. dissertation, 04 2018.
- [Fig2] “Wikimedia commons file:fusion in the sun.svg,” https://en.wikipedia.org/wiki/File:Fusion_in_the_Sun.svg.
- [Fig3] “Wikimedia commons file:binding energy curve - common isotopes.svg,” https://en.wikipedia.org/wiki/File:Binding_energy_curve_-_common_isotopes.svg.
- [Fig4] “Argonne national laboratory advanced test reactor core, idaho national laboratory,” https://en.wikipedia.org/wiki/File:Advanced_Test_Reactor.jpg.
- [Fig5] “File:cherenkov.svg by arpad horvath,” <https://commons.wikimedia.org/wiki/File:Cherenkov.svg>.
- [Fig6] “Wikimedia commons file:greenland (orthographic projection).svg,” [https://en.wikipedia.org/wiki/File:Greenland_\(orthographic_projection\).svg](https://en.wikipedia.org/wiki/File:Greenland_(orthographic_projection).svg).
- [Fig7] “Sketch of a rno-g station with in ice detector strings and surface antennas by 14lumiere,” https://commons.wikimedia.org/wiki/File:RNO-G_station_sketch.jpg#filelinks.
- [Fig8] J. Aguilar, P. Allison, J. Beatty et al., “Design and sensitivity of the radio neutrino observatory in greenland (RNO-g),” Journal of Instrumentation, vol. 16, no. 03, p. P03025, mar 2021. [Online]. Available: <https://doi.org/10.1088%2F1748-0221%2F16%2F03%2Fp03025>
- [Fig9] “Detector deployment,” <https://radio.uchicago.edu/detector.php>.

BIBLIOGRAPHY

- [1] S. Bilenky, “Neutrino. history of a unique particle,” The European Physical Journal H, vol. 38, no. 3, pp. 345–404, dec 2012. [Online]. Available: <https://doi.org/10.1140%2Fepjh%2Fe2012-20068-9>
- [2] J. Cowan, C. L., F. Reines, F. B. Harrison, H. W. Kruse, and A. D. McGuire, “Detection of the Free Neutrino: A Confirmation,” Science, vol. 124, no. 3212, pp. 103–104, Jul. 1956.
- [3] F. Mandl and G. Shaw, Quantum Field Theory, ser. A Wiley-Interscience publication. Wiley, 2010. [Online]. Available: <https://books.google.be/books?id=Ef4zDW1V2LkC>
- [4] B. Martin and G. Shaw, Particle Physics, ser. Manchester Physics Series. Wiley, 2017. [Online]. Available: <https://books.google.be/books?id=ielRDQAAQBAJ>
- [5] S. Dodelson, Modern Cosmology. Amsterdam: Academic Press, 2003.
- [6] B. T. Cleveland, T. Daily, J. Raymond Davis, J. R. Distel, K. Lande, C. K. Lee, P. S. Wildenhain, and J. Ullman, “Measurement of the solar electron neutrino flux with the homestake chlorine detector,” The Astrophysical Journal, vol. 496, no. 1, p. 505, mar 1998. [Online]. Available: <https://dx.doi.org/10.1086/305343>
- [7] S. M. Bilenky, “Bruno pontecorvo and neutrino oscillations,” Advances in High Energy Physics, vol. 2013, p. 873236, Sep 2013. [Online]. Available: <https://doi.org/10.1155/2013/873236>
- [8] G. Bellini, L. Ludhova, G. Ranucci, and F. L. Villante, “Neutrino oscillations,” Advances in High Energy Physics, vol. 2014, pp. 1–28, 2014. [Online]. Available: <https://doi.org/10.1155%2F2014%2F191960>
- [9] Z. Maki, M. Nakagawa, and S. Sakata, “Remarks on the Unified Model of Elementary Particles,” Progress of Theoretical Physics, vol. 28, no. 5, pp. 870–880, Nov. 1962.
- [10] K. Eguchi, S. Enomoto, K. Furuno, J. Goldman, H. Hanada, H. Ikeda, K. Ikeda, K. Inoue et al., “First results from kamland: Evidence for reactor antineutrino disappearance,” Physical Review Letters, vol. 90, no. 2, jan 2003. [Online]. Available: <https://doi.org/10.1103%2Fphysrevlett.90.021802>

- [11] A. Y. Smirnov, “The mikheyev-smirnov-wolfenstein (msw) effect,” 2019.
- [12] S. Chandrasekhar, “The Maximum Mass of Ideal White Dwarfs,” Astrophysical Journal, vol. 74, p. 81, Jul. 1931.
- [13] S. Weinberg and W. Steven, Gravitation and Cosmology: Principles and Applications of the General Theory of Relativity. Wiley, 1972. [Online]. Available: <https://books.google.be/books?id=XLbvAAAAMAAJ>
- [14] T. Melson, H.-T. Janka, R. Bollig, F. Hanke, A. Marek, and B. Müller, “Neutrino-driven explosion of a 20 solar-mass star in three dimensions enabled by strange-quark contributions to neutrino–nucleon scattering,” The Astrophysical Journal Letters, vol. 808, no. 2, p. L42, jul 2015. [Online]. Available: <https://dx.doi.org/10.1088/2041-8205/808/2/L42>
- [15] J. F. Beacom, “The diffuse supernova neutrino background,” Annual Review of Nuclear and Particle Science, vol. 60, no. 1, pp. 439–462, nov 2010. [Online]. Available: <https://doi.org/10.1146%2Fannurev.nucl.010909.083331>
- [16] T. K. Gaisser, R. Engel, and E. Resconi, Cosmic Rays and Particle Physics, 2nd ed. Cambridge University Press, 2016.
- [17] D. Griffiths, Introduction to Elementary Particles, ser. Physics textbook. Wiley, 2008. [Online]. Available: <https://books.google.be/books?id=Wb9DYrjcoKAC>
- [18] K. Greisen, “Cosmic ray showers,” Annual Review of Nuclear Science, vol. 10, no. 1, pp. 63–108, 1960. [Online]. Available: <https://doi.org/10.1146/annurev.ns.10.120160.000431>
- [19] G. A. Shields, “A brief history of active galactic nuclei,” Publications of the Astronomical Society of the Pacific, vol. 111, no. 760, pp. 661–678, jun 1999. [Online]. Available: <https://doi.org/10.1086%2F316378>
- [20] D. Kazanas, “Neutrinos from AGN,” in High Energy Gamma-Ray Astronomy: International Symposium, ser. American Institute of Physics Conference Series, F. A. Aharonian and H. J. Völk, Eds., vol. 558, Apr. 2001, pp. 370–380.
- [21] F. Bradascio, “Search for high-energy neutrinos from agn cores,” 2019. [Online]. Available: <https://arxiv.org/abs/1908.05170>
- [22] K. MØller, P. B. Denton, and I. Tamborra, “Cosmogenic neutrinos through the GRAND lens unveil the nature of cosmic accelerators,” Journal of Cosmology and Astroparticle Physics, vol. 2019, no. 05, pp. 047–047, may 2019. [Online]. Available: <https://doi.org/10.1088%2F1475-7516%2F2019%2F05%2F047>
- [23] G. T. Zatsepin and V. A. Kuz'min, “Upper Limit of the Spectrum of Cosmic Rays,” Soviet Journal of Experimental and Theoretical Physics Letters, vol. 4, p. 78, Aug. 1966.
- [24] K. Greisen, “End to the Cosmic-Ray Spectrum?” , vol. 16, no. 17, pp. 748–750, Apr. 1966.
- [25] S. Fukuda, Y. Fukuda, T. Hayakawa, E. Ichihara, M. Ishitsuka, Y. Itow, T. Kajita, J. Kameda, K. Kaneyuki, S. Kasuga, Kobayashi et al., “The Super-Kamiokande detector,” Nuclear Instruments and Methods in Physics Research A, vol. 501, no. 2, pp. 418–462, Apr. 2003.
- [26] J. Boger et al., “The Sudbury neutrino observatory,” Nucl. Instrum. Meth. A, vol. 449, pp. 172–207, 2000.

- [27] S. Buitink, J. Bacelar, R. Braun, G. de Bruyn, H. Falcke, O. Scholten, K. Singh, B. Stappers, R. Strom, and R. al Yahyaoui, “The numoon experiment: first results,” 2008.
- [28] C. Glaser, D. García-Fernández, A. Nelles, J. Alvarez-Muñiz, S. W. Barwick, D. Z. Besson, B. A. Clark, A. Connolly, C. Deaconu, K. D. de Vries, J. C. Hanson, B. Hokanson-Fasig, R. Lahmann, U. Latif, S. A. Kleinfelder, C. Persichilli, Y. Pan, C. Pfendner, I. Plaisier, D. Seckel, J. Torres, S. Toscano, N. van Eijndhoven, A. Viereg, C. Welling, T. Winchen, and S. A. Wissel, “NuRadioMC: simulating the radio emission of neutrinos from interaction to detector,” *European Physical Journal C*, vol. 80, no. 2, p. 77, Jan. 2020.
- [29] “Measurement of the multi-TeV neutrino interaction cross-section with IceCube using earth absorption,” *Nature*, vol. 551, no. 7682, pp. 596–600, nov 2017. [Online]. Available: <https://doi.org/10.1038%2Fnature24459>
- [30] G. A. Askaryan, “Excess negative charge of an electron-photon shower and the coherent radio emission from it,” *Zhur. Eksptl’. i Teoret. Fiz.*, vol. 41, 8 1961. [Online]. Available: <https://www.osti.gov/biblio/4833087>
- [31] A. Connolly and A. G. Viereg, “Radio detection of high energy neutrinos,” in *Neutrino Astronomy*. WORLD SCIENTIFIC, mar 2017, pp. 217–240. [Online]. Available: https://doi.org/10.1142%2F9789814759410_0015
- [32] J. Jackson, *Classical Electrodynamics*. Wiley, 1998. [Online]. Available: <https://books.google.be/books?id=FOBBEAAAQBAJ>
- [33] V. V. Bogorodsky, C. R. Bentley, and P. E. Gudmandsen, *Electromagnetic Wave Propagation in Ice*. Dordrecht: Springer Netherlands, 1985, pp. 32–47. [Online]. Available: https://doi.org/10.1007/978-94-009-5275-1_3
- [34] T. Huege and D. Besson, “Radio-wave detection of ultra-high-energy neutrinos and cosmic rays,” *Progress of Theoretical and Experimental Physics*, vol. 2017, no. 12, nov 2017. [Online]. Available: <https://doi.org/10.1093%2Fptep%2Fptx009>
- [35] M. Aartsen, M. Ackermann, J. Adams, J. Aguilar *et al.*, “The IceCube neutrino observatory: instrumentation and online systems,” *Journal of Instrumentation*, vol. 12, no. 03, pp. P03 012–P03 012, mar 2017. [Online]. Available: <https://doi.org/10.1088%2F1748-0221%2F12%2F03%2FP03012>
- [36] M. G. Aartsen, M. Ackermann, J. Adams, J. A. Aguilar *et al.*, “Neutrino astronomy with the next generation icecube neutrino observatory,” 2019.
- [37] H. Schoorlemmer, K. Belov, A. Romero-Wolf, D. García-Fernández, V. Bugaev *et al.*, “Energy and flux measurements of ultra-high energy cosmic rays observed during the first anita flight,” *Astroparticle Physics*, vol. 77, pp. 32–43, 2016. [Online]. Available: <https://www.sciencedirect.com/science/article/pii/S0927650516000025>
- [38] P. Allison, R. Bard, J. Beatty, D. Besson, C. Bora, C.-C. Chen, C.-H. Chen, P. Chen, A. Christenson, A. Connolly, J. Davies, M. Duvernois, B. Fox, R. Gaior, P. Gorham, K. Hanson, J. Haugen, B. Hill, K. Hoffman, E. Hong, S.-Y. Hsu, L. Hu, J.-J. Huang, M.-H. Huang, A. Ishihara, A. Karle, J. Kelley, D. Kennedy, I. Kravchenko, T. Kuwabara, H. Landsman, A. Laundrie, C.-J. Li, T. Liu, M.-Y. Lu, L. Macchiarulo, K. Mase, T. Meures, R. Meyhandan, C. Miki, R. Morse, J. Nam, R. Nichol, G. Nir, A. Novikov, A. O’Murchadha, C. Pfendner, K. Ratzlaff, M. Relich, M. Richman, L. Ritter, B. Rotter, P. Sandstrom, P. Schellin, A. Shultz, D. Seckel, Y.-S. Shiao, J. Stockham, M. Stockham, J. Touart, G. Varner, M.-Z. Wang, S.-H. Wang, Y. Yang, S. Yoshida, and R. Y. and,

- “Performance of two askaryan radio array stations and first results in the search for ultrahigh energy neutrinos,” Physical Review D, vol. 93, no. 8, apr 2016. [Online]. Available: <https://doi.org/10.1103%2Fphysrevd.93.082003>
- [39] S. Barwick, E. Berg, D. Besson, G. Binder, W. Binns, D. Boersma, R. Bose, D. Braun, J. Buckley, V. Bugaev, S. Buitink, K. Dookayka, P. Dowkontt, T. Duffin, S. Euler, L. Gerhardt, L. Gustafsson, A. Hallgren, J. Hanson, M. Israel, J. Kiryluk, S. Klein, S. Kleinfelder, H. Niederhausen, M. Olevitch, C. Persichelli, K. Ratzlaff, B. Rauch, C. Reed, M. Roumi, A. Samanta, G. Simburger, T. Stezelberger, J. Tatar, U. Uggerhoj, J. Walker, G. Yodh, and R. Young, “A first search for cosmogenic neutrinos with the ARIANNA hexagonal radio array,” Astroparticle Physics, vol. 70, pp. 12–26, oct 2015. [Online]. Available: <https://doi.org/10.1016%2Fj.astropartphys.2015.04.002>
- [40] I. Kravchenko, S. Hussain, D. Seckel, D. Besson, E. Fensholt, J. Ralston, J. Taylor, K. Ratzlaff, and R. Young, “Updated results from the RICE experiment and future prospects for ultra-high energy neutrino detection at the south pole,” Physical Review D, vol. 85, no. 6, mar 2012. [Online]. Available: <https://doi.org/10.1103%2Fphysrevd.85.062004>
- [41] P. Allison, S. Archambault, R. Bard, J. Beatty, M. Beheler-Amass, D. Besson, M. Beydler, M. Bogdan, C.-C. Chen, C.-H. Chen, P. Chen, B. Clark, A. Clough, A. Connolly, L. Cremonesi, J. Davies, C. Deaconu, M. DuVernois, E. Friedman, J. Hanson, K. Hanson, J. Haugen, K. Hoffman, B. Hokanson-Fasig, E. Hong, S.-Y. Hsu, L. Hu, J.-J. Huang, M.-H. Huang, K. Hughes, A. Ishihara, A. Karle, J. Kelley, R. Khandelwal, M. Kim, I. Kravchenko, J. Kruse, K. Kurusu, H. Landsman, U. Latif, A. Laundrie, C.-J. Li, T. Liu, M.-Y. Lu, A. Ludwig, K. Mase, T. Meures, J. Nam, R. Nichol, G. Nir, E. Oberla, A. ÓMurchadha, Y. Pan, C. Pfendner, M. Ransom, K. Ratzlaff, J. Roth, P. Sandstrom, D. Seckel, Y.-S. Shiao, A. Shultz, D. Smith, M. Song, M. Sullivan, J. Touart, A. Viereg, M.-Z. Wang, S.-H. Wang, K. Wei, S. Wissel, S. Yoshida, and R. Young, “Design and performance of an interferometric trigger array for radio detection of high-energy neutrinos,” Nuclear Instruments and Methods in Physics Research Section A: Accelerators, Spectrometers, Detectors and Associated Equipment, vol. 930, pp. 112–125, jun 2019. [Online]. Available: <https://doi.org/10.1016%2Fj.nima.2019.01.067>
- [42] C. Glaser, D. García-Fernández, A. Nelles, J. Alvarez-Muñiz, S. W. Barwick, D. Z. Besson, B. A. Clark, A. Connolly, C. Deaconu, K. D. de Vries, J. C. Hanson, B. Hokanson-Fasig, R. Lahmann, U. Latif, S. A. Kleinfelder, C. Persichilli, Y. Pan, C. Pfendner, I. Plaisier, D. Seckel, J. Torres, S. Toscano, N. van Eijndhoven, A. Viereg, C. Welling, T. Winchen, and S. A. Wissel, “NuRadioMC: simulating the radio emission of neutrinos from interaction to detector,” The European Physical Journal C, vol. 80, no. 2, jan 2020. [Online]. Available: <https://doi.org/10.1140%2Fepjc%2Fs10052-020-7612-8>
- [43] C. Glaser, A. Nelles, I. Plaisier, C. Welling, S. W. Barwick, D. García-Fernández, G. Gaswint, R. Lahmann, and C. Persichilli, “NuRadioReco: a reconstruction framework for radio neutrino detectors,” The European Physical Journal C, vol. 79, no. 6, jun 2019. [Online]. Available: <https://doi.org/10.1140%2Fepjc%2Fs10052-019-6971-5>
- [44] T. Winchen, “RadioPropa — a modular raytracer for in-matter radio propagation,” EPJ Web of Conferences, vol. 216, p. 03002, 2019. [Online]. Available: <https://doi.org/10.1051%2Fepjconf%2F201921603002>
- [45] K. Yee, “Numerical solution of initial boundary value problems involving maxwell’s equations in isotropic media,” IEEE Transactions on Antennas and Propagation, vol. 14, no. 3, pp. 302–307, 1966.

- [46] R. Herman, A Treatise on Geometrical Optics. Creative Media Partners, LLC, 2019. [Online]. Available: <https://books.google.be/books?id=rp5ByAEACAAJ>
- [47] M. M. Herron and C. C. Langway, “Firn densification: An empirical model,” Journal of Glaciology, vol. 25, no. 93, p. 373–385, 1980.
- [48] G. D. Q. Robin, S. Evans, and J. T. Bailey, “Interpretation of radio echo sounding in polar ice sheets,” Philosophical Transactions of the Royal Society of London. Series A, Mathematical and Physical Sciences, vol. 265, no. 1166, pp. 437–505, 1969. [Online]. Available: <http://www.jstor.org/stable/73767>
- [49] N. Heyer and C. Glaser, “First-principle calculation of birefringence effects for in-ice radio detection of neutrinos,” The European Physical Journal C, vol. 83, no. 2, p. 124, Feb 2023. [Online]. Available: <https://doi.org/10.1140/epjc/s10052-023-11238-y>
- [50] B. Oeyen, I. Plaisier, A. Nelles, C. Glaser, and T. Winchen, “Effects of firn ice models on radio neutrino simulations using a RadioPropa ray tracer,” in 37th International Cosmic Ray Conference. 12-23 July 2021. Berlin, Mar. 2022, p. 1027.
- [51] J. A. Nelder and R. Mead, “A Simplex Method for Function Minimization,” The Computer Journal, vol. 7, no. 4, pp. 308–313, 01 1965. [Online]. Available: <https://doi.org/10.1093/comjnl/7.4.308>
- [52] J. Aguilar, P. Allison, J. Beatty et al., “Design and sensitivity of the radio neutrino observatory in greenland (RNO-g),” Journal of Instrumentation, vol. 16, no. 03, p. P03025, mar 2021. [Online]. Available: <https://doi.org/10.1088%2F1748-0221%2F16%2F03%2Fp03025>
- [53] R. N. Bracewell, “The fourier transform and its applications,” 1966.
- [54] A. Kovacs, A. J. Gow, and R. M. Morey, “The in-situ dielectric constant of polar firn revisited,” Cold Regions Science and Technology, vol. 23, no. 3, pp. 245–256, 1995. [Online]. Available: <https://www.sciencedirect.com/science/article/pii/0165232X9400016Q>
- [55] I. Kravchenko, D. Besson, and J. Meyers, “In situ index-of-refraction measurements of the south polar firn with the rice detector,” Journal of Glaciology, vol. 50, no. 171, p. 522–532, 2004.